

**THÈSE**

Pour obtenir le grade de

**DOCTEUR DE LA COMMUNAUTE UNIVERSITE  
GRENOBLE ALPES**

Spécialité : **BIS – Biotechnologie, instrumentation, signal et imagerie pour la biologie, la médecine et l'environnement**

Arrêté ministériel : 25 mai 2016

Présentée par

**Anna MÎRA**

Thèse dirigée par **Yohan PAYAN**, Directeur de recherche CNRS, Université Grenoble Alpes, et codirigée par **Serge MULLER**, Directeur scientifique GE Healthcare

préparée au sein du **Laboratoire Techniques de L'Ingénierie Médicale et de la Complexité - Informatique, Mathématiques et Applications** en collaboration avec GE Healthcare.  
dans l'**École Doctorale Ingénierie pour la santé la Cognition et l'Environnement**.

**Modélisation biomécanique du sein pour l'évaluation de la compression et de la perception d'inconfort en mammographie.**

Thèse soutenue publiquement le « **date de soutenance** », devant le jury composé de :

**Madame, Hilde, BOSMANS**

Professeur, Université KU Leuven, Rapporteur

**Monsieur, Martyn, NASH**

Professeur, Université d'Auckland, Rapporteur

**Madame, Corinne, BALLEYGUIER**

Médecin Radiologue, Institut Gustave Roussy, Membre

**Madame, Ann-Katherine, CARTON**

Ingénieur de recherche senior, Ge Healthcare, Membre

**Monsieur, Christian, HERLIN**

Praticien Hospitalo-Universitaire, CHU Montpellier, Membre





# **Breast biomechanical modeling for the evaluation of the compression and the discomfort perception in mammography.**

MÎRA Anna

Supervised by:

Yohan PAYAN, CNRS & Univ. Grenoble Alpes  
Serge MULLER, GE Healthcare  
Ann-Katherine CARTON, GE Healthcare

Jury members:

Hilde BOSMANS , KU Leuven  
Martyn P. NASH, University of Auckland  
Corinne BALLEYGUIER, Inst. Gustave Roussy  
Christian HERLIN, CHU Montpellier

Defense July 2018



## ABSTRACT

**Contexte** La mammographie est une modalité d'imagerie médicale à faible dose permettant la détection du cancer mammaire à un stade précoce. Lors de l'examen, le sein est comprimé entre deux plaques afin d'uniformiser son épaisseur et d'étaler les tissus. Cette compression améliore la qualité clinique de l'examen mais elle est également source d'inconfort chez les patientes. Bien que la mammographie soit la méthode de dépistage la plus efficace du cancer du sein, l'inconfort ressenti peut dissuader les femmes de passer cet examen. Par conséquent, une technique alternative de compression du sein prenant en compte le confort de la patiente, en plus de l'amélioration de la qualité d'image, présente un grand intérêt.

**Méthodes** Dans ce travail, nous avons proposé un nouvel environnement de simulation permettant l'évaluation de différentes techniques de compression du sein. La qualité de la compression a été caractérisée en termes de confort de la patiente, de la qualité d'image et de la dose glandulaire moyenne délivrée. Afin d'évaluer la déformation du sein lors de la compression, un modèle biomécanique par éléments finis du sein a été développé. Ce dernier a été calibré et évalué en utilisant des volumes IRM d'une volontaire dans trois configurations différentes (sur le dos, le ventre et de côté). Par ailleurs, la qualité d'image a été évaluée en utilisant un environnement de simulation d'imagerie auparavant validé pour la simulation de l'acquisition d'images en mammographie.

**Résultats** La capacité de notre modèle biomécanique à reproduire les déformations réelles des tissus a été évaluée. Tout d'abord, la géométrie du sein dans les trois configurations a été estimée en utilisant des matériaux Néo-Hookeens pour la modélisation des tissus mous. Les propriétés mécaniques des différents constituants du sein ont été estimés afin que les géométries du sein dans les positions couché sur le ventre et couché soient plus proches possibles des mesures. La distance de Hausdorff entre les données estimées et les données mesurées est égale à  $2.17\text{ mm}$  en position couché sur le ventre et  $1.72\text{ mm}$  en position couché sur le dos. Le modèle a ensuite été évalué dans une troisième configuration sur le

## ABSTRACT

---

côté, avec une distance de Hausdorff étant alors égale à  $6,14\text{ mm}$ . Cependant, nous avons été montré que le modèle Néo-Hookeen ne peut pas décrire intégralement le comportement mécanique riche des tissus mous. Par conséquent, nous avons introduit d'autres modèles de matériaux basés sur la fonction d'énergie de Gent. Cette dernière hypothèse a permis de réduire l'erreur maximale dans la configuration couché sur le ventre et dos incliné d'environ  $10\text{ mm}$ .

Le couplage entre la simulation de la mécanique du sein et la simulation d'aquisition d'image nous ont permis d'effectuer deux études préliminaires. Dans la première étude, les différences entre les pelotes de compression standard rigide et flex ont été évaluées. Selon les simulations effectuées, l'utilisation de la pelote flex pour la compression du sein a le potentiel d'améliorer le confort de la patiente sans affecter la qualité de l'image ou la dose glandulaire moyenne.

Dans la seconde étude, l'impact du positionnement du sein sur la mécanique globale de la compression mammaire a été étudié. Nos simulations confirment que rapprocher la pelote de compression de la cage thoracique peut augmenter l'inconfort de la patiente. Selon les données estimées, pour une même épaisseur du sein sous compression, la force appliquée au sein peut être s'accroître de 150 %.

**Conclusion** L'estimation réaliste de la géométrie du sein pour différentes configurations sous l'effet de la gravité, ainsi que les résultats conformes aux descriptions cliniques sur la compression du sein, ont confirmé l'intérêt d'un environnement de simulation dans le cadre de nos études.

**Mots clés** Mammographie, compression mammaire, confort du patient, modèle biomécanique

# ABSTRACT

**Background** Mammography is a specific type of breast imaging that uses low-dose X-rays to detect breast cancer at early stage. During the exam, the women breast is compressed between two plates in order to even out the breast thickness and to spread out the soft tissues. This compression improves the exam quality but can also be a source of discomfort. Though mammography is the most effective breast cancer screening method, the discomfort perceived during the exam might deter women from getting the test. Therefore, an alternative breast compression technique considering the patient comfort in addition to an improved clinical image quality is of large interest.

**Methods** In this work, a simulation environment allowing the evaluation of different breast compression techniques was put forward. The compression quality was characterized in terms of patient comfort, image quality and average glandular dose. To estimate the breast deformation under compression, a subject-specific finite element biomechanical model was developed. The model was calibrated and evaluated using MR images in three different breast configurations (supine, prone and supine tilted). On the other hand, image quality was assessed by using an already validated simulation framework. This framework was largely used to mimic image acquisitions in mammography.

**Findings** The capability of our breast biomechanical model to reproduce the real breast deformations was evaluated. To this end, the geometry estimates of the three breast configurations were computed using Neo-Hookean material models. The subject specific mechanical properties of each breast's structures were assessed, to get the best estimates of the supine and prone configurations. The Hausdorff distances between the estimated and the measured geometries were equal to  $2.17\text{ mm}$  and  $1.72\text{ mm}$  respectively. Then, the model was evaluated using a supine tilted configuration; with a Hausdorff distance of  $6.14\text{ mm}$ . However, we have shown that the Neo-Hookean strain energy function cannot fully describe the rich mechanical behavior of breast soft tissues. Therefore, alternative material models based on the Gent strain energy function were proposed. The latter as-

## ABSTRACT

---

sumption reduced the maximal error in supine tilted breast configuration by about 10mm.

The coupling between the simulations of the breast mechanics and the X-ray simulations allowed us to run two preliminary studies. In the first study, the differences between standard rigid and flex compression paddles were assessed. According to the performed simulations, using the flex paddle for breast compression may improve the patient comfort without affecting the image quality and the delivered average glandular dose.

In the second study, the impact of breast positioning on the general compression mechanics was described. Our simulations confirm that positioning the paddle closer to the chest wall is suspected to increase the patient discomfort. Indeed, based on the estimated data, for the same breast thickness under compression, the force applied to the breast may increase by 150%.

**Conclusion** The good results we obtained for the estimation of breast deformation under gravity, as well as the conforming results on breast compression quality with the already published clinical statements, have shown the feasibility of such studies by the means of a simulation framework.

**Keywords** Mammography, breast compression, patient comfort, biomechanical model

# CONTENTS

Contents	v
List of Symbols	1
General Problem statement	1
Technical approach	3
Thesis overview	5
Ethics	7
1 Clinical background	9
1.1 Breast anatomy . . . . .	10
1.1.1 Breast embryogenesis . . . . .	10
1.1.2 Breast external appearance . . . . .	11
1.1.3 Internal structures . . . . .	12
1.1.4 Adult breast texture changes . . . . .	15
1.2 Breast Cancer . . . . .	16
1.2.1 Cancer classification . . . . .	17
1.2.2 Breast cancer screening . . . . .	18
1.3 Medical imaging . . . . .	18
1.3.1 X-ray mammography . . . . .	18
1.3.2 Ultrasounds . . . . .	20
1.3.3 Magnetic resonance imaging . . . . .	20
1.4 Conclusion . . . . .	21

## *CONTENTS*

---

<b>2 Biomechanical breast modeling</b>	<b>23</b>
<i>State of the art</i>	
2.1 Continuous mechanics . . . . .	24
2.1.1 Deformation and strain . . . . .	24
2.1.2 Stress measures . . . . .	28
2.1.3 Conservation equations . . . . .	30
2.1.4 Constitutive models . . . . .	32
2.2 Finite Element Discretization . . . . .	35
2.2.1 Eulerian and Lagrangian mesh description . . . . .	35
2.2.2 Lagrangian mesh . . . . .	36
2.3 Contact mechanics . . . . .	39
2.3.1 Contact interface equations . . . . .	40
2.3.2 Surface interaction models . . . . .	41
2.3.3 Contact formulation algorithm: pure penalty model . . . . .	42
2.4 Breast biomechanical model: an overview . . . . .	44
2.4.1 Breast reference configuration . . . . .	45
2.4.2 Constitutive models . . . . .	46
2.4.3 Boundary conditions . . . . .	50
2.4.4 Summary . . . . .	51
<b>3 A new biomechanical breast model evaluated on real data</b>	<b>55</b>
3.1 Geometry extraction . . . . .	56
3.1.1 Data acquisition . . . . .	56
3.1.2 Image segmentation . . . . .	57
3.1.3 Image registration . . . . .	58
3.1.4 Subject-specific 3D geometry . . . . .	60
3.2 Finite Elements Mesh . . . . .	61
3.3 Breast reference configuration . . . . .	62
3.4 Boundary conditions . . . . .	64
3.5 Material constitutive models . . . . .	66
3.5.1 Model simplification . . . . .	68
3.5.2 Estimation of the optimal constitutive parameters . . . . .	69
3.6 Model validation . . . . .	72
3.7 Discussions and conclusion . . . . .	74
<b>4 Breast Compression</b>	<b>77</b>
<i>State of the art</i>	
4.1 Mammography positioning . . . . .	78
4.2 Paddles designs . . . . .	79
4.3 Compression mechanics . . . . .	80
4.4 Compression quality metrics . . . . .	82
4.4.1 Image quality . . . . .	83
4.4.2 Average glandular dose . . . . .	84

---

4.4.3	Pain and discomfort . . . . .	85
4.5	Recent advances in breast compression . . . . .	86
<b>5</b>	<b>Breast compression &amp; comfort</b>	
	<i>A comparative study</i>	<b>89</b>
5.1	Breast compression modeling . . . . .	90
5.1.1	FE modeling of compression paddles . . . . .	90
5.1.2	Breast compression mechanics . . . . .	91
5.1.3	Gent strain energy function . . . . .	93
5.1.4	Updated material constitutive models . . . . .	94
5.1.5	Gent model and breast mechanics under gravity loading . . . . .	96
5.2	Simulation of digital images . . . . .	99
5.2.1	Physical characteristics . . . . .	99
5.2.2	Breast phantom objects . . . . .	99
5.3	Compression quality metrics . . . . .	101
5.3.1	Patient comfort . . . . .	101
5.3.2	Image quality . . . . .	101
5.3.3	Average glandular dose . . . . .	102
5.4	Results . . . . .	102
5.4.1	Compression quality for rigid and flex paddles . . . . .	103
5.4.2	Paddle positioning impact on compression mechanics . . . . .	107
5.5	Discussion and conclusion . . . . .	109
<b>6</b>	<b>Conclusion and Perspectives</b>	<b>111</b>
<b>Conclusion</b>		<b>111</b>
6.1	Biomechanical breast model . . . . .	112
6.2	Breast compression and patient comfort . . . . .	114
<b>Key contributions</b>		<b>117</b>
<b>Publications</b>		<b>119</b>
<b>Appendices</b>		<b>i</b>
<b>A</b>	<b>Distance measures</b>	<b>iii</b>
<b>B</b>	<b>Mesh Convergence</b>	<b>v</b>
<b>C</b>	<b>Boundary conditions</b> <i>contact models</i>	<b>vii</b>
<b>Bibliography</b>		<b>xii</b>



## GENERAL PROBLEM STATEMENT

Today, mammography is the primary imaging modality for breast cancer screening and plays an important role in cancer diagnosis. Subtle soft-tissue findings and microcalcifications that may represent early breast cancer are visualized by means of X-rays images. After investigation, the abnormal findings are taken in charge for further evaluation.

A standard mammography protocol always includes breast compression prior to image acquisition. Women breast is compressed between two plates until a nearly uniform breast thickness is obtained. The breast flattening improves diagnostic image quality and reduces the absorbed dose of ionizing photons. However, the discomfort and pain induced by this compression procedure might deter women from attending a mammography. Fleming et al. [47] showed in a 2500 women panel study that 15% of those who skipped the second appointment cited an unpleasant or painful first mammogram.

An important improvement concerning the patient comfort could be achieved with the emergence of Full-Field Digital Mammography (FFDM). Due to the improved detector capabilities, digital mammography became better in terms of image quality and radiation dose than Film-Screen Mammography. The use of the Automatic Exposure Control (AEC) allows to estimate the acquisition parameters providing the optimal image quality and average glandular dose for a given breast thickness and glandularity. Therefore, FFDM may reduce breast compression while respecting the clinical gold standards on image quality.

Subsequently, there is an opportunity to leverage the potential of the recent imaging technologies by developing alternative breast compression techniques. The new techniques have to consider the patient comfort in addition to an improved image quality and a reduced ionizing radiation dose. This may imply another paddle geometry or peculiar material properties as well as distinct compression paddle positioning.

The goal of this PhD thesis was to develop a simulation environment able to characterize the impact of the paddle design on the patient comfort and its repercussion on the mammography image quality and average glandular dose. Due to the complexity of in-vivo clinical studies, a realistic simulation framework is of a large interest. To this end, the following tasks were considered.

## GENERAL PROBLEM STATEMENT

---

- To develop a biomechanical breast model taking into consideration the subject-specific breast geometry and tissues' mechanical properties.
- To evaluate this biomechanical breast model.
- To model the breast deformations under compression.
- To integrate the corresponding deformable breast phantom into the image acquisition simulation framework.
- To compute compression quality measures able to characterize the differences between various breast compression techniques in terms of patient comfort, image quality and average glandular dose.

Using the developed tools, two studies could be performed.

- To assess the differences between standard rigid and flex paddles in terms of patient comfort, image quality and average glandular dose for two different breast volumes.
- To assess the breast positioning impact on compression mechanics and patient comfort, considering one breast volume and one paddle model.

## TECHNICAL APPROACH

To study the impact of the paddle design on the compression quality, a simulation framework was developed. The breast mechanics and patient comfort were addressed by the means of finite element modeling (ANSYS<sup>1</sup>). On the other hand, the image quality could be assessed by using an image simulation framework modeling the X-rays propagation through matter during acquisition of a mammography image (CatSim<sup>2</sup>).

First, to develop a subject-specific breast model, the MR images of two volunteers in three distinct positions (supine, prone and supine tilted) were acquired. The MRI volumes were processed (ITK<sup>3</sup>/ VTK<sup>4</sup>/ CamiTK<sup>5</sup>) and segmented (ITK-Snap<sup>6</sup>). Then, the processed images were used to extract the 3D surfaces of the breast, compatible with ANSYS Mechanical meshing software. The breast geometries were discretized using tetrahedral solid elements and were the subjects of hyper-elastic quasi-static simulations. An exhaustive optimization process was performed to determine the subject-specific tissues mechanical properties as well as the corresponding breast stress-free configuration. The model was developed and calibrated such as the best estimates of supine and prone breast configurations were obtained. The model accuracy was assessed in terms of Hausdorff distance between the measured and estimated breast surfaces in supine tilted configuration.

Once the model was created and evaluated, it was used to quantify the breast compression quality. To this end, different finite element models of the paddle were developed with peculiar assumption on their flexibility and degrees of freedom. For each simulation of breast compression, the patient comfort was associated with the internal tissues stress/strain distribution and the pressure range at the skin surface. The mean average dose was computed using the model proposed by Dance D. et al. [31] for the corresponding

---

<sup>1</sup><https://www.ansys.com/>

<sup>2</sup>Milioni de Carvalho P. 2014, PhD thesis

<sup>3</sup><https://itk.org/>

<sup>4</sup><https://www.vtk.org/>

<sup>5</sup><http://camitk.imag.fr/>

<sup>6</sup><http://www.itksnap.org>

## TECHNICAL APPROACH

---

breast thickness derived from finite element simulations. The compressed breast geometry was then imported into the image simulation software (CatSim) together with an embedded set of virtual microcalcifications. Synthetic projections were then generated and the signal to noise ratio as well as the signal-difference to noise ratio were computed to characterize the resulting image quality.

# THESIS OVERVIEW

This manuscript is divided into six major chapters. **Chapter 1**, describes the clinical background required for a good understanding of our work. Both internal and external structure of the breast are described. The role of regular screening for breast cancer is discussed with a list of involved medical imaging technologies.

Chapters 2 and 3 are focused on breast biomechanical modeling. **Chapter 2** provides a brief introduction to the continuous and contact mechanics and describes the finite element numerical method able to solve such problems. This chapter provides also a review on biomechanical modeling of the breast. Successes and failures of experiments reported in the literature to determine the tissues material properties and breast stress-free geometry are discussed. The most advanced biomechanical models are listed with their corresponding errors with reference to real breast deformations. **Chapter 3** describes the breast biomechanical model we have proposed and the multi-loading gravity simulations that were performed to evaluate the model. First, the patient data acquisition as well as the required image pre-processing operations are presented. The optimal mesh size for such simulations is determined. Then, the model sensitivity to different boundary conditions and constitutive parameters is studied. The best modeling techniques of the main anatomical structures, such as the suspensory ligaments and the pectoral fascia, are selected. The results of the optimization process allowing to estimate the subject specific mechanical properties of breast tissues and stress-free geometry are presented. Finally, the model fidelity to the real deformations as measured in MR images of the breast in three different configurations, is discussed.

Chapters 4 and 5 are focused in breast deformation under compression modeling, as well as on the assessment of the compression quality in mammography. **Chapter 4** describes the breast compression process and its associated mechanics as recorded during real mammography acquisitions. The role of tissues compression in mammography as well as the current gold standards for image quality and average glandular dose are discussed. The last proposed technologies dealing with patient comfort and pain reducing techniques are outlined with their impact on patient comfort. In **Chapter 5**, two studies on breast

## THESIS OVERVIEW

---

compression quality are described. First, the finite element models of standard compression paddles are provided with the corresponding assumptions on their dynamics. The computed compression force and breast thickness are compared to the corresponding parameters issued from real mammography exams underwent by the volunteers. The derived adjustments of tissues constitutive models are provided. The details for mammography images simulation and breast phantom creation are also discussed. Next, the metrics of image quality, average glandular dose and patient comfort are defined and used to compare the compression quality between different paddle models and different paddle positions.

Finally, **Chapter 6** summarizes the work reported on this manuscript and generalizes the corresponding results. Perspectives and directions for future work are also provided.

## ETHICS AND FUNDING

This research project is financially supported by ANRT, CIFRE n°2014/1357.

The two involved volunteers agreed to participate in a pilot study approved by an ethical committee, MammoBio MAP-VS pilot study.

## **ETHICS AND FUNDING**

---

# 1

## CLINICAL BACKGROUND

The aim of this chapter is to provide the required clinical background on breast cancer screening and diagnosis for a good understanding of the global aim and relevance of the present work.

First, the breast evolution from early to the adult ages is described, with a detailed characterization of internal and external adult breast structures. To explain the intra-individual variation of breast mechanical and structural properties, hormonal changes during the menstrual cycle, pregnancy or menopause are presented. Next the cancer edogenesis is described and the most common cancer types are characterized. Finally, different modalities for breast imaging are presented with their underlying technical principles as well as their relevance for breast cancer regular screening.

## 1.1 Breast anatomy

Internal and external breast structures will be repeatedly referenced in the following work, therefore their detailed description including mechanical properties and their localization is needed. Although the breast anatomy seems to be simple and easy to understand, a detailed analysis of breast embryogenesis is requested for a better localization of the supporting breast tissues. The breast support matrix is a structure of high interests when modeling breast mechanics.

### 1.1.1 Breast embryogenesis

The breast is a modified skin gland which starts to develop at the embryonic stage from the epidermis and dermis. During the sixth fetal month, from 12 to 20 solid cords of epithelial cells are growing down into the dermis (Figure 1.1.a-b). Later, these cords evolve into lactiferous ducts and alveoli (Figure 1.1.c-d). Thus, near birth, a simple network of branching ducts is already developed in the pectoral area [131].

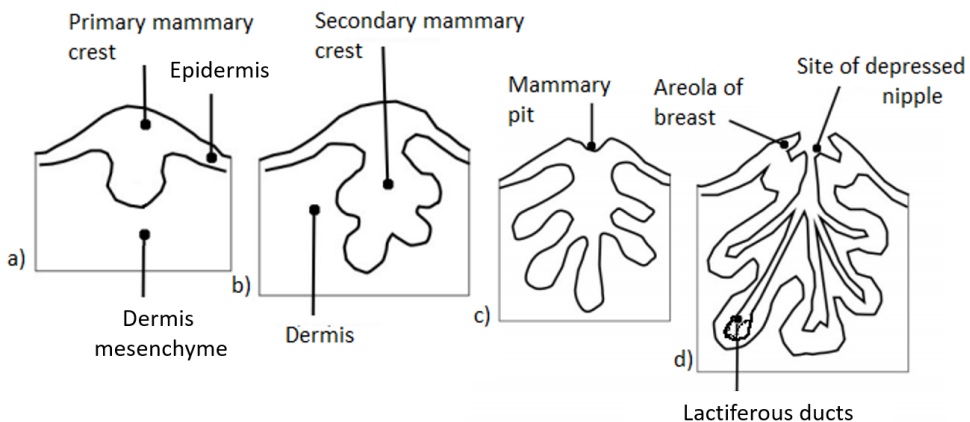


Figure 1.1: Breast embryogenesis: stages of formation of the duct system. The ectoderm is responsible for duct system and alveoli, the mesenchyme is responsible for the connective tissue and vessels [131].

The glandular lobes, generally remain underdeveloped until puberty (13 to 18 years). Under hormonal stimulation, the breast buds, due to the development of the mammary glands and increased deposition of fatty tissue, become palpable discs beneath the nipple. The ducts grow into the soft tissue and the lobular differentiation begins [84].

Kopans D.B. [84] analyzed the breast development sequence in the subcutaneous tissues. According to the author the evolution of the breast within the fascial system is unclear, with two possible evolution paths:

- (A) The superficial fascia splits in two layers forming the deep and the superficial fascia. The mammary glands appears between these two layers (Figure 1.2.A).

- (B) The elongating ducts retracts the superficial fascia. The mammary gland are enveloped by the superficial fascia (Figure 1.2.B)

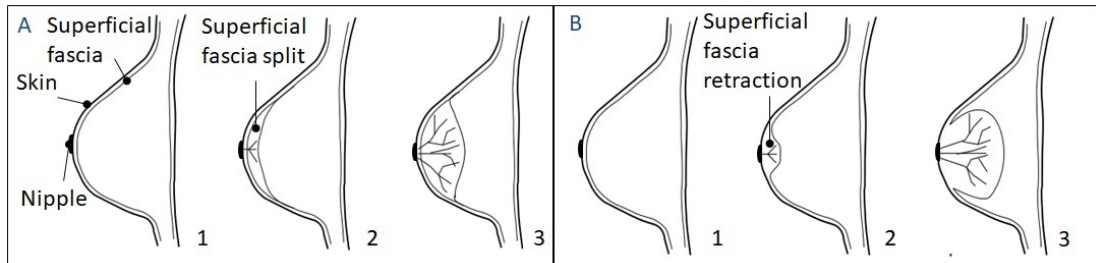


Figure 1.2: Breast development sequence in the subcutaneous tissues. A) Mammary bud development by splitting the superficial fascia in 2 layers. B) Mammary bud development by fascia retracting, reproduced from [84].

### 1.1.2 Breast external appearance

In order to describe the breast appearance, several notions for localization into the breast volume and its vicinity are defined. Usually, the breast volume is divided into four quadrants: upper outer quadrant (UOQ), upper inner quadrant (UIQ), lower outer quadrant (LOQ), lower inner quadrant (LIQ)(see Figure 1.3). On the other hand, the anatomical structures surrounding the breast are localized using the anatomical landmarks such as the inframammary fold, the clavicle, the sternal angle, the sternal line, the costal margin and the axilla.

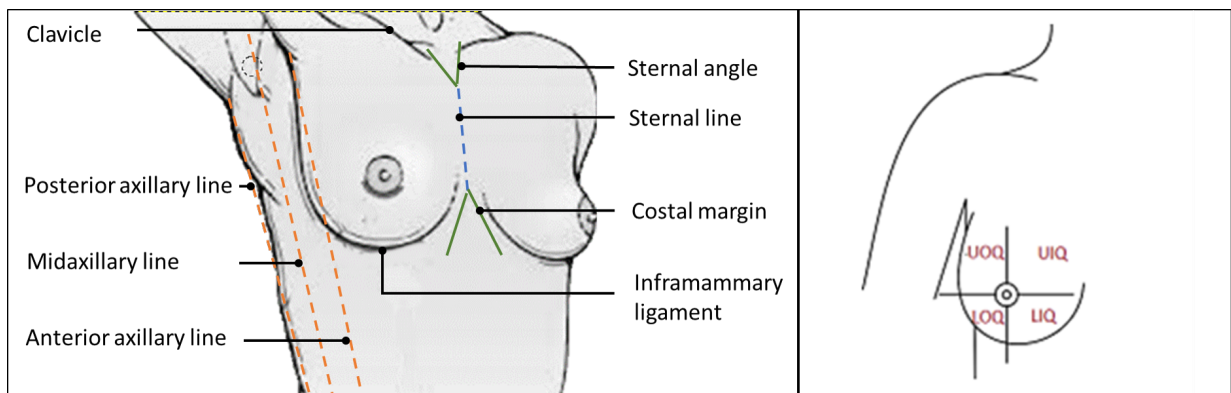


Figure 1.3: Left: thorax landmarks; Right: four breast quadrants [140]

Anatomically, the adult breast is localized on top of the ribcage, between the clavicle superiorly and costal margin inferiorly. Its transverse boundaries are defined from the sternal line medially to the midaxillary line laterally (Figure 1.3). The intra-individual asymmetry (between left and right breasts) is considered as a normality for the young and the adult breast. The breast shape and contour are influenced by [96]:

- The volume of mammary gland in each breast quadrants.
- The amount of the subcutaneous and intra-lobular fat.
- The body contour of the chest wall.
- The muscular covering and thickness.
- The thickness and elasticity of the skin.

Anthropomorphic characteristics of women breast were studied almost for the aim of cosmetic and reconstructive surgery. Vandeput J. and Nelissen M [140] measured distances between anatomical landmarks of the thorax of 973 women with aesthetically near-perfect breasts. The authors proposed different relations as guidelines to compute the recommended breast size parameters (nipple-mid clavicle distance, nipple inframammary fold distance) as a relation of body parameters (body height, torso width). In their study, a poor correlation was found between body height or weight and breast volume. Contrariwise a high correlation was found between the nipple to inframammary fold distance or the nipple to mid clavicle distance and the thorax width. Catanuto et al. [21] mentioned that the breast shape after surgery cannot be predicted by volumetric measurements only; they have proposed additional measures (areas, distances or angles) allowing unambiguous characterization of the breast shape. According to the authors, the curvature of the thoracic surface is the most relevant parameter to evaluate the outcome of a reconstructive breast surgery.

Starting with the Warner Brother Corset Company in 1935, the underwear industry introduced a new unit to measure the breast volume, the cup. The cup size is computed using a relation between the circumference of the chest at the level of the nipples and the torso width [109].

### 1.1.3 Internal structures

Breast heterogeneous structure includes a mixture of parenchyma and adipose tissue (Figure 1.4). The breast parenchyma consists of glandular components, lymphatic network and blood vessels [29]. Skin, Cooper's ligaments and fascias are the supporting system of the breast; their interconnection and intersections with the pectoral muscle fix and support the breast soft tissue [96].

The **adipose tissue** is the predominant tissue of the breast that fills up depressions between the deep and superficial fascia. In the intra-fascial space, adipose tissue surrounds and is dispersed among the glandular structures. Fat properties and its spatial distribution give the breast a soft consistency. The main aim of this tissue is to protect the lobes and lactiferous ducts.

The **glandular tissue** is represented by breast lobes. A healthy female breast is made up of 12-20 lobes. They are distributed centrally and laterally within the breast. The total amount of glandular tissue depends on the hormonal fluctuation, age and physical state.

Mammary ducts arise from the lobes as branches and connect them to the female nipple. There are about ten duct systems with a tree-like structure in each breast that carry the milk from the lobes to the nipple. The dark area of skin surrounding the nipple is called the areola.

Huang S. and team [74] have studied the breast shape and fibro-glandular distribution using dedicated breast CT images. This study shows that the glandular tissues is situated in the central portion of the breast. In prone position about 60 % of glandular tissues is located near to the nipple. A mean percentage of glandular tissue was computed by Yaffe M. and colleagues [147], the values varied from 13.7% to 25.6 % within different groups. They also mentioned a drop in glandular fraction with the advancing age.

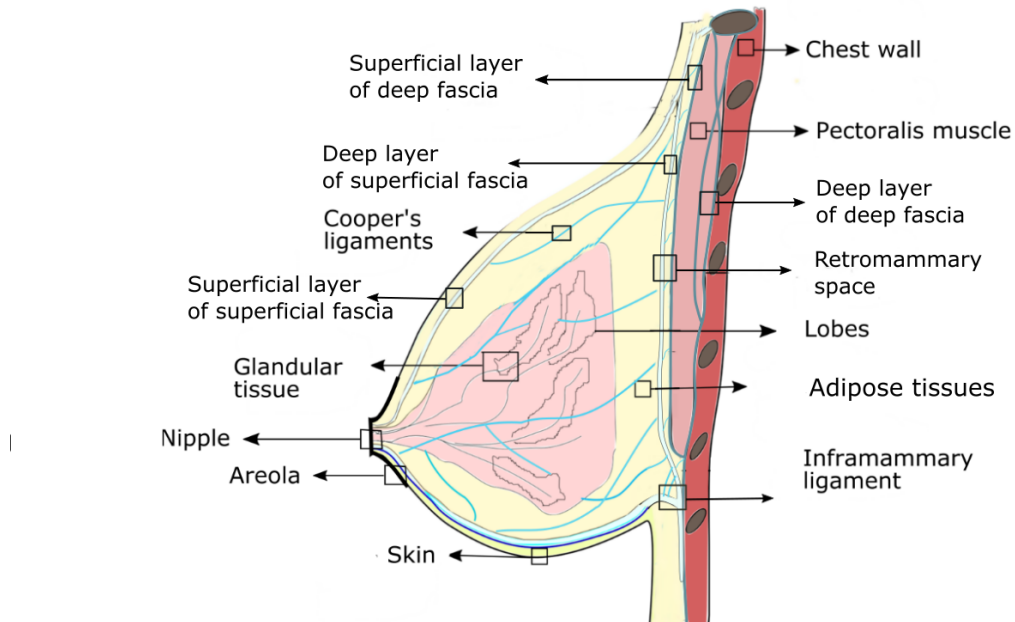


Figure 1.4: Breast anatomy [29].

A layer of adipose tissue and connective fascia separates the breast from the pectoral muscle forming a retro-mammary fat space.

The **skin** is the covering breast layer which provides protection and receives sensory stimuli from the external environment. It is a heterogeneous organ composed of three layers (see Figure 1.5 , [78]): epidermis (dead cells) mainly composed of keratin, dermis composed of collagen and elastin fibers in a viscous matrix made of water and glycoproteins and hypodermis, mainly composed of adipocytes cells.

The breast skin thickness varies from the breast base to the nipple between  $\sim 2\text{ mm}$  and  $\sim 0.5\text{ mm}$ . At the nipple areola region, the skin is 4-5 mm thick. [4]. Sutradhar A. and Miller M.J. [134] studied the breast skin thickness of 16 different sectors radially

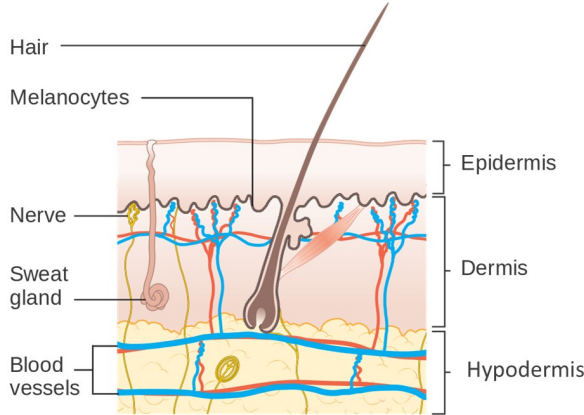


Figure 1.5: Skin anatomy, *Cancer Research UK*

oriented around the nipple. The thickness range proposed by the authors varies between  $0.83mm$  and  $2.35mm$  with a mean of  $1.55 \pm 0.25mm$ . According to this study, the skin thickness varies as follows: the lateral region thickness is the thinnest among all the breast regions followed by superior/inferior and medial region; there is no significant difference between the inferior and superior breast regions; in the radially exterior region, the skin is thicker than in the radially interior region (close to the nipple). During the breast puberty, the breast volume increases and the skin thickness decreases in all regions [138].

The **connective tissue** is represented by Cooper's ligaments and fascial system. The breast fascial system is composed of deep fascia and superficial fascia. During puberty, breast is growing and the superficial fascia divides in two layers: the deep layer of the superficial fascia and the superficial layer of the superficial fascia [84]. Cooper's ligaments run throughout the breast tissue parenchyma from the deep layer of the superficial fascia beneath the breast to the superficial layer of superficial fascia where they are fixed (Figure 1.4). Because they are not taut, these ligaments allow the natural motion of the breast [29]. Between the deep layer of the superficial fascia and the superficial layer of the deep fascia, a layer of connective loose tissue form the retro-mammary space, allowing the breast tissue to slide over the chest [96]. In regions where the superficial fascia meets the deep fascia, suspension ligaments are created. One of these ligaments is situated at the level of the sixth and seventh ribs and is called the **inframammary ligament** [12]. It evolves into the **deep lateral ligament** and the **deep cranial ligament** that are respectively attached to the axillary fascia and to the clavicle. The second meeting point of the two fascias is situated on the sternal line and is called the **deep medial ligament** (Figure 1.6). On the upper part of the breast, near the second rib space, the deep fascia tightly connects with the two layers of the superficial fascia, and create a the third meeting point. The three ligaments are 3D structures, evolving from the pectoral muscle toward the nipple, underlying the skin surface.

The existence, the topography, and the thickness of the membranous layers of the superficial fascia have been studied in various regions of the body [2]. According to the

authors, the thickness of these superficial layers in both superior and inferior breast regions is equal to  $88.12 \pm 7.70\mu m$  and  $140.27 \pm 11.03\mu m$  respectively.

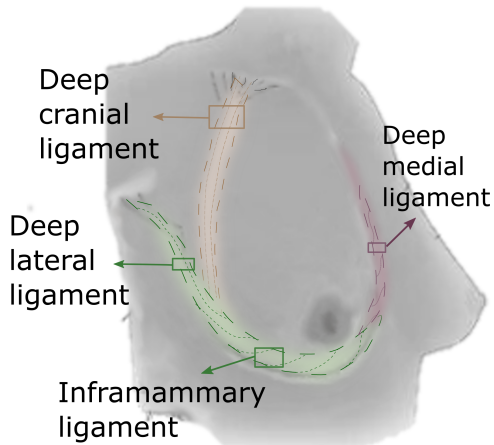


Figure 1.6: Suspensory ligaments. The suspensory ligaments together with the fascias constitute the breast support matrix and ensure the tissues inter-connection [96].

The lymphatic system is a vessel network which insures the transportation of white blood cells from tissues into the bloodstream. All intramammary lymph nodes are located in the lateral half of the breast along the margin of the breast parenchyma [84]. The lymphatic drainage of the breast extends from the subareolar plexus deep to and around the nipple (Figure 1.7 ).

The blood supply to the breast comes primarily from the internal mammary artery named successively subclavian, axillary, and brachial arteries (Figure 1.7). From them, the lateral and internal thoracic arteries run underneath the main breast tissue.

#### 1.1.4 Adult breast texture changes

The female breast undergoes substantial changes during the woman's lifetime. Most changes are caused by hormones and by woman's physiological condition. Important changes in female breast stiffness and composition occur during the menstrual cycle, pregnancy and menopause.

There are three important phases during the menstrual cycle caused by hormonal fluctuation [4]. During the first phase, the estrogen (hormones) diffusion stimulates the epithelial cell multiplication and the enlargement of ductal structures. Next, during ovulation, epithelial cells begin to grow in the lobule due to progesterone hormone; an increase in blood flow is also noticed. In the last phase, the ductal structures and the lobes support an involution and a regression process. It must be mentioned that not all lobules regress, therefore during menstrual cycle new lobules can be created. The work by Lorenzen J. et al. [89] showed that, during the premenstrual phase the stiffness of fibro-glandular tissue and glandular tissue can change by 30% and 14 % respectively. They also have shown that

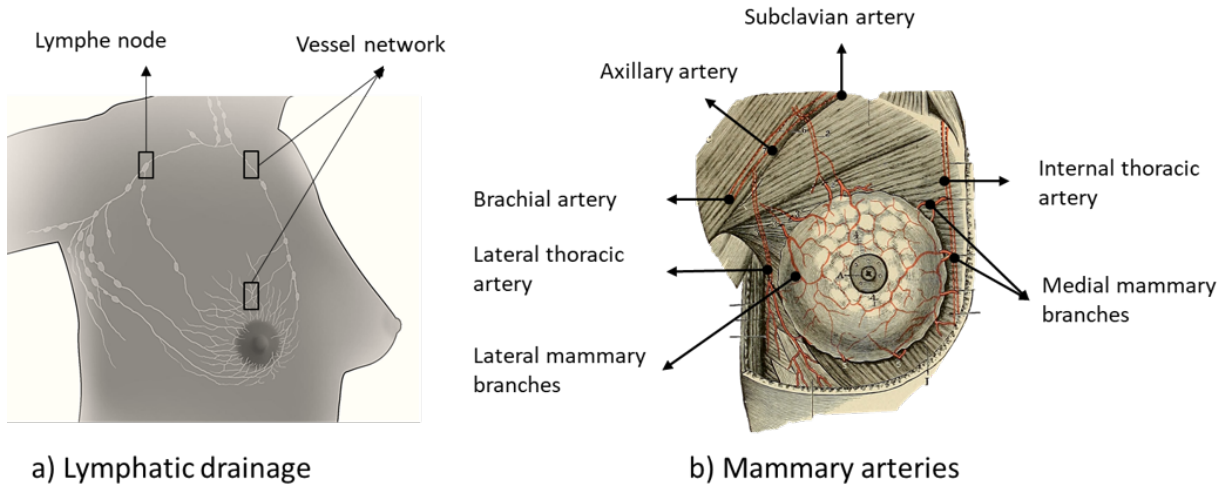


Figure 1.7: Lymphatic system and Mammary Arteries for adult female breast. Images reproduced from National Cancer Institute [97] and Pilcher L.S. et al. [115]

in the middle of the menstrual cycle, the parenchyma volume increases of 38% and the water content by 24.5%.

During pregnancy, under the influence of estrogen and progesterone, the breast enlarges in volume and density, the veins dilate and the proportion of parenchyma tissues increases. When lactation is weaned the breast returns to the pre-pregnancy state, and the atrophy of glandular, ductal, and stromal elements is observed [106].

The menopausal breast contains a larger fraction of fatty tissues and reduces the number of ductal and lobular elements. During the first four years after menopause, the breast is the subject of an atrophy process. The atrophy begins medially and posteriorly, then laterally, working its way to the nipple [4]. In this period the breast loses progressively fat and stoma tissue, resulting in breast shrinkage and loss of contours.

The breast support matrix can be stretched and attenuated by weight changes occurring during pregnancy and can relax with aging. These various changes can result in an excess of breast mobility over the chest and ptosis.

## 1.2 Breast Cancer

The first written description of breast cancer was on ancient Egyptian papyrus. At that time the treatment was considered futile and the woman was left without any medical assistance. Ancient Greeks, thought that the breast cancer was caused by an excess of black bile. It was thought that the monthly menstrual flow naturally relieved women of this excess, which explained why breast cancer was more common after menopause [4].

Nowadays, several researches [114, 90] have shown that the cancer is always caused by damages of a cell's DNA. The initiation of the mutagenic process that may result in various genetic errors requires cell division. A factor that increases cell proliferation will

increase also the risk of cancer. The woman hormones, estrogen and progesterone, appear to impact the breast cell division rate [28, 45], which explains the high rates of breast cancer in women (99% of breast cancer occurs in women). The risks of developing a cancer is increased by various factors like age, genetics, family history or life style. According to [90] the breast cancer risk factors can be explained by the exposure of women to the ovarian hormones during their lifetime.

The breast cancer is the second most frequent type of cancer and is the leading cause of death within women with cancer diagnosis [132]. The Foundation for Medical Research [49] estimates the risk of developing breast cancer for french women as 1 in 8 with more than 47% of cases diagnosed on women within 65 years old. According to the French Public Health Agency [132] the incidence of breast cancer has increased by 138% between 1980 and 2005. In United Kingdom and United States by year 2000 the death rate from breast cancer was reduced by almost 20% and in 2005 was down by 25% [113]. This significant improvement was attributable to the rise in the life expectancy and the upgrowth of screening technologies.

### 1.2.1 Cancer classification

The breast cancer type is determined by the specific cells that are affected. When a woman is developing a breast cancer in the epithelial cells, this type of tumor is called carcinoma. The primary tumor can also start in cells from other tissues such as muscle, fat or connective tissues. These types of tumors are called sarcomas, phyllodes, Paget disease and angiosarcomas but they are less frequent [3].

The carcinomas are then classified based on their location and how far the cancerous cell have spread. When the cancerous cells remain within the milk ducts or lobules, the cancer is classified as a non-invasive cancer. Otherwise, the malignant cancerous cells break through normal breast tissue barriers and spread out through other body organs, and they are classified as invasive cancer [4]. The most common types of carcinomas characterized by their location are: ductal carcinoma and lobular carcinoma.

The invasive ductal carcinoma starts in the epithelial cells that line the milk ducts, whereas the invasive lobular carcinoma starts in the lobules. Both evolve through the surrounding tissues and may widespread to the other organs through bloodstream and lymph nodes (metastasize).

Although the non-invasive carcinomas are not malignant, they have a 40% chance to change to invasive carcinomas over a 30-year period. The non-invasive ductal carcinomas start and stay inside the milk duct. The non-invasive lobular carcinomas overgrowth the normal breast cells and stay inside the lobule.

Invasive lobular carcinoma (ILC) may be harder to detect on physical exam as well as imaging, like mammograms, than invasive ductal carcinoma. Moreover, compared to other kinds of invasive carcinomas, about 1 in 5 women with ILC might have cancer in both breasts. Non-invasive ductal carcinoma is the more commonly detected form, making up 4% of symptomatic cancers and 20% of the cancer detected during a screening program. Its presence may be indicated on X-ray mammograms by microcalcifications ( $\mu calc$ ) [3].

### 1.2.2 Breast cancer screening

Early detection remains the primary defense available to prevent the development of breast cancer. Early detection of breast cancer is made possible by regular screening tests aimed to find suspicious lesions before any symptom can develop. The principal benefit of the regular screening is the potential to prevent the premature and often prolonged, painful death of the individual. Studies have shown that regular mammographic screening resulted in a 63% reduction in breast carcinoma death among women who actually underwent screening [135]. In 2012, the review of the UK screening program [98] showed that, it prevented 1300 deaths from breast cancer every year.

Secondary benefits include a reduction in the trauma by treating earlier-stage lesions. Indeed, earlier the invasive carcinoma detection, better the response to treatment, which means that the patient may avoid having a mastectomy or a chemotherapy.

Various worldwide countries have adopted organized breast cancer screening programs. Depending on the regional statistics and the estimated risk factors (age group, breast density, family history etc) the population is invited to participate to a free screening examination. In 1994, the French National Authority for Health approved a national screening program [48]. Since then, every woman within 50 and 74 years old, is invited one in two years for a clinical exam and a mammography.

The individuals who are suspected of having breast cancer, will have additional diagnostic tests as: diagnostic mammography, ultrasound (US), Magnetic Resonance Imaging (MRI), biopsy, blood test etc. The diagnostic test not only helps to confirm or to reject the screening suspicion, but also, in case of positive test, to determine the stage and the type of the breast cancer.

## 1.3 Medical imaging

Medical imaging is a technology domain used in medicine to capture information on human body internal structures or internal tissues properties. This information is then processed and analyzed in order to diagnose, monitor, or treat medical conditions. This technology encompasses different imaging modalities and processes, each with their own advantages and disadvantages. Next, the most relevant modalities for breast imaging are presented .

### 1.3.1 X-ray mammography

X-ray mammography is a type of medical imaging that uses X-rays to capture images of the internal structures of the breast (FDA definition). In digital mammography (also known as Full Field Digital Mammography, FFDM) X-rays are beamed through the breast to an image receptor (Figure 1.8). A detector converts X-rays to digital information.

The mammography is used to detect parenchymal distortions, asymmetries, masses and clusters of microcalcifications within the breast. These findings are not pathogenic and require a tissue diagnosis to confirm the presence of an invasive cancer, *in situ* can-

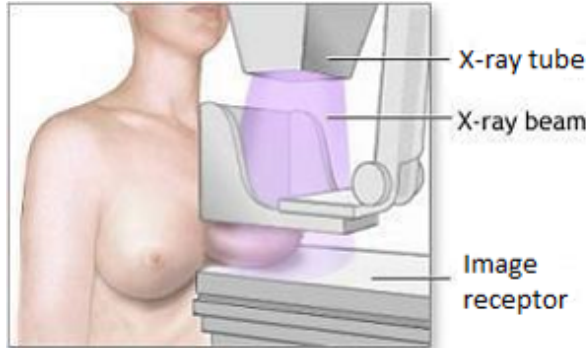


Figure 1.8: Mammography exam

cer, or a non-malignant lesion. Microcalcifications are small calcium deposits embedded in a protein matrix. They present X-ray attenuation coefficients substantially higher than breast tissue and therefore appear as bright spots in the X-ray images. The diameter of a microcalcification is typically inferior to 1 mm [70]. Breast microcalcifications present many shapes and sizes. They can be round, linear, coarse or granular. A mass is a radiological finding demonstrating an increased density versus the surrounding tissue. There is a large variation on mass size and shape. Usually a suspicious mass is larger than 8 mm and has irregular or speculated margins [92]. Asymmetries and parenchymal distortions are visualised as tethering or indentation of breast tissue. They are the third most common mammographic appearance of nonpalpable breast cancer, representing nearly 6% of abnormalities detected in screening mammography [54].

A standard mammographic protocol always includes breast compression prior to image acquisition. Women breast is compressed between two plates until a nearly uniform breast thickness is obtained. Nowadays, the European Commission recommends a standardized breast compression force, , i.e. the compression should stop at a level of force just below the subject's pain threshold or to the maximum setting of the machine (not to exceed 200 N). Analog mammography used screen/film detector technology in order to display breast internal structures, thus a uniform breast compression was needed in order to ensure a uniform exposure over the breast volume. With digital mammography, the exposure variation could be corrected with post-processing, while the breast compression is still indispensable to hold the breast away from the chest wall, to reduce the blur due to physical motion, to reduce the absorbed dose of ionizing photons, to separate overlapping structures or to reduce image degrading scatter [84].

Studies in different countries have assessed mammography sensitivity and specificity. The obtained sensitivity ranges between 81 and 88 %, and the specificity between 83 and 98 % [81, 72]. The mammography sensitivity is mostly affected in dense breasts. A dense breast is a breast for which the proportion of the fibroglandular tissues greatly exceed the proportion of fatty tissues. Fatty tissues are radiographically translucent, and lead to high intensity signal appearing on the mammographic images as dark areas. Meanwhile, the fibroglandular tissues and breast cancers tend to absorb more X-rays photons, therefore

they will appear as white areas. The lack of contrast between the cancer and dense regions of the background makes the detection more difficult.

### **1.3.2 Ultrasounds**

Breast ultrasound uses high-frequency sound waves to image breast tissues. The ultrasound technician put gel on the skin above the area of interest and moves the sound-emitting probe over the skin. The emitted waves are bounced by the breast tissue interfaces.. The probe picks up the reflected waves and transforms them into an image.

For asymptomatic women, a careful investigation of lateral and profound breast tissues is needed to identify the suspicious lesions. The limited field of view of the ultrasound image prevents from seeing abnormalities that lie deeper in the breast. Consequently, the ultrasounds are not sufficient for regular screening and are used to complement other screening tests. However, it is widely used to investigate suspicious lesions found within mammography, clinical or self-examinations. Breast ultrasound is particularly effective in differentiating cysts from solid lesions. It has a low sensitivity for detecting microcalcifications which is the most common feature in addition to masses associated with breast cancer. Breast ultrasound can also be used for differential diagnosis, local staging and intervention guidance.

**Ultrasound elastography** is a sonographic imaging technique combining the ultrasound technology with the basic physical principles of elastography. Elastography assesses tissue deformability by providing information on the tissue elasticity. It consists of either an image of strain in response to force or an image of estimated elastic moduli. This approach is somehow equivalent to clinical or self-examination, but with a higher precision.

Shear-wave elastography uses focused pulses of ultrasound generated by the probe to induce soft tissues deformation. The tissue elasticity is assessed either by directly measuring soft tissue deformation or by measuring the speed of shear wave propagation. The combination of SWE with conventional ultrasound increases the diagnostic performance for breast lesions, compared with conventional ultrasound alone [149]. Elastography serves as a complementary tool to differentiate benign from malignant lesions by providing information about the lesion stiffness [76, 103].

### **1.3.3 Magnetic resonance imaging**

Magnetic resonance imaging (MRI) is a noninvasive procedure used in breast imaging for studying internal structure of the breast that cannot be properly visualized using standard mammography (dense breasts). It employs radio-frequency waves and intense magnetic fields to excite hydrogen atoms. Body parts that contain hydrogen atoms (i.e. in water) are then imaged with contrasts depending on relaxation parameters characteristic of the tissues in the body. The quality of the image produced by MRI techniques depends, in part, on the strength of the received signal. For higher image quality, it is optimal to use an independent RF receiving coil placed in close proximity to the region of interest. For

breast imaging, dedicated breast MRI coils can be used. The patient is usually placed in prone position with the breast inside the coil and both arms by the sides of the body.

When the cancerous tumor develops, new vascularization is created on the direct surrounding to supply the tumor with oxygen and nutrient. Thus, for breast cancer imaging, a contrast agent may be used to enhance highly vascularized regions. These regions, most of the time associated to lesions, are visualized due to their uptake of contrast agent. Contrast enhanced MRI is used as a screening modality for women with high risk of breast cancer.

Low specificity and high cost of MRI restricts its use in a routine screening [112]. However, it is increasingly used for high-risk groups and for lesions that are difficult to detect with mammography or ultrasounds tests.

## 1.4 Conclusion

Today, mammography is the primary imaging modality used in breast cancer screening and plays an important role in cancer diagnosis. Ultrasounds and Magnetic Resonance Imaging are complementary imaging techniques mostly used in for dense breasts and high-risk women.

In order to obtain an accurate reading, the mammography machine needs to compress the breasts. The discomfort and pain produced by breast compression might deter women from attending breast screening by mammography [9, 47]. In a study by Dullum et al [37] more than 50% of attendants ( $N= 1800$ ) mentioned moderate to extreme physical discomfort. It has been reported that the fear for pain itself can already be by itself a reason to avoid getting the first mammogram [5], and that 15% of those who skipped the second appointment cited as the main cause an unpleasant or painful first mammogram [47, 144]. Postponing a mammographic exam can lead to delayed breast cancer diagnosis and worse prognosis (expected outcomes) for some women.

The main direct cause of pain in mammography is the flattening of the breast, which is directly linked to the applied compression force. Latest researches indicate that with a reduced level of compression (10N vs 30N), 24% of women did not experience a difference in breast thickness. If breast thickness is not reduced when compression force is further applied, then discomfort increases with no benefit in image quality or average glandular dose. Therefore, a detailed study on alternative breast compression techniques considering the patient comfort in addition to the image quality and ionizing radiation dose is needed.

The aim of this work is to provide a simulation framework capable to assess the patient physical comfort, as well as the corresponding image quality and average glandular dose for breast compression with different paddle designs. The developed numerical methods would serve to build an optimal compression paddle in terms of latter listed parameters, and therefore increase the adherence to breast cancer screening.

In this scope, a subject-specific biomechanical Finite Element (FE) model is developed and evaluated on real deformations measured on MR images. The proposed model is then used to compute the tissues deformation associated to breast compression during

---

*CHAPTER 1. CLINICAL BACKGROUND*

---

mammography. The resulting internal stress/strain intensities are then used as a first estimate of the patient comfort. The deformed breast geometry is the subject of an Monte-Carlo image simulation allowing to assess the image quality (IQ) and the average glandular dose (AGD), in order to validate the image quality for the different strategies of compression we are considering.

## BIOMECHANICAL BREAST MODELING

### *State of the art*

Finite elements models are widely used to estimate soft tissue deformations under pre-defined boundary conditions. Several biomechanical models of the breast were recently developed providing physics-based predictions of tissue motion and internal stress and strain intensity. A biomechanical model obtained from patient's MRI volumes can be subsequently used to mimic breast compression during mammography acquisitions.

This chapter provides theoretical background on continuous mechanic theory applied to soft tissue modeling. The principles of finite element theory are described including solid bodies and contact mechanics. A review of the existing biomechanical breast models is given, presenting the main challenges in the field and the proposed solutions. These developments provide the core foundation of our proposed patient specific breast model.

## 2.1 Continuous mechanics

Continuous mechanics is a branch of mechanics that deals with the analysis of the kinematics and the mechanical behavior of materials modeled as a continuous mass. Continuous mechanics is based on the following hypothesis: the matter is continuously distributed throughout the space occupied by the matter. Its formulation relies on how physical quantities, as for example pressure, temperature, and velocity, are measured macroscopically.

In this section the continuous mechanics theory applied to solid bodies is described using the books by Belytschko T. et al. [13] and Abeyaratne R. [1].

### 2.1.1 Deformation and strain

Continuous mechanics is the mathematical description of how physical objects respond to the application of forces.

A **body** is the mathematical abstraction of an **object** and is defined by its geometric and constitutive properties. At a macroscopic level, a solid object is described as a homogeneous and continuous body. Then, the substance of the object has a unique composition and completely fills the space it occupies, ignoring the granular (atomic) nature of matter. In continuous mechanics, a body  $\mathcal{B}$  is composed of **particles**  $p$  (or material points). Each particle is located at some defined **point**  $x$  in three dimensional space. All the points corresponding to the locations of all the particles, constitute the **domain**  $\Omega$  occupied by the body in a given configuration, also named *geometry*. A particular body can change its configuration and therefore the occupied region in the space when exposed to some external stimulus, such as force, pressure or heat.

The **configuration** of a body is defined as a one-to-one mapping between the particle  $p$  and position  $x$ ,  $\Omega_0 = \chi_0(\mathcal{B})$  (see figure 2.1). To describe the solid's response to external stimuli, one needs to know the changes in geometrical characteristics between at least two configurations: the configuration  $\Omega_1$  that one wishes to analyze, and the **reference configuration**  $\Omega_0$  relative to which the changes are to be measured. Here, (Figure 2.1), the mappings  $\chi_0$  and  $\chi_1$  take  $p \rightarrow X$  and  $p \rightarrow x$ , where  $X$  and  $x$  are the positions of particle  $p$  in the two configurations under consideration.

Frequently, the reference configuration is fixed for a given study and is arbitrarily chosen in a the most convenient way among all the configurations that the body can sustain.

The **deformation** of the body from the reference configuration  $\Omega_0$  is characterized by the next defined mapping  $\Phi$ :

$$x = \Phi(X) = \chi_1(\chi_0^{-1}(X)), \quad \text{where } X \in \Omega_0 \text{ and } x \in \Omega_1 \quad (2.1)$$

The **displacement**  $u$  of a particle is the difference between its position in the analyzed configuration (or current configuration) and its position in the reference configuration.

$$u(X) = \Phi(X) - X \quad (2.2)$$

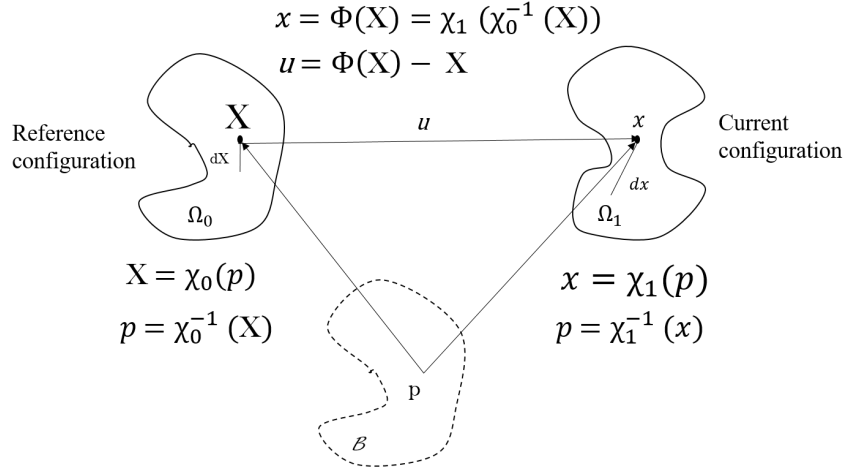


Figure 2.1: The position of a particle in the reference and current body configurations.

Suppose that  $G(\Omega_1)$  is the value of some extensive physical property associated with the body  $\mathcal{B}$  in the current configuration (such as the body mass  $m$ ). It exists a density  $g(x)$  such that:

$$G(\Omega_1) = \int_{\Omega_1} g(x) dv \quad (2.3)$$

where  $dv$  is the volume of the material element. Thus, the property  $G(\Omega_1)$  is related to the body while the density  $g(x)$  is related to the position of the body particle.

### Eulerian and Lagrangian formulations

There are two classical techniques used to describe the body physical characteristics depending on the choice of independent variables. Some physical characteristics, such as the mass density, can be defined for each individual particle. In such a case, the body characteristics are defined by:

$$\forall p \in \mathcal{B}, m = \mathcal{M}(p). \quad (2.4)$$

Here the coordinate system remains consistent and moves with the particle. Therefore, the coordinates of both the particle and the attached variable do not change along the deformation. A particle is an abstract entity and cannot be used in numerical calculations. Therefore, it is described by its location in the reference configuration  $p = \chi_0^{-1}(X)$ .

$$m = \mathcal{M}(p) = \mathcal{M}(\chi_0^{-1}(X)) \quad (2.5)$$

We call  $X$  Lagrangian or material coordinates, and its application is called Lagrangian or material description.

Instead of defining body characteristics as a function of body particles, one can define directly a body as a function of particle locations in current configuration by using the

relation  $x = \chi_1(p)$ , and therefore

$$m = \tilde{\mathcal{M}}(x) = \mathcal{M}(\chi_1^{-1}(x)) \quad (2.6)$$

Here the coordinate system is fixed and the particle coordinates are changing. Therefore, the position of particles, and any related quantity, change during the deformation. We call  $x$  Eulerian or spatial coordinates, and its application is called Eulerian or spatial description.

These approaches are distinguished by three important aspects: the mesh description, the stress tensor and momentum equilibrium, and the strain measure. The advantages and drawbacks of these two formulations will be discussed later in this chapter. Further, only Lagrangian formulation is used to describe the continuous deformation of soft tissue.

### Deformation gradient

In mathematical formulation the deformation gradient tensor  $F$  is the Jacobian matrix of the deformation  $\Phi(X)$ :

$$F = \frac{\partial \Phi(X)}{\partial X} = \frac{\partial x}{\partial X} \quad (2.7)$$

Considering infinitesimal quantities, the deformation gradient relates the segment  $dX$  in the reference configuration to the corresponding deformed segment  $dx$  in the current configuration (Figure 2.1)

$$dx = F \cdot dX. \quad (2.8)$$

In addition to the mapping of such vectors, the deformation gradient tensor allows also the mapping of differential volumes as:

$$dv = \det(F)dV = JdV \quad (2.9)$$

The Jacobian determinant  $J$  of the deformation gradient tensor  $F$  is a measure of the volume variation during the deformation. It can be used to relate extensive physical properties in the current and reference configurations:

$$\int_{\Omega_1} g(x)dv = \int_{\Omega_0} g(\Phi(X))JdV \quad (2.10)$$

### Local decomposition of the deformation gradient tensor into rotation and stretch

The deformation gradient tensor  $F$  completely characterizes the body deformation in the vicinity of a particle  $p$ . This deformation consists, locally, of a rigid body rotation and a body *stretch* (see Figure 2.2). As  $dX$  and  $dx$  are differential segments, the map  $F$  is not affected by rigid-body translations.

Generally, the body stretch is defined as the ratio of the deformed line elements to the length of the corresponding undeformed line element

$$l = \frac{|dx|}{|dX|}, \quad (2.11)$$

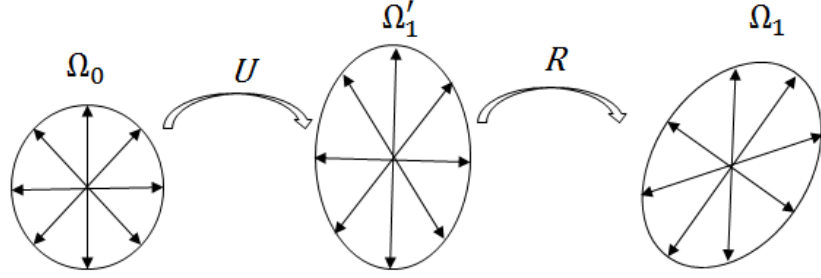


Figure 2.2: Local decomposition of the deformation tensor into stretch and rotation.

and consists locally on three mutually orthogonal stretches named **the principal stretches**.

According to the polar decomposition theorem, the deformation tensor can be written as the product of a proper orthogonal tensor  $R$  representing the rotational part, and a symmetric positive defined tensor  $U$  representing the body distortions

$$F = R \cdot U. \quad (2.12)$$

Where  $U$  and  $R$  are given by the relations  $U = (F^T \cdot F)^{\frac{1}{2}}$  and  $R = F \cdot U^{-1}$ . The essential property of tensor  $U$  is that it is symmetric and positive, therefore it has three real positive eigenvalues  $\lambda_1, \lambda_2, \lambda_3$  and a corresponding triplet of orthonormal eigenvectors  $r_1, r_2, r_3$ . Thus, when an infinitesimal segment  $dx$  is stretched by the tensor  $U$ , the segment is distorted in the principal directions of  $U$  by amounts of corresponding eigenvalues of  $U$ . The tensor  $U$  is also called the **right stretch tensor**. Since there is a one-to-one relation between  $U$  and  $U^2$ , for the simplification of numerical calculus, the stretch tensor can be replaced by the **Green deformation tensor**  $C = F^T \cdot F$ .

There are three particular functions of  $C$  called the principal invariants.

$$I_1(C) = \text{tr}C, \quad I_2(C) = \frac{1}{2} [\text{tr}C^2 - (\text{tr}C)^2], \quad I_3(C) = \det(C). \quad (2.13)$$

These functions are related to the three principal stretches by the following relations:

$$I_1(C) = \lambda_1^2 + \lambda_2^2 + \lambda_3^2, \quad I_2(C) = \lambda_1^2\lambda_2^2 + \lambda_2^2\lambda_3^2 + \lambda_3^2\lambda_1^2, \quad I_3(C) = \lambda_1^2\lambda_2^2\lambda_3^2 \quad (2.14)$$

The essential property of the principal invariants is that they do not change under coordinate transformations for a given body configuration. Their use to compute the body stretch is an essential part of constitutive modeling, because the behavior of a material should not depend on the coordinate system.

It also can be shown that:

$$\det(C - \mu I) = -\mu^3 + I_1(C)\mu^2 - I_2(C)\mu + I_3(C) \quad (2.15)$$

### Strain measures

Referring to small deformations, the engineering nominal strain is defined as the ratio of the change in length of the deformed line element to the length of the corresponding undeformed line element:

$$\epsilon = \frac{dx - dX}{dX} \quad (2.16)$$

When the body is not deformed, the deformation gradient  $F$  and therefore the right stretch tensor  $U$  is equal to identity tensor  $I$ . The strain in such a case is equal to zero.

For most biological soft tissues, large deformation has to be considered. In that case, the previously defined strain is no more applicable. For large deformations, a measure of strain can be any monotonically increasing function related to stretch in a one-to-one manner, this function has to vanish in the reference configuration [93]. In an orthogonal coordinate system, considering that  $m$  in an integer, an admissible function is

$$f(x) = \frac{1}{m}(x^m - 1) \text{ for } (m \neq 0) \text{ and } \ln(x) \text{ for } (m = 0). \quad (2.17)$$

For  $m = 0$ , this function represents the Hencky strain tensor,

$$E = \ln(U), \quad (2.18)$$

for  $m = 1$ , this function represents the Biot strain tensor

$$E = U - I, \quad (2.19)$$

and for  $m = 2$ , this function represents the Green-Lagrangian strain tensor:

$$E = \frac{1}{2}(U^2 - I) = \frac{1}{2}(C - I) \quad (2.20)$$

The Green-Lagrangian tensor is commonly used in practice as, by using the relation 2.15, it can be computed without prior knowledge of the eigenvectors of the Green deformation tensor  $C$ .

### 2.1.2 Stress measures

Generally, forces are categorized as internal and external forces. An **external force** is a force caused by an external agent outside of the system. Contrariwise an **internal force** is a force exchanged by the particle in the system. The external forces are categorized in **body forces** (acting at the distance) and **contact forces** (acting on the body surface). The relation between body forces per unit undeformed volume  $\tilde{b}(X)$  (Lagrangian coordinates) and body forces per unit deformed volume  $b(x)$  is given by the following relation:

$$\tilde{b} = \frac{dv}{dV} b = Jb. \quad (2.21)$$

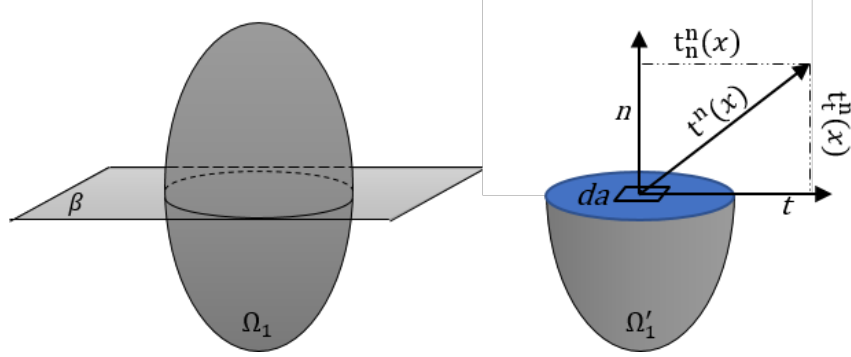


Figure 2.3: True stress vector  $t^n(x)$  at point  $x$  on the fictitious surface created by the cutting plane  $\beta$  of normal  $\vec{n}$  passing through the point  $x$ .

The contact forces can act on the external surface of the body or on an imaginary internal surface enclosing a volume element (Figure 2.3). In general terms, the stress (or the **traction vector**)  $t^n(x)$  is defined as contact force per unit area  $da$  in the limit as  $da \rightarrow 0$ . Therefore  $t^n(x)$  varies from point to point in intensity and orientation depending on the  $da(n)$  orientation. The stress vector projection on normal axis  $n$  defines the **normal stress vector** and its projection on the tangential axis defines the **shear stress vector**.

The stress on the boundary  $\partial\Omega_1$  of the region occupied by the body is applied by external forces through physical contacts along the boundary. When formulating and solving a boundary-value problem, this stress defines the boundary conditions.

### Cauchy's lemma

Cauchy's lemma states that traction vectors acting on opposite sides of a surface are equal and opposite.

$$t^{-n}(x) = -t^n(x) \quad (2.22)$$

### Cauchy's Law

Cauchy's law states that it exists a Cauchy stress tensor  $\sigma$  which maps linearly the normal to a surface to the stress vector acting on that surface, according to the next relation

$$t^n = \sigma \cdot n \quad \text{where} \quad t_i^n = \sigma_{i,j} n_j \quad (2.23)$$

When large deformations are considered, the reference and current configurations of the body are significantly different and a clear distinction has to be made between them. The traction vector  $t^n$  is defined in Eulerian coordinates (body current configuration) and is also called the **true stress**. Accordingly, the Cauchy stress tensor  $\sigma$  is called the true stress tensor.

The definition of any measure with respect to the deformed configuration is less practical as it is usually unknown a priori. For the simplification of mathematical formulation, a

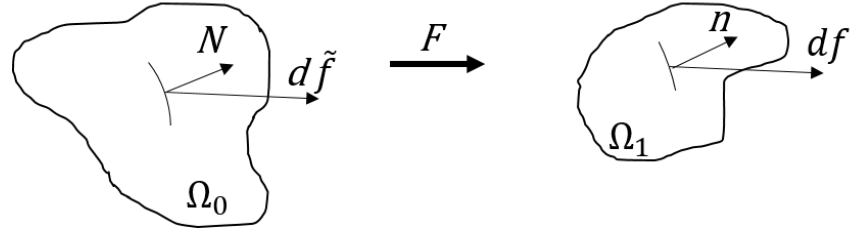


Figure 2.4: Deformation of area  $dA$  into area  $da$ . The force  $df$  acting on deformed area  $da$  and the pseudoforce  $d\tilde{f}$  acting on undeformed area  $dA$

new pseudostress is defined in the Lagrangian coordinate space named the **engineering stress**. The engineering stress has no physical meaning and has to be converted into true stress for any interpretation.

Below, two pseudostress vectors are defined (Fig. 2.4):

- $T^N$  defined as the contact force  $df$  per unit area  $dA$  in reference configuration.
- $\tilde{T}^N$  defined as the contact pseudoforce  $d\tilde{f}$  per unit area  $dA$  in reference configuration.

Accordingly, two pseudostress tensors are defined based on pseudostress vectors:

- $T^N = P \cdot N$ ,  $P$  is called **first Piola-Kirchhoff stress tensor**,
- $\tilde{T}^N = S \cdot N$ ,  $S$  is called **second Piola-Kirchhoff stress tensor**.

where  $N$  is the normal vector of unit area  $dA$  in the reference configuration.

The three stress tensors are linked by the next relation

$$\sigma = J^{-1} F \cdot P = J^{-1} F \cdot S \cdot F^T \quad (2.24)$$

### 2.1.3 Conservation equations

Three conservation laws must be satisfied by physical system subject to any applied boundary conditions: **conservation of mass**, **conservation of linear momentum** and **conservation of angular momentum**. The resulting equations describe partially the mechanical behavior of a continuous body.

#### Conservation of mass

The mass  $m$  of a body with the density  $\rho$ , that infills the space region  $\Omega_1$  is given by :

$$m(\Omega) = \int_{\Omega} \rho(X) dV \quad (2.25)$$

The mass conservation law requires that the body mass remains constant throughout all possible body configurations. In a Lagrangian formulation, this results in a relation between

the body density in the reference configuration  $\rho_1$  and the body density in the current configuration  $\rho$ .

$$\int_{\Omega_1} \rho_1 dv = \int_{\Omega_0} \rho_0 dV = const. \quad (2.26)$$

Using the relation 2.9 one can deduce that:

$$\int_{\Omega_0} (\rho_1 J - \rho_0) dV = 0 \quad and \quad \rho_1 J = \rho_0 \quad (2.27)$$

### **Conservation of the linear momentum**

Assuming that the body  $\mathcal{B}$  is defined on a arbitrary region  $\Omega_0$  with a boundary  $\Gamma_0$ , and is subject to a body-force  $\rho_0 b$  and the surface traction  $T^N$ . And let  $X$  be the particle location in the undeformed solid. The total force acting on the body  $\mathcal{B}$  is then defined as:

$$f = \int_{\Omega_1} \rho_0 b(X) dV + \int_{\Gamma_0} T^N(X) dA \quad (2.28)$$

The conservation of the linear momentum requires that the total force acting on the body to be equal to the time rate change of the linear momentum. In a static problem, the time rate change of the linear momentum is neglected and thus an equilibrium equation is obtained.

$$\rho_0 b + \nabla_0 \cdot P = 0 \quad (2.29)$$

Where the  $P$  is the first Piola-Kirchhoff stress tensor. The equilibrium equation can be formulated in terms of the second Piola-Kirchhoff stress tensor by using relations 2.24 .

### **Conservation of angular momentum**

The conservation of the angular momentum requires that the resultant momentum on any part of the body about a fixed point  $\mathcal{O}$  equals the rate of increasing of its angular momentum (about  $\mathcal{O}$ ). For a static problem, the integral form of the conservation of the angular momentum is defined as:

$$\int_{\Omega_0} X \times \rho_0 b(X) dV + \int_{\partial\Omega_0} X \times T^N(X) dA = 0 \quad (2.30)$$

The relation 2.30 requires that the second Piola-Kirchhoff stress tensor is a symmetric tensor:

$$S = S^T \quad (2.31)$$

In summary, the conservation equations are fulfilled if and only if the following local conditions are fulfilled at each point in the body:

$$\rho_1 J = \rho_0, \quad \nabla_0 \cdot S \cdot F^T + \rho_0 b = 0, \quad S = S^T \quad (2.32)$$

with the traction on the surface related to the stress through  $\tilde{T}^n = S \cdot N$ . For the simplification of mathematical calculus, the constitutive equations are formulated in terms of the second Piola-Kirchhoff stress tensor using the relations 2.24.

### 2.1.4 Constitutive models

The constitutive models, called also material models, define the relation between stress and strain of a physical system under the action of external stimuli. It is almost impossible to define a universal material behavior capable to model the material response to all possible conditions. Thus, for a given material, several constitutive models can be defined depending on the studied characteristics.

Biological materials are classified into:

- *Isotropic or anisotropic materials*: in a isotropic (anisotropic) material the values of a property are constant (vary) with respect to the direction.
- *Compressible or incompressible materials*: in a compressible (incompressible) material the volume changes (remains constant) during the deformation and the density remains constant. For an incompressible material the Jacobian determinant of the deformation tensor  $J$  is equal to 1.
- *Homogeneous or heterogeneous materials*: in a homogeneous (heterogeneous) material the values of a property are constant (vary) with respect to the position within the body.

Biological soft tissues are modeled using elastic materials model. The elasticity is the property of a solid material to return to its original size and shape when the influence of an external force is removed. In this case the strains are said to be reversible.

Considering small deformations, the stress-strain law of a linear material is given by the **Hook's law**

$$\sigma = \lambda \epsilon \quad (2.33)$$

,where the coefficient of proportionality  $\lambda$  is named **Young's modulus**.

Elastic materials may be defined also with a non-linear stress-strain relationship. In such cases the elastic modulus ( $\lambda$ ) is defined in function of strain  $\epsilon$

$$\lambda = \frac{\partial \sigma}{\partial \epsilon} = f(\epsilon). \quad (2.34)$$

For example, for an elastic exponential material [11] the elastic modulus is computed using the function

$$f(\epsilon) = b e^{m\epsilon}, \quad (2.35)$$

where  $b$  and  $m$  are material parameters.

For large deformations the stress-strain relationship is deduced from a potential function. A **hyperelastic** material is an elastic material for which the work is independent of the deformation path. The material reversibility and path-independent behavior implies the absence of energy dissipation during the deformation. Thus, there exists a **potential** function  $W(E)$  such that

$$S = \frac{\partial W(E)}{\partial E} = 2 \frac{\partial \psi(C)}{\partial C}.$$

Moreover, if the material is isotropic, the stored strain energy  $W$  of a hyperelastic material can be written as a function of principal invariants ( $I_1, I_2, I_3$ ) of the Green deformation tensor  $C$  previously defined in equation 2.13.

We introduce below the most used potential functions for the characterization of biological soft tissues.

For the simplification of potential expressions, we define the first and the second deviatoric strain (strain related to the deformation at constant volume) invariants:

$$\bar{I}_1 = \frac{I_1}{I_3^{2/3}}; \quad \bar{I}_2 = \frac{I_2}{I_3^{4/3}}$$

We also define the **Bulk modulus**  $K$  as measure of a material's resistance to compression, the **shear modulus**  $\mu$  as the ratio of shear stress to the shear strain, and the **Poisson ratio** as the ratio between longitudinal strain to the transverse strain describing the body shape change. For small deformations the Bulk modulus and the shear modulus are linked to the Young's modulus and the Poisson ratio by the following relations:

$$K = \frac{\lambda}{3(1 - 2\nu)} \quad \text{and} \quad \mu = \frac{\lambda}{2(1 + \nu)} \quad (2.36)$$

### **Neo-Hookean potential function**

The Neo-Hookean [137] law is an extension of the Hook's law to large deformations. The potential function is based only on the first invariant and is given by

$$W = \frac{\mu}{2}(\bar{I}_1 - 3) + \frac{K}{2}(J - 1)^2, \quad (2.37)$$

where  $\mu$  and  $K$  are the initial shear modulus and the initial Bulk modulus respectively.

### **Mooney-Rivlin potential function**

The potential function of a Mooney-Rivlin [122] material can be defined as:

$$W = \frac{\mu_1}{2}(\bar{I}_1 - 3) + \frac{\mu_2}{2}(\bar{I}_2 - 3) + \frac{K}{2}(J - 2)^2, \quad (2.38)$$

where the constants  $\mu_1$  and  $\mu_2$  describing the material properties are linked to the initial shear modulus  $\mu = (\mu_1 + \mu_2)$ , and the constant  $K$  is the initial Bulk modulus.

### **Gent potential function**

The potential function of a Gent [59] material model is defined as:

$$W = -\frac{\mu J_m}{2} \ln \left( 1 - \frac{\bar{I}_1 - 3}{J_m} \right) + \frac{K}{2} \left( \frac{J^2 - 1}{2} - \ln J \right), \quad (2.39)$$

where the constants  $\mu$  and  $K$  constants are the initial shear modulus and the initial Bulk modulus respectively. And  $J_m$  is a parameter limiting the value of  $(\bar{I}_1 - 3)$ .

### Ogden model

The Ogden [101] material model is based on the three principal stretches ( $\lambda_1, \lambda_2, \lambda_3$ ) and  $2N$  material constants, where  $N$  is the number of polynomials that constitute the potential function:

$$W = \sum_{i=1}^N \frac{\mu_i}{\alpha_i} (\lambda_1^{\alpha_i} + \lambda_2^{\alpha_i} + \lambda_3^{\alpha_i} - 3) + \sum_{k=1}^N \frac{K}{2} (J - 1)^{2k}, \quad (2.40)$$

where  $\mu_i$  and  $\alpha_i$  are material constants, and  $K$  is the Bulk modulus.

### Yeoh model

The potential function of Yeoh [148] model is based on the first invariant:

$$W = \sum_{i=1}^N \mu_i (\bar{I}_1 - 3)^i + \sum_{k=1}^N \frac{K}{2} (J - 1)^{2k}, \quad (2.41)$$

where the  $\mu_i$  are material constants and  $K$  is the Bulk modulus.

### Governing equations of Lagrangian formulation

We consider a body  $\mathcal{B}$  which occupies in the reference configuration the domain  $\Omega_0$  with a boundary  $\Gamma_0$ . The governing equations for the mechanical behavior of a continuous body are:

1. Conservation of mass  $\rho_1 J = \rho_0$
2. Conservation of linear momentum  $\nabla \cdot P + \rho b = 0$
3. Conservation of angular momentum  $F \cdot P = P^T \cdot F^T$
4. Constitutive equations
5. Measure of strain  $E = \frac{1}{2}(C - I)$
6. Boundary condition:  $e_i \cdot N \cdot P = e_i \cdot \bar{t}$  on  $\Gamma_0^{t_i}$
7. Internal continuity condition:  $\llbracket e_i \cdot N \cdot P \rrbracket = 0$  on  $\Gamma_0^{int}$

Where we note  $\Gamma_0^{t_i}$  the set of prescribed tractions  $\bar{t}$  on the body boundary  $\Gamma_0$ ; and  $\Gamma_0^{int}$  is the union of all surfaces where the stresses are discontinuous in the body (material interfaces).

The momentum equation together with the traction boundary condition and the interior traction continuity condition are called the generalized momentum balance (GMB) .

## 2.2 Finite Element Discretization

In continuous mechanics the body deformation is expressed in terms of partial differential equations (PDE). For the majority of problems, the PDE cannot be solved analytically, therefore approximation methods are developed. To this end, the finite element (FE) method has become the standard numerical calculation to compute such approximations. The computational domain, the unknown solution, and its partial derivatives are discretized, so as to obtain a set of algebraic equations for the function values at a finite number of discrete locations. The unknowns of the discrete problem are associated with a computational mesh which represents a subdivision of the domain  $\Omega_0$  into many small control volumes  $\Omega_k$

### 2.2.1 Eulerian and Lagrangian mesh description

The mesh description depends on the chosen independent variables (Eulerian or Lagrangian formulation). An Eulerian mesh formulation is usually used to solve problems linked to fluid like materials, and a Lagrangian mesh for solid like materials. In an Eulerian mesh, the Eulerian coordinates of nodes are fixed (coincident with spatial points) and the material points change in time (see Figure 2.5.b). In this case the mesh has to be large enough to contain the body in its current configuration. Throughout the deformation, the material points will belong to different elements. On the contrary, in a Lagrangian mesh, the Lagrangian coordinates of nodes are time invariant, nodal trajectory corresponds with material points trajectory and no material passes between elements (see Figure 2.5.a).

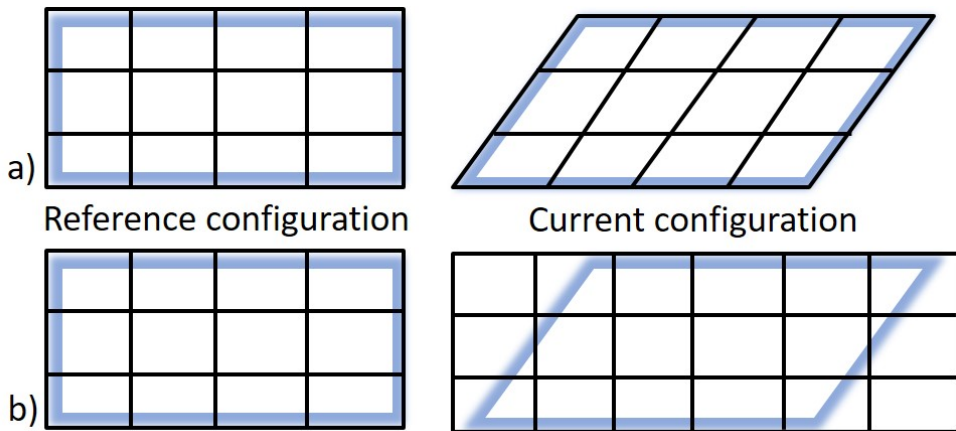


Figure 2.5: a) Lagrangian mesh formulation. b) Euler mesh formulation

In a Lagrangian mesh, the boundary and interface nodes remain coincident with body boundaries and material interfaces throughout the entire deformation. Thus, the boundary conditions are defined directly on the respective nodes. On the other hand, in an Eulerian mesh, the boundary and interface conditions have to be defined on points which are not nodes. This implies important complications in multi-dimensional problems.

An important drawback of a Lagrangian mesh affects mainly the large deformation domain. As the nodes are coincident with the material points, the elements deform with materials. Therefore, the magnitude of deformation is limited because of the element distortion. The limited distortion that most elements can sustain without performance degradation or failure is an important factor in nonlinear analysis with Lagrangian formulation.

### 2.2.2 Lagrangian mesh

The general approach of the FE method in Lagrangian formulation is illustrated in Figure 2.6. First, the momentum equations with given boundary conditions are multiplied by a set of appropriate test functions. The test functions have to satisfy all displacement boundary conditions and to be smooth enough so that all derivatives in momentum equations are well defined. Then, performing an integration by parts, the weak formulation of GMB is obtained, also called the principle of virtual work [13].

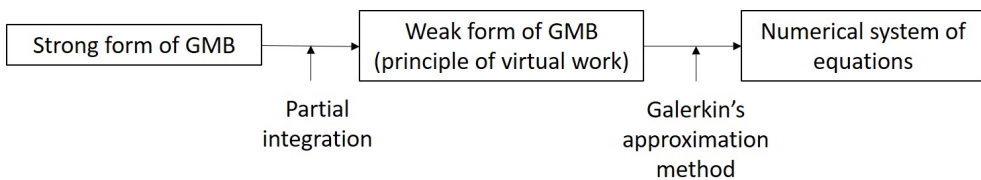


Figure 2.6: From strong formulation of the generalized momentum balance (GMB) to numerical equations.

The momentum equations and the traction boundary conditions, usually called the strong form, cannot be directly discretized by an FE method. The strong formulation of the GMB equations imposes the  $C_1$  continuity conditions on the field variables. Therefore, the solution of this problem does not always exist. This is true especially in the case of complex domains with different material interfaces. In order to overcome these difficulties, weak formulations are preferred. The weak formulation of the GMB reduces the continuity requirements thereby allowing the use of easy-to-construct and implement polynomials. Due to reduced requirements in function smoothness, the weak forms never give an exact solution, but one can obtain a relatively accurate solution with the discretization refinement.

From the weak form of the GMB equations, the numerical system of equations is formulated by using finite element interpolants for the mechanical displacement and the test functions. The whole domain is discretized into a number of smaller areas or volumes which are called **finite element** (or elements) and their assembly is called a **mesh**. Finite elements can be of various shapes (as shown in Figure 2.7.b), quadrilateral or triangular in two dimensions, and tetrahedral or hexahedron in three-dimensions.

The mechanical displacement is approximated at the discretization points called finite element **nodes**. The nodes are at the vertices of the finite elements for a linear type,

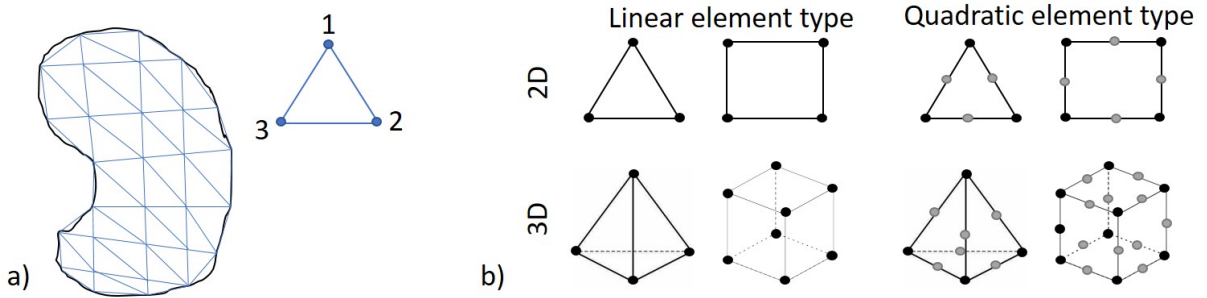


Figure 2.7: a) Discretization of a 2D domain with triangular finite element: Lagrangian mesh. b) Different types of finite elements

and at the vertices and mid-side of the finite element edges for a quadratic type (Figure 2.7.b). The displacement of each point within an element is interpolated from the values of the displacements of the nodes of the this element. In this way, the problem of finding the displacement of every point within the body is replaced by the problem of finding the displacements of a finite number of nodes.

As in a Lagrangian mesh the nodes are following the motions, for large deformations the finite elements can be highly distorted. Therefore, the element shape quality is generally checked all along the deformation process. Several shape parameters for each element type have been proposed, such as: aspect ratio, maximum corner angle, Jacobian ratio, skewness, parallel deviation, warping factor. The acceptable limit values of these shape factors are proper to the element types. In the following, only the shape parameters of the linear triangular elements are presented [7].

### Triangle aspect ratio

The element's shape aspect ratio is computed using only the vertices, corner nodes, of the element (Figure 2.8). First, two lines are created: one through a node ( $K$ ) and the midpoint of the opposite edge ( $K'$ ), the second through the midpoint of the others two edges ( $J'$  and  $I'$ ). Then two rectangles are created, with each rectangle having a pair of edges parallel to one of the previously defined lines. The rectangle edges have to pass through the nodes and the triangle's edge midpoints. This construction is repeated for each triangle's node resulting in 6 rectangles. The aspect ratio of a rectangle is defined as the ratio between the longer and shorter sides. Thus, the triangle's aspect ratio is defined as the maximal aspect ratio over the 6 rectangles divided by squared root of 3.

The best possible aspect ratio is 1 and is represented by an equilateral triangle. An element with an aspect ratio larger than 20 is considered as a bad aspect element, because large aspect ratio may degrade solution performance.

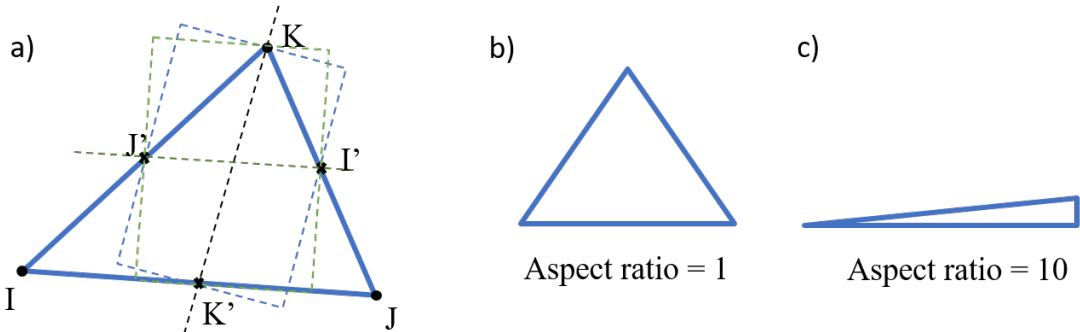


Figure 2.8: Computation of the aspect ratio for a triangle

### Triangle maximum corner angle

The maximum corner angle is computed using nodes position in 3D space. The best possible maximum corner angle is  $60^\circ$ . An element having a maximal corner angle larger than  $165^\circ$  is considered as a bad shape element, because large corner angles may degrade the solution performance. Figure 2.9 shows a triangle with a good ( $60^\circ$ ) and bad ( $165^\circ$ ) quality.

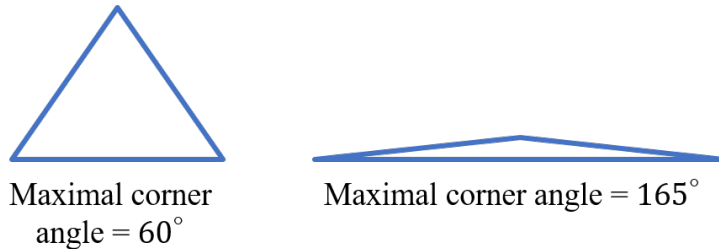


Figure 2.9: Example of triangles with different maximal corner angles.

The aspect ratio and the maximal corner deviation of a tetrahedra is computed using the definition of the same measure on a triangle. The element shape parameter is assigned as the worst value over the triangles defined by the tetrahedra's faces and cross-sections.

### Skewness

The skewness of a triangular element is computed using the equivalent volume deviation method. It is defined as the difference between the optimal and real cell size over the optimal cell size. The optimal size is the size of an equilateral cell with the same circum radius. According to its definition, the value of 0 indicates an ideal cell, from 0 to 0.75 the cell is considered to have a good quality, from 0.75 to 1 the cell is considered to have a bad quality and a value of 1 indicates a completely degenerated cell (Figure 2.10).

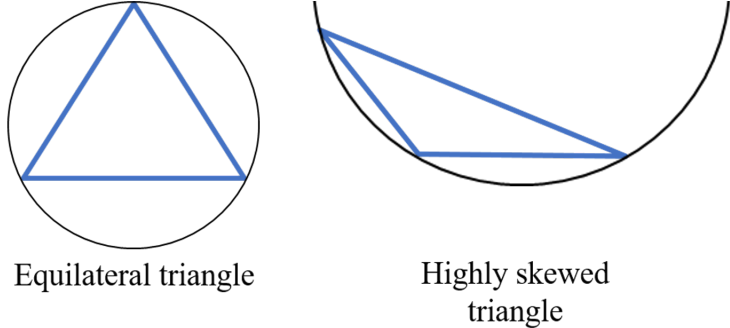


Figure 2.10: Example of triangles with different skewness with the corresponding circum radius.

## 2.3 Contact mechanics

In order to transfer the loads between elements, the nodes have to be connected together. If two bodies are separated with no common nodes, no interaction will occur during the deformation and the bodies will pass through each other. Here, an asymmetric surface-to-surface contact method is used to solve the multi-body interaction problems.

Let's consider two different bodies  $\mathcal{A}$  and  $\mathcal{B}$  and their occupied domains  $\Omega_A$  and  $\Omega_B$  with boundaries  $\Gamma_A$  and  $\Gamma_B$  respectively (see Figure 2.11). Also, we note  $\Omega$  the domain of intersection of two bodies. The contact interface is the intersection of the surfaces of the two bodies:

$$\Gamma = \Gamma_A \cap \Gamma_B. \quad (2.42)$$

The intersection consists of two surfaces, usually distinguished as **target** and **contact** surfaces. For an asymmetric contact each surface has a single designation and the choice of the surface types is made following these next guidelines (the target surface property are enumerated in their priority order):

- If the body  $\mathcal{A}$  is stiffer than the body  $\mathcal{B}$ , the surface  $\Gamma_A$  defines the target and  $\Gamma_B$  the contact surface.
- If  $\Gamma_A$  is a concave surface getting in contact with the convex surface  $\Gamma_B$ , the surface  $\Gamma_A$  defines the target and  $\Gamma_B$  the contact surface.
- If  $\Gamma_A$  is larger than  $\Gamma_B$ , the surface  $\Gamma_A$  denotes the target and the surface  $\Gamma_B$  the contact surface.

For the following, we identify  $\Gamma_A$  as the target surface and  $\Gamma_B$  as the contact surface (Figure 2.11).

Sometimes, the asymmetric contact does not provide satisfactory results and a symmetric contact is needed. When defining a symmetric contact, each surface coming in contact is designated to be both contact and target surface types. Therefore, two sets of contact

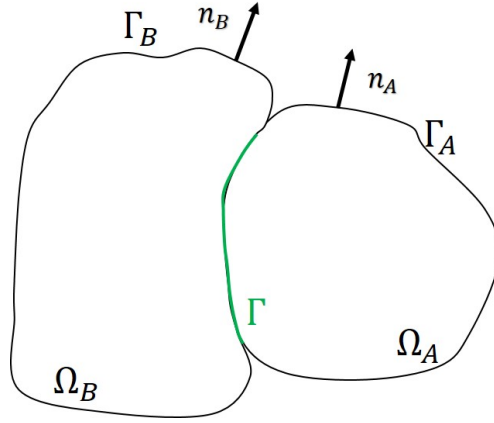


Figure 2.11: Multi-body contact problem.

pairs are defined. The symmetric contact may be used when the distinction between the contact and the target surfaces is not clear or to reduce the contact penetration. However, it usually results in a more time-consuming solution.

### 2.3.1 Contact interface equations

In the case of multi-body interaction, besides the standard mechanical governing equations, two additional contact conditions have to be fulfilled: the two bodies cannot interpenetrate, and the traction must satisfy momentum conservation on the contact interfaces.

#### Traction conditions

Traction conditions must follow the balance of momentum across the contact interface:

$$t_A + t_B = 0 \quad (2.43)$$

On the contact boundary surface  $\Gamma$ , the traction vector is decomposed into its normal and tangential components:

$$t_A^n = t_A \cdot n_A, \quad t_B^n = t_B \cdot n_B$$

$$t_A^t = t_A - t_A^n n_A, \quad t_B^t = t_B - t_B^n n_B$$

Therefore the momentum balance requires:

$$t_A^n + t_B^n = 0, \quad t_A^t + t_B^t = 0 \quad (2.44)$$

### Inter-penetrability condition

The bodies implied in a multi-body problem must fulfill the inter-penetrability condition:

$$\Omega_A \cap \Omega_B = 0 \quad (2.45)$$

Decomposing the displacement  $u$  into its normal and tangential components,  $u^n$  and  $u^t$  respectively, the inter-penetrability condition can be written as:

$$t^n \leq 0, \quad u^n - gn_A \leq 0, \quad t^n(u^n - gn_A) = 0 \quad (2.46)$$

Where  $g$  is the gap between the two bodies and  $n_A$  is the normal to the target surface.

### 2.3.2 Surface interaction models

When two solid bodies are placed together under a nonzero normal force and act one over the other with a tangential force, a **friction force** ( $f_{friction}$ ) tangential to the interface and opposite to the applied force is created. Depending on whether the applied force can overcome or not the opposing friction force, the bodies may or may not move relative to each other. The body motion along the interface is called **sliding**. The **sliding force**,  $f_{sliding}$  is the resulting tangential force which causes the sliding motion between the two bodies.

According to the allowed relative body motion in tangential or normal directions, five types of surface interaction models can be distinguished: bonded, rough, no-separation, frictional and frictionless. Table 2.1 resumes each corresponding mechanical behavior. If the body motion is not allowed in normal or tangential directions, once the bodies get in contact, the respective components of traction are equals ( $t_A = t_B$ ). This means that, for a pure **bonded** contact, the two bodies are considered as a unique solid body.

Name	body motion in normal direction	body motion in tangential direction
Bonded	No	No
Rough	Yes	No, $f_{friction} \gg f_{sliding}$
No-separation	No	Yes, $f_{friction} = 0$
Frictionless	Yes	Yes, $f_{friction} = 0$
Frictional	Yes	Yes, if $f_{sliding} > f_{friction}$

Table 2.1: Surface interaction models and corresponding mechanical behaviors

The *frictional* contact behavior is defined using Coulomb friction law. For a continuous body, the Coulomb friction model is applied at each point of the contact interface. Considering that bodies  $\mathcal{A}$  and  $\mathcal{B}$  are in contact within the surface  $\Gamma$ , then for all  $x \in \Gamma$ :

$$\text{if } \|t^t(x)\| < -\mu_f t^n(x), \quad \Delta u^t = 0 \quad (2.47)$$

$$\text{if } \|t^t(x)\| = -\mu_f t^n(x), \quad \Delta u^t = -k(x)t^t(x), \quad k(x) > 0 \quad (2.48)$$

Where  $\mu_f$  is the material property named **friction coefficient**,  $\Delta u^t$  is the slip incremental in the tangential direction and  $k(x)$  is a variable computed from the momentum equation. The equation (2.47) is known as the sticking condition: the tangential traction is lower than the critical value, thus no sliding occurs. Reciprocally, equation (2.48) is called the sliding condition.

When a frictionless contact model is used,  $\mu_f = 0$ , the tangential tractions vanish completely:  $t_A^t = t_B^t = 0$ . On the contrary, when a rough contact is modeled, the friction coefficient  $\mu_f$  is equal to infinity, so that the sticking condition is always fulfilled.

In practice, several contact models can be combined to model a physical contact between two bodies.

### 2.3.3 Contact formulation algorithm: pure penalty model

#### Pinball region

Contact formulation presents two primary difficulties from a computational point of view. The first, is the unknown traction conditions for each considered frictional model. And second, the regions which will get in contact during the deformation process can not be predicted.

The region of contact depends on materials properties and imposed boundary conditions. Therefore, it is difficult to know a priori where the surfaces will be in contact. To formulate analytic equations, one has to know exactly the nodes involved in the contact process. Therefore, during body deformation, the program searches if the contact is *opened* or *closed*. The status is defined using a sliding pinball (Figure 2.12). The pinball slides over the contact surface nodes and searches for the target surface. If the node to surface distance is smaller than the pinball radius, the contact is considered to be closed (Figure 2.12, green nodes). Otherwise the contact is considered to be opened (Figure 2.12, gray nodes).

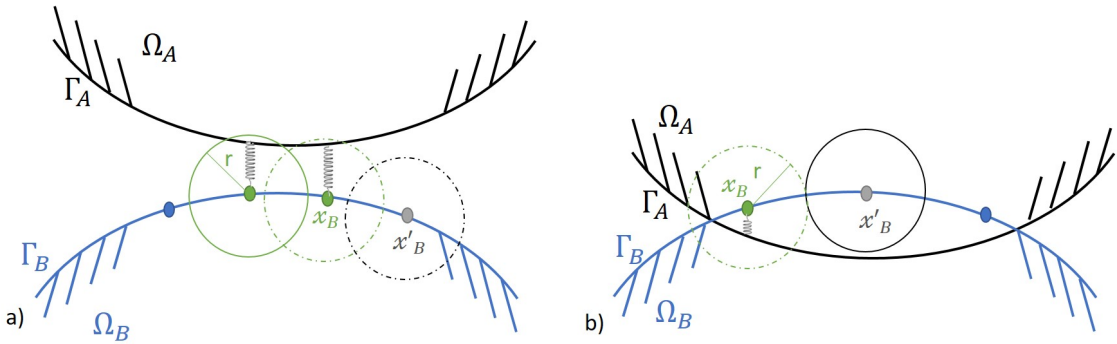


Figure 2.12: Contact status update using a pinball of radius  $r$ . Green nodes - updated nodes to closed contact status; gray nodes - updated nodes to open contact status; blue nodes - nodes which contact status need to be updated

### Gap and penetration measures

Let's consider a point  $x_B$  belonging to the body surface  $\Gamma_B$ , and  $x_A$  the intersection point of the surface normal  $n_B$  with the surface  $\Gamma_A$  (Figure 2.13). The point to surface distance  $d_1(x_B, \mathcal{A})$  is defined as:

$$d_1(x_B, \mathcal{A}) = \|x_B - x_A\| = \left[ \sum_{i=1,2,3} (x_B^i - x_A^i)^2 \right]^{\frac{1}{2}} \quad (2.49)$$

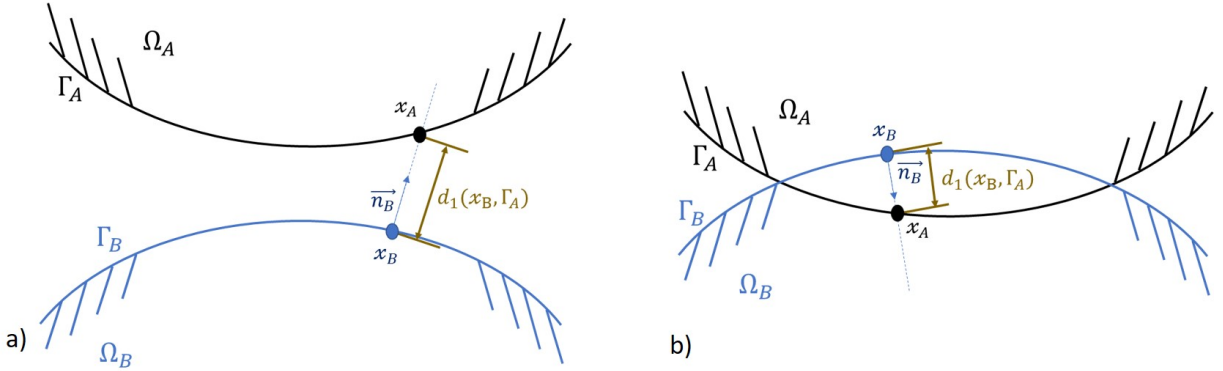


Figure 2.13: a) Body  $\mathcal{A}$  and body  $\mathcal{B}$  are close but not in contact. The  $d_1(x_B, \mathcal{A})$  measure define the gap between the bodies at point  $x_B$ . b) Body  $\mathcal{B}$  have penetrated the body  $\mathcal{A}$ . The  $d_1(x_B, \mathcal{A})$  measure gives the penetration at point  $x_B$ .

If the intersection point  $x_A$  is located inside the pinball area, the node to surface distance defines the amount of **gap** or **penetration** of the respective node (Figure 2.13).

Computing the gap or the penetration at single points increases numerical instabilities. Therefore, in this work, surface projection based contact method proposed by ANSYS was used. In Figure 2.14 the computation method of each projected area over the contact surface is explained. Figure 2.14.a represents the contact surface elements and Figure 2.14.b represents the target surface elements. If the two surfaces are overlapped, each unique area becomes a surface projected contact area (Figure 2.14.c). Therefore instead of calculating the penetration or the gap at each element node, the method computes an average value for each overlapping area.

This approach provides a more accurate calculation of contact traction and stresses for the underlying elements, however it is computationally more expensive. The interested reader is referred to ANSYS contact technology guide [6] for more details on the contact modeling.

### Finite element mesh

For the finite element computation, contact and target surfaces have to be discretized with 2D linear or quadratic elements (Figure 2.7) consistent with the underling 3D element mesh. The elements are named contact and target elements respectively. They have no

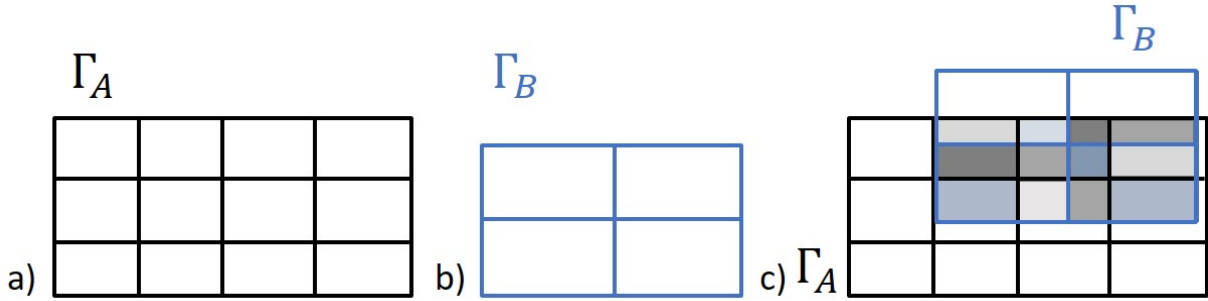


Figure 2.14: The contact surface projection over the target surface: a) Target surface elements; b) contact surface elements; c) surface projected contact areas.

material properties apart the friction coefficient  $\mu_f$ . The stress-strain as well as the gap or penetration measures are computed for each mesh node of the discretized surface.

### Pure Penalty method

In this manuscript, one of the most popular mathematical expression of contact compatibility conditions is used, namely the penalty method. With such a method, additional contact properties are defined to manage contact behavior: a normal stiffness factor, opening stiffness factor, and a tangential stiffness factor. Such factors play an important role in the numerical computation but have no physical meaning.

The penalty method uses a spring like relationship to introduce a force for all nodes pairs (contact-target) that are defined to be in closed contact (Figure 2.49). The contact force is computed using the following expression:

$$f_c = k_c d \quad (2.50)$$

where  $d$  represents the penetration or gap amount and  $k_c$  is the normal stiffness factor or the opening stiffness factor respectively. The tangential stiffness factor works in the same way enforcing the responding frictional force. Even if physical contacting bodies do not interpenetrate ( $d = 0$ ), some finite amount of penetration,  $d > 0$ , is required mathematically to maintain equilibrium.

The magnitude of the stiffness contact factors is unknown beforehand which make difficult a proper estimation of contact mechanics. The contact force at each node have to be large enough to push the contact surface back to the target surface and eliminate unwanted penetration or gap. At the same time, if the contact force is too large, it pushes the contact surface far away from the pinball region causing error and solution instabilities.

## 2.4 Breast biomechanical model: an overview

Biomechanical modeling of breast tissues has been widely investigated for various medical applications such as surgical procedure training, pre-operative planning, diagnosis and

clinical biopsy, image guided surgery, image registration, and material parameter estimation (Table 2.3). For the last 20 years, several research groups have presented their breast models based on finite elements theory. The complexity and relevance to breast anatomy of each model depend on the research purpose for which it was designed.

Several groups have proposed biomechanical breast models to register uncompressed volumetric breast data sets to compressed ones [67, 124, 133] or to compressed mammography projections [80]. Within this framework, the authors modeled the breast deformation from prone to compressed prone position assuming linear elastic materials, zero residual stress and Dirichlet boundary conditions. However, compression-like breast deformation is too limited to characterize global breast mechanics.

Applications such as image guided surgery or preoperative planning imply a wider range of deformations. Therefore biomechanical breast models capable of estimating gravity induced deformation between different body position were proposed, for example from supine to prone positions (named also multi-loading gravity simulations) [52, 60, 44]. Considering the involved large deformations, these models need to be more accurate with respect to mechanical and anatomical breast properties. In this respect, a patient-specific model is needed considering more personalized boundary conditions, material models and a better representation of breast anatomy.

As described in Section 2.1, to build such a mechanical breast model, one needs to provide the breast geometry in a **reference configuration**, the **constitutive models** of tissues composing the breast volume and the **boundary conditions**. A proper definition of all these variables has a significant impact on model accuracy.

### 2.4.1 Breast reference configuration

A large number of existing patient specific models are using volumetric data from MR images [20, 80, 30, 42, 91] or CT images [105, 133] to design the breast geometry. During the acquisition of such images, the breast tissues are already under large deformations implying significant changes of breast geometries, for example if the patient is in a supine or in a prone position. Moreover, the deformed breast configurations include already the initial pre-stresses which are generally unknown and are extremely difficult to measure in clinical conditions.

To model the breast tissues deformation under gravity loading, the reference state is chosen to be the breast geometry in a stress-free configuration, i.e. without being deformed by any force, including gravity. The breast stress-free geometry is practically impossible to measure; therefore, several estimation methods have been proposed. The four most used methods are described below.

#### Inverse gravity

Palomar A.P. et al. [105] and Sturgeon G.M. et al. [133] used the inverse gravity method to estimate the stress-free geometry from the prone position measured using MRI modality. In their works, the authors just reversed the gravity effects without considering the initial

stresses already included in the breast prone configuration. However, it has been proved that the inverse gravity method gives a poor approximation of the breast reference state and can be used only with small deformations or highly constrained models [43].

### Breast neutral buoyancy configuration

Assuming that breast density is equal to water density, Rajagopal V. et al. [119] compute the breast stress-free configuration by imaging the breast immersed in water. Following the same physical assumptions, Kuhlmann M. et al. [86] proposed to estimate the stress-free configuration by applying a hydro-static distributed load on the breast surface collected in a prone configuration. Although the estimated geometries are relatively accurate, these methods are time-consuming and are difficult to transpose in a clinical framework.

### Prediction-correction iterative algorithm

The prediction-correction iterative method was first proposed by Govindjee S. and Mihalic P.A. [61] and adapted later by Carter T. [20] and Eiben B. et al. [43]. The original method is based on the prediction-correction iterative scheme represented in Figure 2.15. The first approximation of the breast reference configuration is estimated by applying the inverse gravity method on the prone breast configuration (see above). Then, a numerical breast prone configuration is computed and compared to the corresponding measured one. The difference between the two prone geometries (the measured one and the simulated one) is used to update the reference breast configuration. The process is repeated until the convergence is achieved (i.e. when the difference is minimal). These methods were validated using the breast shape in the neutral buoyancy configuration.

### Inverse FE algorithm

Pathmanathan P. et al. [108] and later Vavourakis V. et al [141] proposed an analytic computation of the breast reference state by reparametrizing the equilibrium equation and by solving a finite element formulation of the inverse motion. The model provides good estimates of breast reference configurations but needs important numerical resources. Eiben B. and colleagues [43] showed that the prediction-correction iterative algorithm and the inverse FE algorithm are similar in terms of resulting accuracy.

## 2.4.2 Constitutive models

Global breast mechanics is governed by breast internal consistency and tissues' individual mechanical properties. The breast soft tissue is known to be incompressible, nonlinear, anisotropic, and viscous materials. However, even for small time scales loads the breast tissues viscosity can be neglected [142].

Under large compressions, the breast volume can vary due to fluids (blood and lymph) flows. Thus, soft tissues are not considered as totally compressible materials, and are frequently modeled as quasi-incompressible with a value of the Poisson ratio  $\nu$  ranging

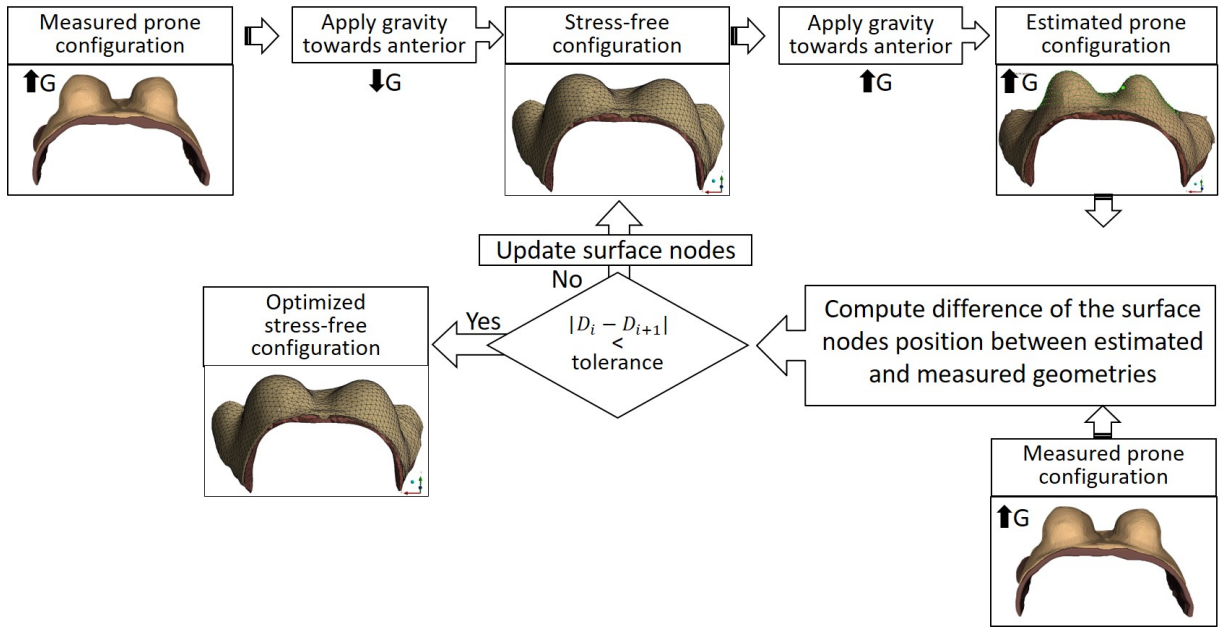


Figure 2.15: Prediction-correction algorithm

between 0.45 and 0.5. The influence of the Poisson ratio within linear constitutive models was studied by Tanner C. and colleagues [136]; according to the authors, the best breast geometry estimates are obtained with high Poisson ratio ( $\nu = 0.495 - 0.499$ ). The breast tissues being predominately composed of water, the density is considered to be equal to  $981 \text{ kg/m}^3$ .

For the last decades, several constitutive models were used to model the breast tissues response to an external force: exponential elastic [11], Neo-Hookean hyper-elastic [20, 120, 133, 41, 66, 53] and Mooney-Rivlin models [127, 136, 19, 91]. The most used models are analyzed in the following section.

### Glandular and adipose tissues biomechanical properties

Multiple studies have shown that breast composition, and therefore its mechanical behavior, undergo substantial changes during woman lifetime (section 1.1.4). The first studies on mechanical proprieties estimation of breast tissues were done for diagnosis purposes. When the breast is developing benign or malign disorders, its mechanical properties differ from the ones of the normal breast tissues [85].

Later, several research groups (Table 2.2) have studied the elastic modulus of adipose and glandular tissues. The breast tissue Young's modulus range between  $0.1 \text{ kPa}$  and  $271.8 \text{ kPa}$ . Such huge variation may be explained by the differences in the experimental setups used to estimate tissues stiffness, but also by the participant's physical condition, age or period in the menstrual cycle. For example, Han L. et al. [67], though using the same FE method, found significantly inter-individual variability, with the shear modulus ranging between  $0.22$  and  $43.64 \text{ kPa}$ . Lorenzen J. and team [89], showed that during the

*CHAPTER 2. BIOMECHANICAL BREAST MODELING  
STATE OF THE ART*

---

menstrual cycle, due to the hormonal changes, the elastic properties of the glandular tissues can change by about 30%.

Ex-vivo estimation				
Author	Method	Material model	material properties	
			Adipose kPa	Glandular kPa
Krouskop T.A. et al. [85]	Indentation- 5%	Linear elastic	$\lambda = 19 \pm 7 \text{ kPa}$	$\lambda = 33 \pm 11 \text{ kPa}$
Krouskop T.A. et al. [85]	Indentation- 20%	Linear elastic	$\lambda = 20 \pm 6 \text{ kPa}$	$\lambda = 57 \pm 19 \text{ kPa}$
Wellman P. et al. [142]	Indentation - 5%	Linear elastic	$\lambda = 6.6 \text{ kPa}$	$\lambda = 33 \text{ kPa}$
Wellman P. et al. [142]	Indentation - 15%	Linear elastic	$\lambda = 17.4 \text{ kPa}$	$\lambda = 271.8 \text{ kPa}$
Azar F.S. et al. [11]	Indentation	Exp. elastic	$b = 4.46 \text{ kPa}; m = 7.4$	$b = 15.1 \text{ kPa}; m = 10$
Samani A. et al. [126]	Indentation	Linear elastic	$\lambda = 3.25 \pm 0.91 \text{ kPa}$	$\lambda = 3.24 \pm 0.61 \text{ kPa}$
In-vivo estimation				
Van Houten E.E. et al. [139]	MRE	Linear elastic	$\lambda = 17 - 26 \text{ kPa}$	$\lambda = 26 - 30 \text{ kPa}$
Sinkus R. et al. [130]	MRE	Visco-elastic	$\mu = 2.9 \pm 0.3 \text{ kPa}$	
Rajagopal V. et al. [119]	MRI-FEM	Neo-Hookean	$\mu = 0.16 \text{ kPa}$	$\mu = 0.26 \text{ kPa}$
Carter T. [18]	MRI-FEM	Neo-Hookean	$\mu = 0.25 \text{ kPa}$	$\mu = 0.4 \text{ kPa}$
Han L. et al. [67]	MRI-FEM	Neo-Hookean	$\lambda = 1 \text{ kPa}$	$\lambda = 0.22 - 43.64 \text{ kPa}$
Gamage T. et al. [52]	MRI-FEM	Neo-Hookean	$\mu = 0.1 \text{ kPa}$	
Griesenauer R.H. et al [62]	MRI-FEM	Hooks law	$\lambda = 0.25 \text{ kPa}$	$\lambda = 2 \text{ kPa}$

Table 2.2: Material properties for adipose and glandular tissues.

An important difference in estimated values of breast elastic modulus is observed between the linear elastic and hyperelastic models. Considering only in-vivo studies with Neo-Hookean material models, the adipose and glandular shear modulus values are lower than 50kPa.

Carter T. [20] compared a one parameter Neo-Hookean potential function with a five-parameter Mooney-Rivlin potential function for various constitutive parameters. The multi-loading gravity simulations were thus performed on 3 subjects. According to the

authors, even with parameters 10 times softer than described in the literature [125], the Mooney-Rivlin model underestimates the tissues deformation by at least 75% (prone to supine loading simulation). The best estimates were given by the Neo-Hookean model with the initial shear modulus equal to  $0.2kPa$ .

Previously listed researches clearly showed the variability of elastic modulus of the same tissue between and within individuals. Eder M. [40] made a larger analysis including all material models proposed in the literature. According to authors, many of them are too stiff, permitting not enough deformation within the gravity loading. This study has shown that the most reliable values of the elastic modulus are the ones given by Rajagopal V. and colleagues [119] (Table 2.2).

### **Muscle biomechanical properties.**

Muscle is a kinematically, geometrically, and materially complex tissue. The muscle mechanical behavior depends on its contractile active and passive elastic properties [99]. In biomechanics the muscle is modeled using complex models such as Hill-type models [151], Feldman's lambda model [46] which are considering the variation of muscle elasticity as function of the muscle state. For breast biomechanical modeling, the muscle is combined with the thoracic cage and is frequently considered as a rigid breast support. In most of cases, the pectoral muscle is modeled by imposing zero-displacement conditions on nodes closer to the chest wall [125, 27, 117] or by allowing them to slide along the chest wall line [66, 60].

The muscle is a nonlinear, anisotropic, incompressible material. The bibliographic data on static mechanical properties of the muscle-tendon unit assessed by supersonic shear wave imaging elastography states a Young's modulus ranging between  $20kPa$  and  $300kPa$  depending on the muscle location and subject's physical condition [88]. The muscle shear modulus on the upper trapezius was studied by Leong H. T. et al [87]. According to the authors, the muscle shear elasticity at rest was  $17.11 \pm 5.82kPa$ , and it increased to  $26.56 \pm 12.32kPa$  during active arm holding at 30 degrees abduction.

### **Skin biomechanical properties**

Several studies have shown the importance of considering the skin in biomechanical breast modeling. According to Carter T. [20], a model which includes the skin better estimates the tissues deformations under gravity loading.

Sutradhar A. and Miller M.J. [134] published a complete study about breast skin, estimating its elasticity for 16 different breast regions. The study was done on 23 female volunteers aged from 29 to 75 years old. The authors found that the skin elastic modulus ranges between  $15$  and  $480kPa$  with an average of  $334 \pm 88kPa$ . The elastic modulus in the lateral region has the highest value (mean  $370kPa$ ), followed by the superior region (mean  $355kPa$ ). The inferior region (mean  $331kPa$ ) follows next, with the medial region having the lowest value (mean  $316kPa$ ). However, no significant variation of the elastic modulus in radial direction was found.

Other researches on skin elasticity are available, but they are not specific to the breast skin. Hendriks F. and colleagues [69] estimated in-vivo skin properties by suction testing. The skin was considered as a homogeneous, isotropic, incompressible, hyperelastic material. The study was performed on 14 subjects, and the average value of the elastic modulus for skin was  $58.4\text{kPa}$ .

The estimation of the breast skin elasticity by the means of finite elements using Neo-Hookean potential function has resulted in softer materials model. Carter T.[18] found an initial shear modulus equal to  $16\text{kPa}$ , whereas Han I. et al [66] found that for the five studied subjects, the skin shear modulus ranged between  $2.47\text{kPa}$  and  $5.78\text{kPa}$ .

### **Fascias and ligaments biomechanical properties**

The surrounding breast fascias and the supervisory ligament form the breast support matrix. These structures are well described for surgical purposes (thickness, location etc), however little is known about their mechanical properties. The first biomechanical breast model taking into account the effect of Cooper's ligaments was proposed by Azar F. and colleagues [11] and took up later by Pathmanathan P. et al [108] and Han L. et al [67]. The authors designed a new material model for fatty tissues including the anisotropic behavior of breast ligaments. Later, Georgii J. and colleagues [60] came up with a spring-mass generic model for the breast support matrix. According to the authors, including the ligaments into the finite elements breast model increased the robustness of the prone-supine simulation with respect to the input parameters.

To our knowledge, there is no experimental data, available in the literature, describing the mechanical properties of breast superficial fascia. An approximation of the elastic modulus of Cooper's ligaments is provided by Gefen A. [57] by extrapolating known ligamentous structure in the human body. The authors estimated the elastic modulus of suspensory ligaments ranging between  $80$  and  $400\text{MPa}$ .

Fibrous tissues get their elasticity from elastin fibers and their structural support from collagen fibers. As reported by Riggio E. et al [121], the superficial fascia is made up of both collagen and elastin fibers. In contrast, the Cooper's ligaments appeared to be composed almost of collagen fibers. The mechanical properties of a single collagen fiber from a rat tail were studied by Wenger M.P. et al. [143]; according to the authors the corresponding elastic modulus ranges between  $5 \text{ GPa}$  and  $11 \text{ GPa}$ . Other studies on biomechanical characterization of human body superficial fascia from various regions are available in the literature. The most frequently studied structures are the plantar fascia and foot ligaments, with a Young's modulus ranging between  $0.1\text{kPa}$  [56] and  $700\text{MPa}$  [25].

#### **2.4.3 Boundary conditions**

Breast deformations can be modeled by solving the motion equations using two different types of boundary conditions, regarding either displacements (Dirichlet conditions) or forces (Neumann conditions).

Dirichlet conditions are usually used to constrain the sternum/axilla ends and the posterior surface of the breast or the thoracic cage if the muscular tissues are considered [62, 119, 108, 52, 62]. As reported by Carter T. [20] the zero-displacement boundary conditions in a multi-gravity loading framework result in an over-constrained model. In that case, sliding conditions over the chest wall have to be considered.

Later, several teams using biomechanical breast models for multi-modality image registration or surgical planning showed that including the sliding boundary conditions [60, 66] improves the registration accuracy. However, for most studies in which a biomechanical model is designed for breast compression, tissues sliding over the chest wall is neglected and fixed boundary conditions are usually assumed [133, 91].

#### **2.4.4 Summary**

During the last decades, several breast biomechanical models were proposed. However, only a small part of them [20, 52, 66] were evaluated with respect to real tissue deformations. As we intend to build-up a subject-specific breast biomechanical model capable of estimating multi-loading gravity deformations, we will only consider as relevant the biomechanical models that were evaluated and compared with real data. In this chapter, three main challenges were identified: the estimation of the breast reference geometry, the estimation of subject-specific material properties and the definition of the boundary conditions and namely at the breast-muscle interface. State of the art of breast biomechanical models were developed by: Eiben B. et al [44], Han L. et al. [66], Gamage T. et al. [52].

Gamage T. and colleagues [52] proposed a finite element model capable to estimate the supine breast configuration from the prone one. The breast stress-free configuration was estimated using a prediction-correction iterative algorithm. The optimization process was performed by using as ground-truth the skin surfaces on prone configuration. Contrariwise, the material constitutive parameters were identified using the skin surface on supine breast configuration. Breast tissues sliding over the chest wall was considered partially by modeling the pectoral muscle as a soft structure and including it into the optimization process. The model accuracy was assessed for the supine breast configuration only. The root-mean-squared error (RMSE) was computed from the point to surface distances between the estimated and measured data. According to the authors, the breast supine geometry was estimated within an RMSE of 5mm (maximal distance of 9.3 mm).

Latter on, Han L. et al. [66] developed a breast biomechanical model for image registration. The estimates of supine breast configuration were computed for five subjects, and the accuracy was assessed by computing the Euclidian distance between anatomical landmarks. The mean Euclidian distance ranges between 11.5 mm and 39.2 mm (maximal Euclidian distance ranges between 20.3 mm and 61.7 mm). The authors modeled the elongation of the pectoral muscle using a contact sliding model. The material constitutive parameters were adapted to the patient's breast mechanics, the stress-free breast geometry was estimated by inverse gravity.

Finally, Eiben B. et al [44] proposed a new model to estimate the up-standing breast configuration from the prone one. The model was evaluated on 3 subject. The patient

*CHAPTER 2. BIOMECHANICAL BREAST MODELING  
STATE OF THE ART*

---

specific stress-free geometry was computed using an inverse finite elements u-p formulation. The material parameters were optimized such that the best fit in supine configuration is obtained. The model accuracy was measured in terms of the mean Eulerian Distance between manually selected internal landmarks. The supine breast configuration was estimated with a mean distance ranging between 12.2mm and 19.8mm. The model evaluation for the up-standing configuration was not presented.

In the next chapter, a new biomechanical model of the breast will be described. The proposed model considers the subject-specific breast geometry and elastic properties as proposed in previous models. However, breast tissues sliding over the chest wall is modeled by including new anatomical structures such as superficial fascia and suspensory ligaments. Finally, the model was evaluated by confrontation with real data collected from MR images.

Authors	Application	FE mesh	Material models	Boundary conditions	Stress-free config.
Azar F. et al. [11]	Computer assisted breast surgery	8-Node hexahedrons (trilinear isotropic elements)	Skin-elastic adipose,glandular-hyperelastic polynomial	Sliding between breast - thorax and breast-paddle	Prone breast geometry
Rajagopal V. et al. [118]	Breast compression	8-Node hexahedrons (tricubic Hermite elements)	Homogeneous , Neo-Hookean model	Zero-displacement BC	Buoyant breast in water
Pathmanathan P. et al. [108]	Image registration	8-Node hexahedrons (trilinear elements)	Homogeneous polynomial Skin exponential hyperelastic	Zero-displacement on muscle; Compression with imposed displacement	Inverse FE algorithm
Han L. et al. [66]	Image registration	4-Node tetrahedrons	Muscle, glandular, fatty, skin - Neo-Hookean model	Sliding on pectoral muscle	Inverse gravity
Gamage T. et al. [52]	Computer assisted breast surgery	8-Node hexahedrons (tricubic Hermite elements)	Homogeneous+ Neo-Hookean incompressible model	Zero-displacement BC on rib cage surface, Sternum, axilla ends, shoulder	PC iterative algorithm
Patete P. et al. [107]	Computer assisted breast surgery	4-Node tetrahedrons (trilinear isotropic elements)	Adipose , glandular, skin	Zero-displacement BC on the chest wall	PC iterative algorithm
Kuhlmann M. et al. [86]	image registration	4-Node tetrahedrons	Adipose, glandular- gel-like (Eulerian formulation); Skin - hyperelastic material (Lagrangian formulation)	Zero-displacement chest wall	PC iterative algorithm
Georgii J. et al. [60]	Surgery simulation	8-Node hexahedrons, 2-node 3D spars	homogeneous elastic material, Cooper's ligaments-generic mass-spring model	sliding BC (breast on the pectoral muscle)	NA
Eiben B. et al. [44]	Surgery outcome prediction	4-Node tetrahedrons	Fatty , glandular- Hookean model; exponential hyperelastic	Zero-displacement BC	Inverse FE algorithm
Garcia E. et al. [53]	3D breast lesion localization	4-Node tetrahedrons	adipose, glandular - Neo-Hookean models	zero-displacement BC	Prone breast configuration

Table 2.3: Breast biomechanical models



## A NEW BIOMECHANICAL BREAST MODEL EVALUATED ON REAL DATA

The state of the art in breast finite element modeling was presented in the previous chapter. Three models were identified representing the cutting-edge technologies in the field. The authors used prone MRI to estimate the breast reference geometry. The subject-specific constitutive parameters were chosen such that the best fit between the supine configuration estimate and the corresponding measured breast geometry was obtained. The models were evaluated using the measured and the estimated positions of superficial fiducial landmarks or internal anatomical landmarks in the supine breast configuration. As the optimization and evaluation processes were based on the same data, the model limitations must have been underestimated. For a better assessment of the accuracy of a breast biomechanical model, we think that the evaluation on a third breast configuration is required.

This chapter introduces a new biomechanical model developed by combining the best practices and concepts proved by previous works. To be as realistic as possible, our model considers breast heterogeneity, sliding boundary conditions, initial pre-stresses and personalized hyper-elastic properties of breast tissue. In addition, new types of soft tissue are included representing the breast support matrix. Moreover, our model was built using prone and supine breast configurations and was evaluated in supine tilted configuration ( $\tilde{45}$  deg) of the same volunteer.

In the first part of this chapter, the data acquisition protocol is described and details on numerical methods and software used to extract the subject-specific breast geometry are described. Next, the different components of the finite element mesh are presented and the mesh quality is assessed using shape parameters. Then, the assumptions on boundary conditions and materials models are explained. Finally, the model optimization process is detailed and results on subject-specific parameters and breast reference configuration are presented.

## 3.1 Geometry extraction

Geometry extraction is the first step in FE analysis, and it consists of obtaining the 3D surfaces of the breast. We use MR images to obtain the subject-specific breast volumes and the surrounding soft tissues distribution. Prior to surface extraction, the MRI volume is segmented and mapped to a single reference coordinate system. The next section describes the image acquisition protocol and the numerical method used to generate the 3D subject-specific breast geometry.

### 3.1.1 Data acquisition

The images were acquired using a Siemens 3T scanner with T2 weighted image sequences. The in-plane image resolution was  $0.5 \times 0.5$  mm, and the slice thickness was 0.6 mm. During the acquisition, the contact between the breasts and ~~the contours of~~ the relatively narrow MRI scanner tunnel, or with the patient body (arms or thorax), was minimized. Three different positioning configurations were considered: prone, supine and supine titled ( $\pm 15$  deg). These positions were chosen to assess the largest possible deformations

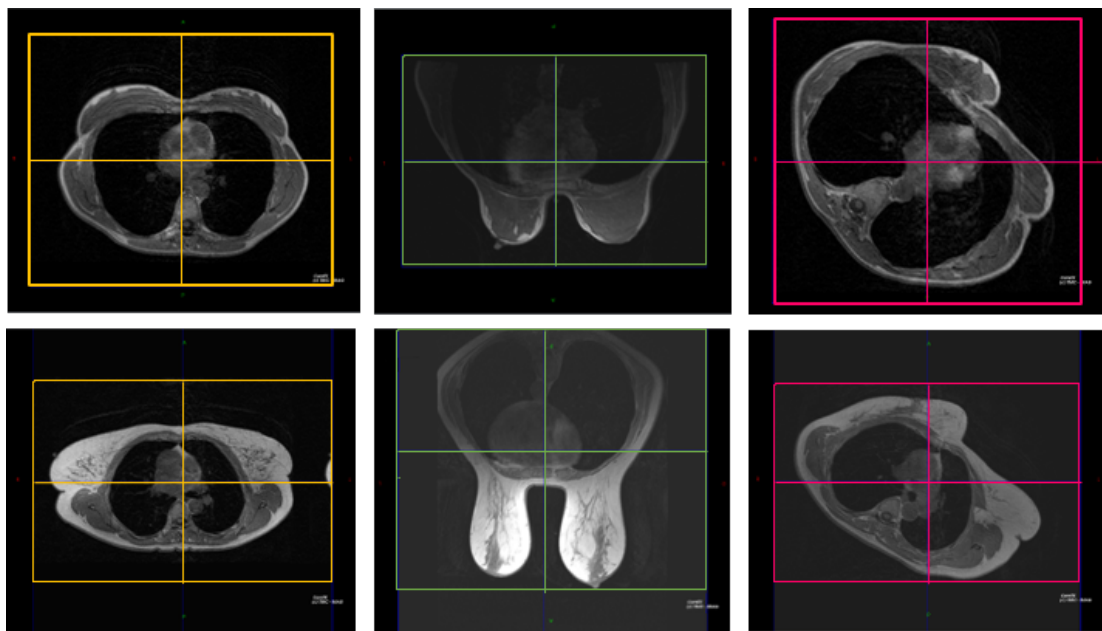


Figure 3.1: MR images in three breast configurations: first line - volunteer 1; second line - volunteer 2

Two volunteers agreed to participate in a pilot study approved by an ethical committee (MammoBio MAP-VS pilot study). The volunteers are 59 and 58 years old and have A-cup (volunteer 1) and F-cup (volunteer 2) breast size respectively.

Both volunteers were also asked to provide the compression force and breast thickness as measured during their most recent mammography. Such data are summarized in Table

### 3.1.

	Subject 1		Subject 2	
	Right breast	Left breast	Right breast	Left breast
Force (N)	21.9	40.9	94.8	56.6
Breast thickness (mm)	47	42	50	49

Table 3.1: Compression force and breast thickness for both subjects for a cranio-caudal mammogram

The biomechanical breast model that we propose was developed and evaluated using the MRI volumes of the first volunteer only. However, the breast deformation under compression simulations, detailed later in this manuscript, were performed for the both breast volumes.

#### 3.1.2 Image segmentation

A semi-automated active contour method proposed by ITK-Snap software was used to segment the pectoral muscle and the breast tissues from MR images [150]. To segment a tissue, the image is divided in several regions of interest (ROI, see Figure 3.2.a). For each ROI the segmentation of one tissue takes place in 3 steps (Figure 3.2):

1. First, the random forest algorithm [71] was used to compute the probability of each pixel to belong or not to the segmented tissue. Figure 3.2.c shows the synthetic volume corresponding to the previously selected ROI (Figure 3.2.b). In the new defined volume, the pixels were classified into background (blue) and breast tissues (gray) with a given probability (color intensity). The training data set for the random forest algorithm was manually selected by the user. It includes state and space characteristics such as voxel grey intensity, voxel's neighbors gray intensity (with variable radius of neighboring) and voxel position ( $x, y, z$ ) .
2. Then, spherical regions with variable radius, also names seed points, are placed manually into the new synthetic volume. The seed points mark all the connected components belonging to the segmented tissue (Figure 3.2.d.1).
3. Finally, the seed point contours evolves in the 3D space with a speed and direction derived from the pixel values in the synthetic volume (Figure 3.2.d.2-4). In Figure 3.2.c, the value of a pixel belonging to the background range between  $p_{val} \in [-1, 0]$ . Contrariwise, the value of a pixel belonging to the breast tissues range between  $p_{val} \in [0, 1]$ . Thus the point seeds contours expand over the positive regions and shrink over the negative ones. The propagation speed is proportional to the pixel intensity  $|p_{val}|$ . The process is stopped when the growing region covers up the entire relevant volume.

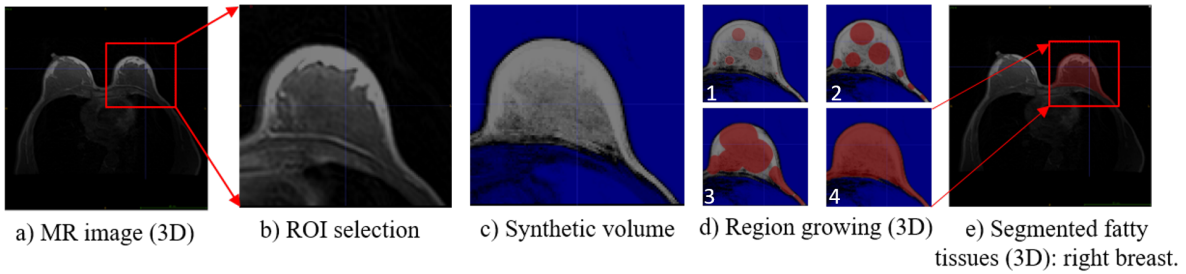


Figure 3.2: Breast tissues segmentation on the breast MRI of the second volunteer. Prone breast configuration.

The breast and pectoral muscle components are computed by merging the set of segmented ROIs. After segmentation, an additional manual correction was performed to refine the boundaries of each component. Simple erosion and dilatation operations were applied on segmented volumes in order to obtain smoother surfaces. Then, to avoid tissues overlapping at juncture border between the pectoral muscle and ~~breast~~, binary operations were used. First ~~the~~ ~~the~~ two segmented volumes were merged together to create a single volume. Then, from the full ~~component~~, the pectoral muscle volume was subtracted to redefine the breast volume without overlapping.

The process was repeated for both volunteers and for each breast configuration: supine, prone and supine tilted. The extracted surfaces in supine and prone configurations are used for model definition and optimization, the ~~last~~ surface, in supine tilted configuration, is used for model evaluation.

### 3.1.3 Image registration

During the imaging acquisition process, the subject was moved in and ~~outside~~ the MRI scanner tunnel. Therefore, the breast ~~does~~ not only undergo an elastic deformation, but also a rigid transformation. Prior to image acquisition, four landmarks were fixed on the chest wall in order to make image registration possible. The landmarks were placed on sternum and inframammary fold lines; these regions are indeed known to be rich in fibrous ligaments limiting the soft tissue elastic deformation. To assess the body position changes, a rigid transform is computed by minimizing the Euclidian distance between the two configurations of the four points defined by the four landmarks. The transformation is estimated using the iterative closest point (ICP) algorithm proposed by ITK library.

However, due to small local deformations of skin, the computed rigid transformation is not accurate enough. Therefore, a second registration step was performed by aligning the bone structures of the thoracic cage from prone and supine tilted positions to the supine one. The muscular tissues mask previously segmented ~~were~~ used in order to remove non-breast soft tissue. The image registration was implemented using a gradient descent based algorithm minimizing the image cross correlation (ITK library).

Figure 3.3 shows overlapping prone-supine and supine tilted-supine breast images of

the first volunteer in the transversal plane after registration. The registration error was assessed by computing the distance from the muscle's anterior surface in prone or supine tilted configurations to the muscle's anterior surface in supine configuration (Figure 3.4). The chest wall line of both volumes was well aligned, within an error of  $\pm 5 \text{ mm}$ . Higher differences may be observed because of elastic thoracic cage deformations due to hand position or body-mass force repartition. A maximal error of  $16.25 \text{ mm}$  is observed over the muscle surface in prone configuration in the region of the right arm, however these regions are out of the area of interest.

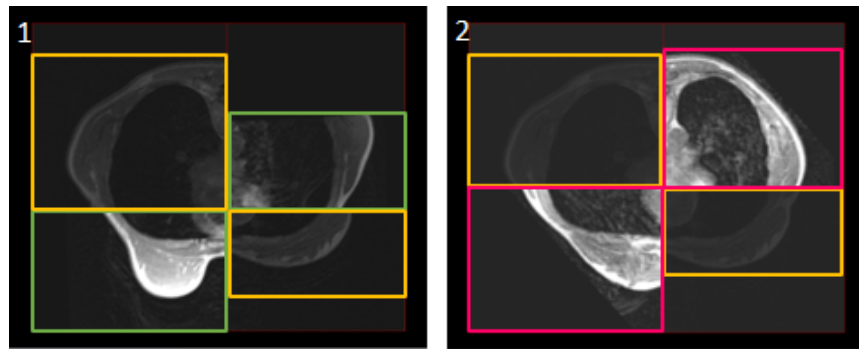


Figure 3.3: Registered MRI images for the first subject, 1) prone configuration versus supine; 2) supine tilted versus supine. Yellow frame - supine configuration; Green frame - prone configuration; Red frame - supine tilted configuration.

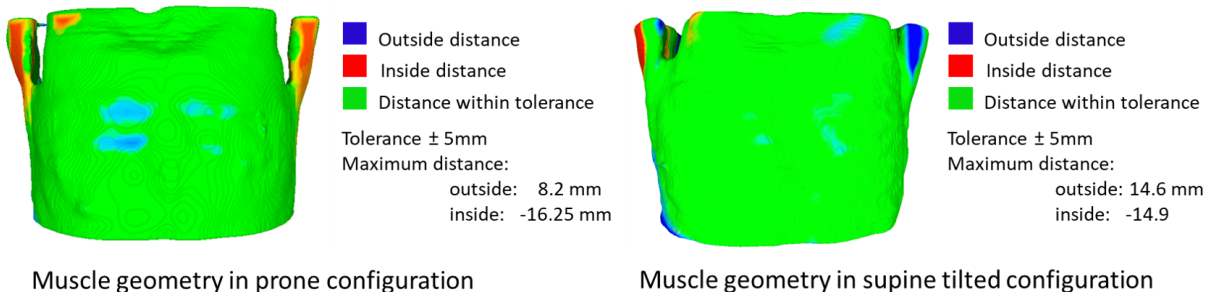


Figure 3.4: Registration accuracy measured over the anterior muscle surface.

As described it will be described next sections, the breast model calibration and evaluation is a time consuming procedure. Therefore, we were able to perform the breast model calibration and evaluation based on the geometry and mechanical properties of the first subject only. Therefore, the image registration of the second volunteer was not performed.

In a multi-loading gravity finite element simulation, the gravity force is applied to the whole model as a body force. The gravity force orientation can be broken down into three components of the Cartesian coordinate system labeled as X, Y, and Z directions (Figure 3.5). The supine configuration was chosen as a reference state, therefore the gravity loading direction was set in that configuration to be oriented on the inverse direction of the Y axis

(postero-anterior direction, Figure 3.5):  $\gamma_s = (0, -1, 0)$ . The gravity loading direction for the two other positions are given by the rigid transformation computed by image registration:  $\gamma_p = (0.037, 0.985, -0.165)$  direction vector for gravity in prone position and  $\gamma_{st} = (-0.744, -0.667, 0.023)$  direction vector for supine tilted position. These direction vectors characterize the breast configurations of the first volunteer only.

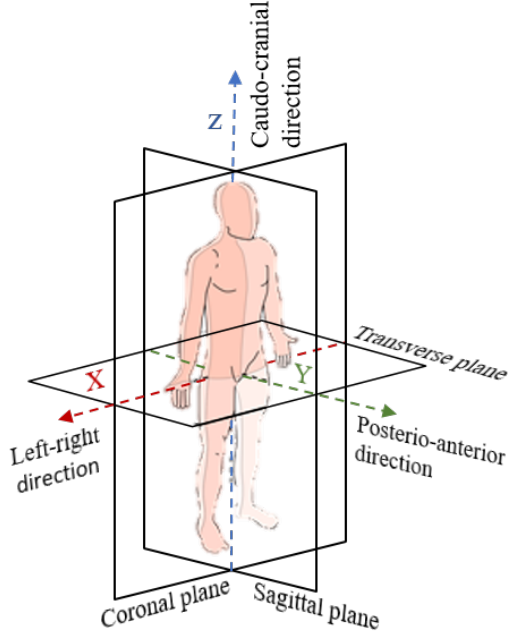


Figure 3.5: Anatomical planes and nominal Cartesian axis directions.

### 3.1.4 Subject-specific 3D geometry

The breast subject-specific geometry was created based on the MR images in supine configuration. Following image segmentation (Figure 3.6.b), the outer shape of labeled regions are subsequently discretized by triangular elements. A semi-automatic Skin Surface module proposed by SpaceClaim Direct Modeler was used to convert the mesh surfaces to non-uniform rational basis spline (NURBS) surfaces (Figure 3.6.c).

The NURBS are averaging curves between points, therefore they are smoother and easier to use in mechanical applications. Figure 3.7 shows the distance from the mesh surface to the NURBS surface for the breast and muscle geometries of the first volunteer in supine position. The NURBS surface fits nearly all over the initial geometry within a tolerance of 0.5 mm. In areas with small curvature angles, the distance between the two surfaces increase up to 1.6 mm and 3.06 mm for breast and muscle geometries respectively.

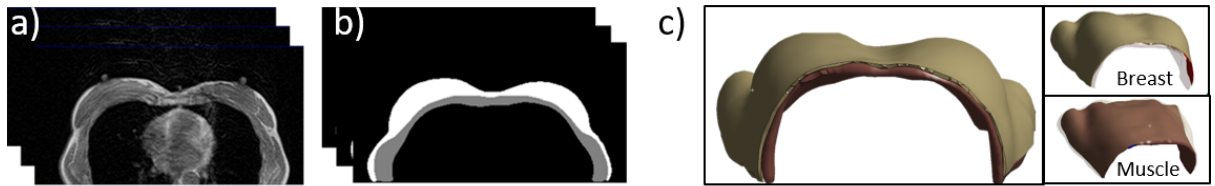


Figure 3.6: 3D geometries generation. a) MR images; b) segmented images; c) corresponding 3D geometries.

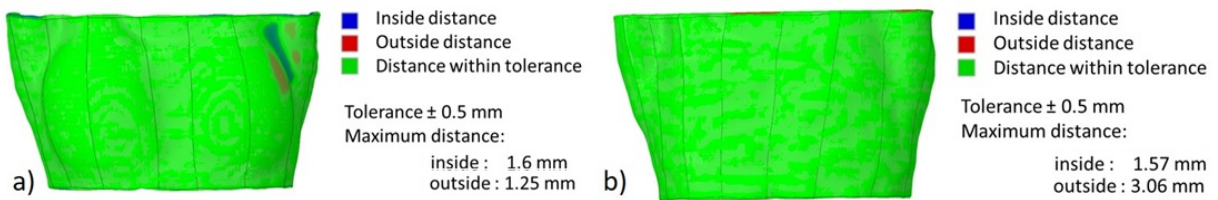


Figure 3.7: The distance between the mesh surface and the corresponding estimated NURBS surface. a) breast volume; b) muscle volume.

## 3.2 Finite Elements Mesh

After computing the NURBS surfaces, the internal spatial information needs to be encoded using a volumetric mesh. The optimal elements type or mesh density for such a simulation is still an open question and topic of debate. The use of hexahedral elements is usually assumed to result in a more accurate solution, especially when expecting high strain/stress gradients. However, in the literature, because of the large computational time, such meshes are used mostly with a reduced number of elements [124, 52]. Tetrahedral elements are widely used due to their geometrical flexibility and because they provide a good trade-off between computation time and estimated displacement accuracy [66, 105, 62].

In our case, an iterative optimization process is being considered to estimate the tissue's constitutive parameters. Therefore, to reduce the computation time, only linear tetrahedral elements were used. The first order elements are known to bear volumetric locking problems when used to model large strain for quasi-incompressible materials [51]. When volumetric locking occurs, the displacements calculated by the finite element method are orders of magnitude smaller than they should be. It has been shown that a linear element with a mixed U-P formulation can avoid these problems [123]. Therefore, in our work, the geometries are meshed using the tetrahedral element solid285 (ANSYS Mechanical) which provides a mixed U-P formulation option.

On the other hand, the mesh density has also an impact on model accuracy. A finer mesh result in a more accurate and stable solution, but also increase the computational time. To our knowledge, no studies have determined the optimal resolution of the volumetric mesh for simulating breast tissues deformations. To determinate the appropriate mesh size, a mesh convergence study was performed. The details can be found in Appendix B.

According to these results the optimal element's size ranges between 7 and 10mm. Thus, the mesh that was chosen for the first volunteer consists in 18453 tetrahedral elements with 9625 elements assigned to the pectoral muscle and the thoracic cage and 8828 elements assigned to breast tissues (Figure 3.8).

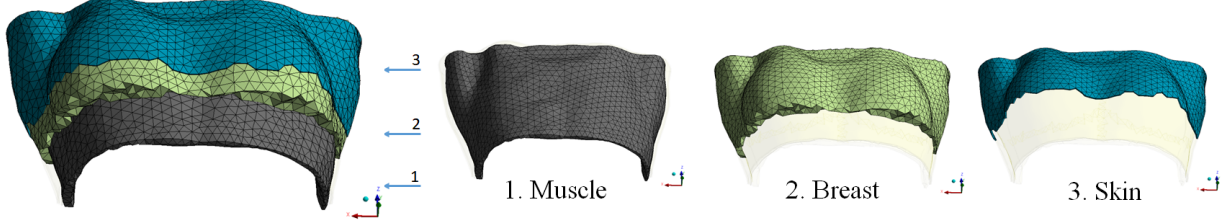


Figure 3.8: Finite element mesh components. The tissues components are cropped for visualization purposes.

The mesh quality was measured using three criteria: element skewness, aspect ratio and maximal corner angle. The Figure 3.9 shows the values ~~ranges~~ distribution for these shape parameters. The element's aspect ratio and maximal corner angle range between the nominal limits defining a good mesh quality (Section 2.2). There is a small number of elements with a skewness ~~larger~~ than the maximal theoretical quality limit ( 0.75 ) , however there are no degenerated elements (skewness = 1).

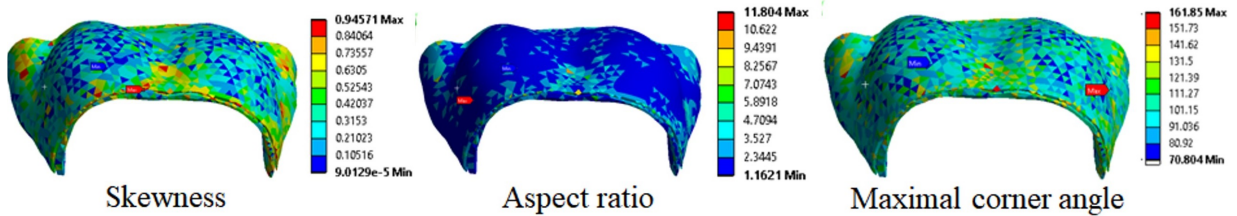


Figure 3.9: Finite elements mesh quality.

The breast skin layer is added a posteriori as a 2mm thick single layer of shell elements (1980 elements). Shell elements and the underlying solid elements are sharing the same nodes (Figure 3.9.a).

### 3.3 Breast reference configuration

To estimate the reference configuration of the breast (*stress-free* configuration), an adapted prediction-correction iterative approach was implemented [43] using prone and supine image data sets. The overall iterative process is presented in Figure 3.10. The first estimate of stress-free breast configuration is computed by applying an inverse gravity on the supine geometry. Then, at each iteration, the estimated stress-free configuration is used to simulate breast deformation due to gravity in a prone position. The differences between

the result of this simulation and the real shape of the breast in prone position is quantified by computing the Euclidian distances  $d_j$  for each *active node* defined at the breast external surface. These distances are then used in the next iteration of the process to simulate imposed displacements (Dirichlet condition) to the active nodes  $j$  in the stress-free configuration. To reduce the mesh deformation, and thus to limit any element distortion, the displacements are only partially imposed using a multiplicative regularization factor ( $\alpha < 1$ ). The process repeats as long as the new transformation improves the similarity between the two geometries in prone configuration by more than 1 mm on average,  $|D_{i+1} - D_i| > 1 \text{ mm}$ . The similarity between the estimated and measured configurations at iteration  $i$  is given by the mean Euclidean distance  $D_i$  over the active nodes  $j$ .

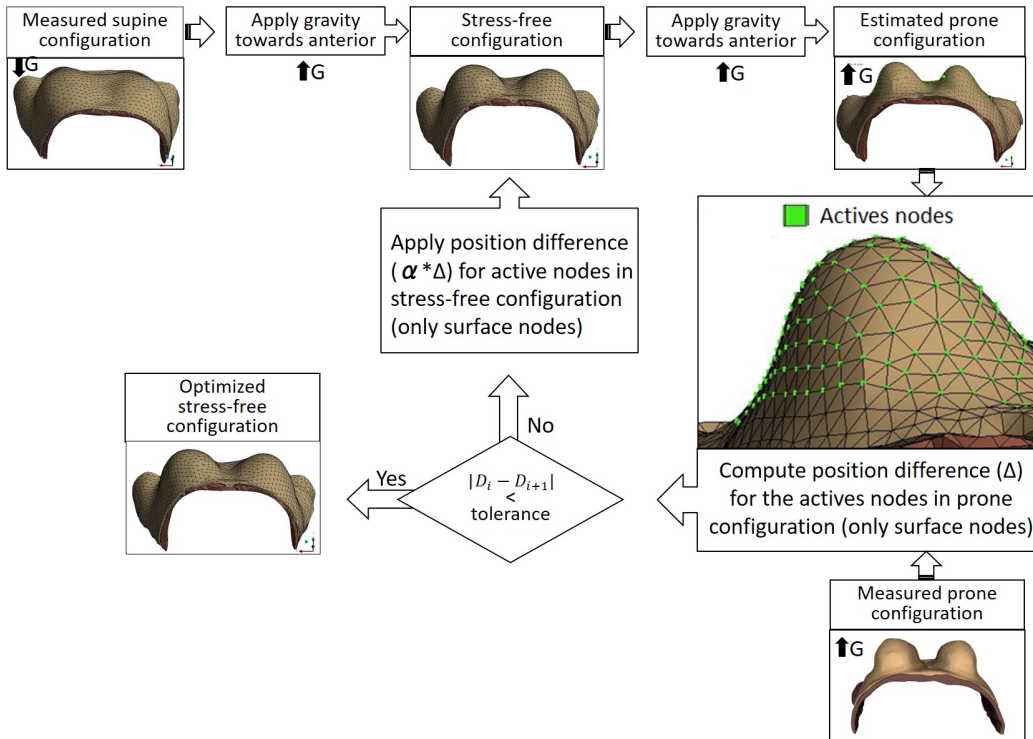


Figure 3.10: Fixed point type iterative algorithm for stress-free geometry approximation.  $D_i$  - mean node to node distance over the active nodes at iteration  $i$ ,  $G$  - gravity force

During the fitting process, the active nodes are chosen to be the ones corresponding *only* to the breast surface. The skin nodes belonging to the arms and the lateral thoracic areas are excluded in order to neglect as much as possible the error due to rigid body changes.

To compute the distance  $d_j$  between the node position in the estimated and the measured breast configurations, the positions of the active surface nodes on prone configuration have to be known. Thus, an additional mesh registration step was performed at each iteration: the active nodes were morphed into prone configuration using the elastic deformation method proposed by Bucki M. [16]. The method estimates a C1-diffeomorphic, non-folding

and one-to-one transformation to register a source point cloud onto a target data set, which can either be a point cloud or a surface mesh. The set of input source points is initially embedded in a deformable virtual hexahedral elastic grid. Then, an iterative registration technique is performed. At each iteration the grid is deformed such that the distance between the target and the source nodes is minimized. The use of the grid allows to speed-up the registration process. The distances between the grid vertices and target nodes are computed only once, prior to registration. The [source points location](#) is then computed by interpolation between the closest grid vertices. To increase the registration accuracy, the regular grid is progressively refined by subdividing each cell into eight smaller ones. Seven refinement steps were performed resulting in a minimal cell size of about 2 mm.

### 3.4 Boundary conditions

To provide a rigid support for the muscle mesh component, zero displacement conditions are imposed to its posterior face, assumed to be attached to the rib cage ([figure 3.11](#)). Then, the interface between the breast mesh and [muscle](#) mesh is modeled using contact mechanics. The muscle is stiffer than the adipose tissues, thus its anterior face represents the target surface and the posterior breast face represents the contact surface (see Section 2.3 for a reminder of these target and source surfaces).

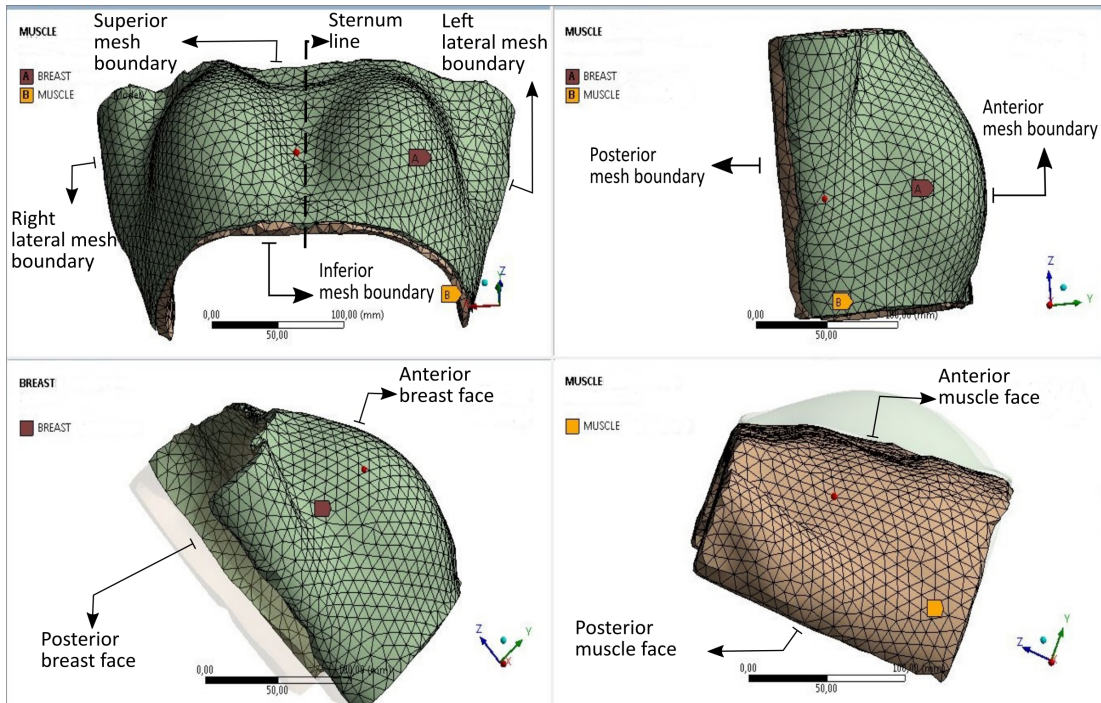


Figure 3.11: Finite elements mesh boundaries

Previous works have shown that modeling breast deformations from prone to supine configurations requires taking into account breast tissues sliding over the chest wall [19, 66].

Therefore, the juncture surface is modeled as a no-separation contact with a frictional behavior proposed by the ANSYS Contact Technologies (see Section 2.3.2). The penalty algorithm is used with a meticulous control of contact normal and opening stiffness parameters. At this stage, stiffness parameters do not have a physical meaning and have to be identified by *trial and error* methods. Since these parameters are extremely sensitive to the stiffness of the underlying elements and to the direction of the local deformation, new values have to be identified for each new simulation case.

To study the impact of the friction coefficient ( $\mu_f$ ) on tissues sliding, several simulations have been performed at different values of  $\mu_f$ . We found that, with the Coulomb friction law, even for a high value of  $\mu_f$ , too much sliding is allowed when estimating the prone breast configuration. At the contact surface, because of excessive sliding, the tissue accumulation in the region of the sternum line results in a sinuous surface (Figure 3.12); thus, the finite element mesh undergoes important distortions and the solution is compromised. Therefore, different strategies based on anatomical breast structures were investigated to limit the amount of sliding and to overcome solution instabilities (Appendix C). However, it seems that a small amount of friction improves the solution convergence capabilities [6]; therefore the friction coefficient was kept to  $\mu_f = 0.1$ .

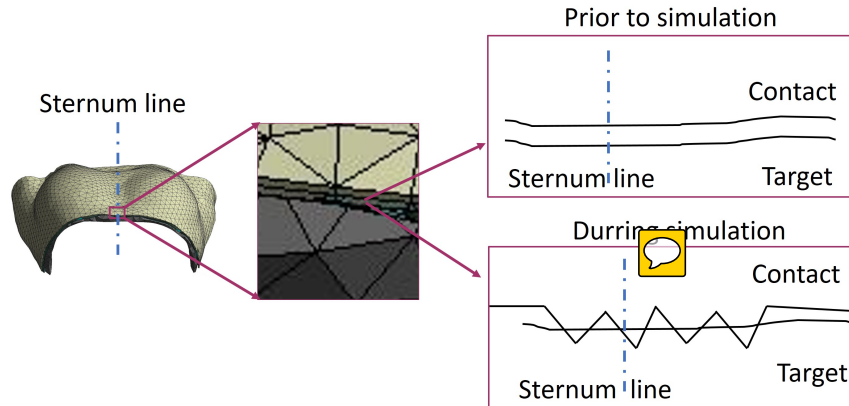


Figure 3.12: Tissues accumulation on the sternum line with excessive sliding

The breast soft tissue is firmly attached to the deep fascia via suspensory ligaments but can move freely over the pectoralis muscle [96, 29]. Therefore, the strategy chosen to control the amount of tissues sliding relies on ligamentous breast structures described in Section 1.1.3. As far as breast support matrix is concerned, only the largest structures were modeled (i.e. fascias and suspensory ligaments). The superficial layer of the superficial fascia was integrated in the skin layer, assuming a higher material stiffness. In addition, a new layer of 0.1mm thick shell elements was added at the juncture surface between muscle and breast tissue to model the deep layer of the superficial fascia. The shell and the underlying breast elements were imposed to share the same nodes. Since the deep fascia and muscle tissues are supposed to present similar elastic properties, the deep fascia was not explicitly modeled. In addition, two ligamentous structures (inframammary ligament

and deep medial ligament) were modeled using [Ansys](#) link type elements connecting the [node](#) of the breast posterior surface to anterior muscle surface (Figure 3.13).

Several additional Dirichlet conditions were set on the mesh boundaries: the superior and inferior ends of the deep fascia layer are constrained in Z direction; the superior and inferior ends of the skin layer are constrained in Y direction. For left and right lateral breast boundaries (Figure 3.11), Dirichlet conditions are too strong and preclude breast tissue to slide laterally. Therefore, in these regions, new ligamentous structures are included using link elements with a cable-like behavior (Figure 3.13).

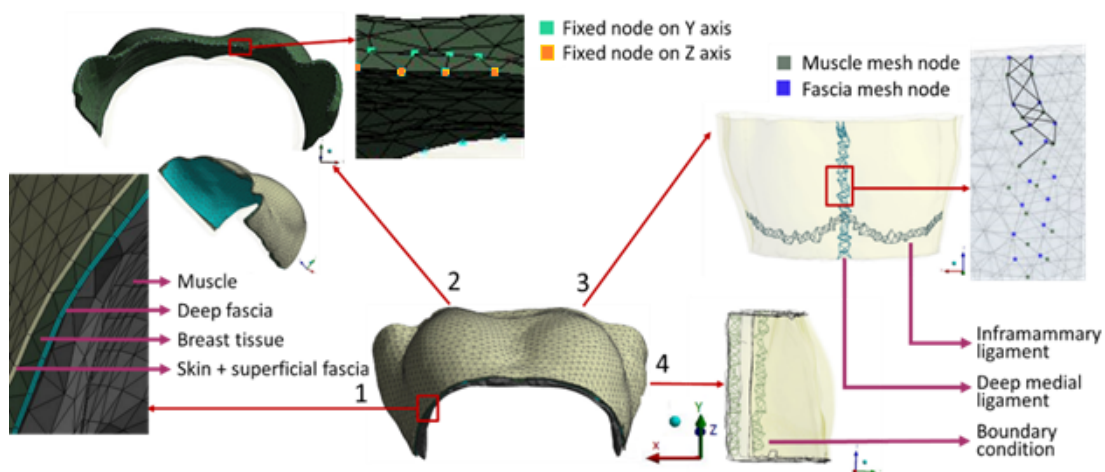


Figure 3.13: Components of the finite element mesh.

The deep layer of the superficial fascia is much stiffer than the underlying adipose tissues. Due to imposed boundary conditions, the amount of sliding depends on fascia's elasticity. The suspensory ligaments define regions where the breast sliding is minimal regardless of the applied deformations. These additional stiff structures reduce the tissues sliding and improve the solution convergence capability.

### 3.5 Material constitutive models

Our final model consists of 6 types of tissues, wherein 4 tissues (glandular, fatty, muscle and skin) are well described and regularly used in biomechanical modeling, and 2 of them (fascia and suspension ligaments) are with limited use and poorly described in the literature. A large range of values of the constitutive parameters are available for each tissue. However because of an [inconsistent](#) interindividual variability, subject-specific parameters had to be identified.

Here, all materials [except to](#) the suspensory ligaments were modeled using the Neo-Hookean strain energy functions. Breast suspensory ligaments were assumed to undergo only small deformations, thus they were considered as linear materials. Subject-specific mechanical tissue properties were computed using an optimization process based on a

multi-loading gravity simulation procedure (Figure 3.14). First, for a given set of parameters ( $\lambda_{glandular}$ ,  $\lambda_{adipose}$ ,  $\lambda_{muscle}$ ,  $\lambda_{skin}$ ,  $\lambda_{fascia}$ ,  $\lambda_{ligam}$ ,  $\nu$ ), the stress-free configuration was estimated by minimizing the difference between the simulated and the measured breast geometry in prone configuration. Then, from the new estimated stress-free geometry, the supine breast configuration was derived. The estimated supine geometry was compared to the measured one using modified Hausdorff distance (see Appendix A for distance definition), representing the estimation error. To avoid including the geometry dissimilarity due to arm position, the modified Hausdorff distance was computed only on breast skin surface. The process implies multiple simulations based on imposed node displacements; therefore the FE mesh can be significantly altered (with convergence issues) before reaching an optimal stress-free geometry. Mainly for that reason, we chose to perform an exhaustive manual research (rather than an automatic one) of the optimal set of constitutive parameters.

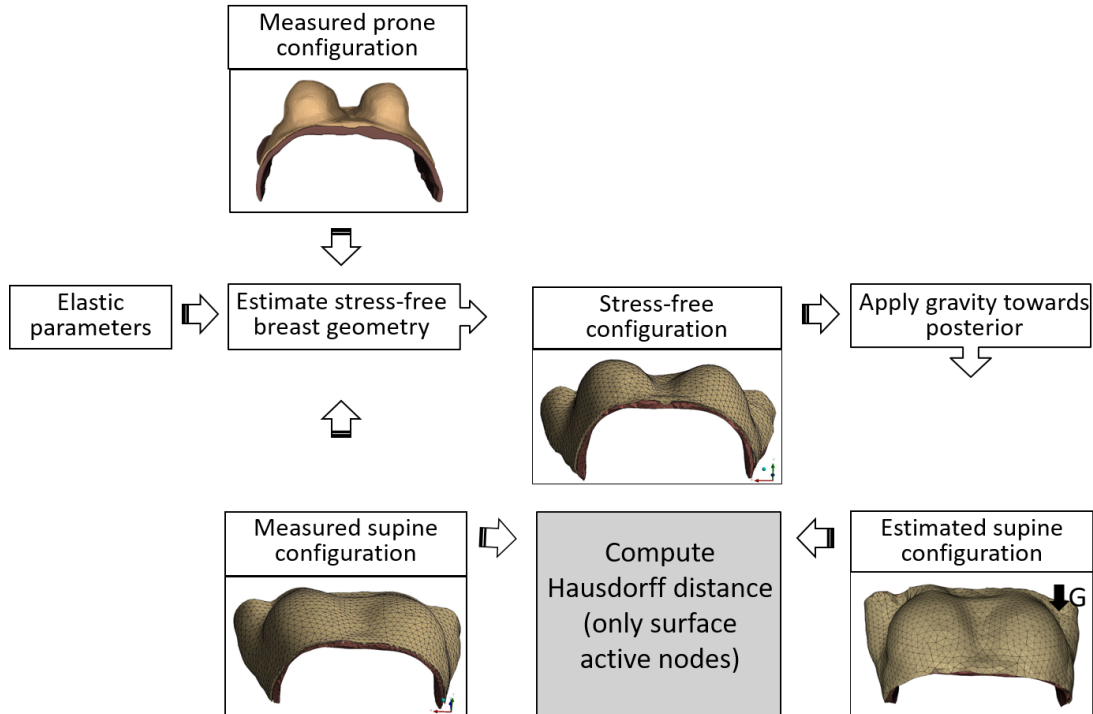


Figure 3.14: Process to estimate optimal material parameters

An optimization process including finite element simulations with 6 parameters results is a complex and time-consuming problem. The model simplification was then performed in two steps. First, the parameters which variations have limited effects on simulation results were identified and set to an optimal fixed value. Next, for parameters which variations have a high impact on simulation results, a sensitivity study was performed to redefine the search intervals and interval's discretization step.

### 3.5.1 Model simplification

The breast tissues are mainly composed of water; a usual assumption is to consider them as nearly incompressible materials[50]. However, previous works proposed a Poisson's ratio value ranging between  $\nu = 0.3$  [73] and  $\nu = 0.5$  [52]. In a multi-loading gravity simulation, the breast volume is nearly constant, thus, the influence of Poisson's ratio on nodes displacements was studied only for values ranging between  $\nu = [0.45, 0.495]$  (Figure 3.15).

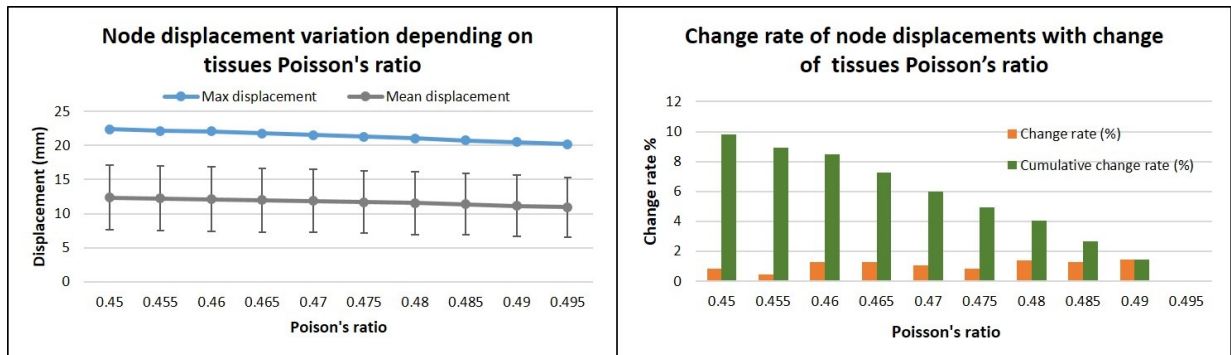


Figure 3.15: Estimation of the optimal material parameters

The simulations were performed by applying the gravity force in posterio-anterior direction on breast geometry in supine configuration. We present on Figure 3.15, the node displacement variation and the change rate of node displacement as function of the tissue Poisson ratio. On the left-hand side, the mean and the maximal displacements of the skin nodes are given for each values of  $\nu$ . On the right-hand side, the maximal difference of nodal displacements between two consecutive simulations (change rate) and the maximal difference of node displacements between the actual and the less deformed geometry (cumulative change rate) are plotted. The change rate is computed within the assumption that the maximal displacement over the simulations set represents 100 % change rate. Non-significant variations are observed on the mean and maximal displacements of skin nodes, thus a constant value of  $\nu = 0.49$  was chosen.

The pectoral muscle together with the thoracic cage are the breast tissues support. The deformation of the muscle under gravity loading is neglected. Therefore, its Young's modulus was not included on the parametric study and was chosen so that only minimal deformations occur ( $\lambda_{muscle} = 10kPa$ ).

The ligamentous breast structures are added with a cable-like behavior to reduce tissues sliding. Their Young's modulus is also not included in the optimization process and is set sufficiently high ( $\lambda_{ligam} = 500kPa$ ) to preclude their elastic deformation.

The adipose and glandular tissues are known to be extremely soft and to undergo large deformations under gravity loading. Calvo-Gallego J.L. [17] proposed a uniform polynomial material model for the mixture of adipose and glandular tissues. The authors have also shown that the breast outer shape deformation does not depend on glandular distribution but is highly dependent on its volumetric ratio. In this work, it was chosen to model the

glandular and fatty tissues as a single homogeneous material with an equivalent Young's modulus  $\lambda_{breast}$ . The mechanical properties of the equivalent breast tissue are in direct relation with glandular and adipose volumes ratios. Because the left and right breasts may have different glandularities, two different parameters are considered ( $\lambda_{breast}^l$ ,  $\lambda_{breast}^r$ ), one for each laterality.

Breast skin and superficial fascia are an essential part of the breast support matrix. The two layers are much stiffer than breast tissues and are the structures governing the amount of deformations. Their elastic behavior was included on the optimization process.

Based on existing publications, an interval of possible values are given in Table 3.2 for each parameter included in the optimization process ( $\lambda_{breast}^l$ ,  $\lambda_{breast}^r$ ,  $\lambda_{skin}$ ,  $\lambda_{fascia}$ ). To characterize model sensitivity to parameters' variations, a set of simulations were performed. The defined intervals for each type of tissues were discretized by steps of 10% and at each step the skin nodes displacement were computed. Results of the corresponding simulations are shown on Figure 3.16. As previously, the first column represents the variation of mean and maximal displacements of skin nodes in function of the elastic parameter of each material; the second column represents the change rate and the cumulative change rate of skin nodes displacements.

	Search intervals from bibliographic data			Search intervals after model simplification		
	Breast	Skin	Fascia	Breast	Skin	Fascia
Min (kPa)	0.3	7.4	100	0.3	2	50
Max (kPa)	6	58.4	5000	4	20	250

Table 3.2: Minimal and maximal value (in kPa) for Young's moduli.

The figure shows that the model is very sensitive to the variation of Young's modulus of breast tissue, skin and fascia (Figure 3.16). However, beyond some values, the materials become too stiff and do not change significantly the breast deformations under gravity loadings. Therefore, the search intervals for breast tissue and skin Young's moduli were reduced so that a larger value impacts the cumulative change rate less than 20% (max displacement less than  $\sim 5mm$ ). As the fascia stiffness governs the lateral displacement and shows a smaller variation over the search interval, a threshold of 10 % ( $\sim 2.5mm$ ) was chosen. The obtained search intervals are summarized in Table 3.2

### 3.5.2 Estimation of the optimal constitutive parameters

The model optimization is a tough and time consuming process. It was extremely difficult to obtain the solution convergence when combining the tissues large deformations with the sliding contact conditions. Because of the large computation time, the reference breast configuration and the optimal constitutive parameters were computed only for the first volunteer. The model optimization of the second volunteer is considered for future work.

**CHAPTER 3. A NEW BIOMECHANICAL BREAST MODEL EVALUATED ON REAL DATA**

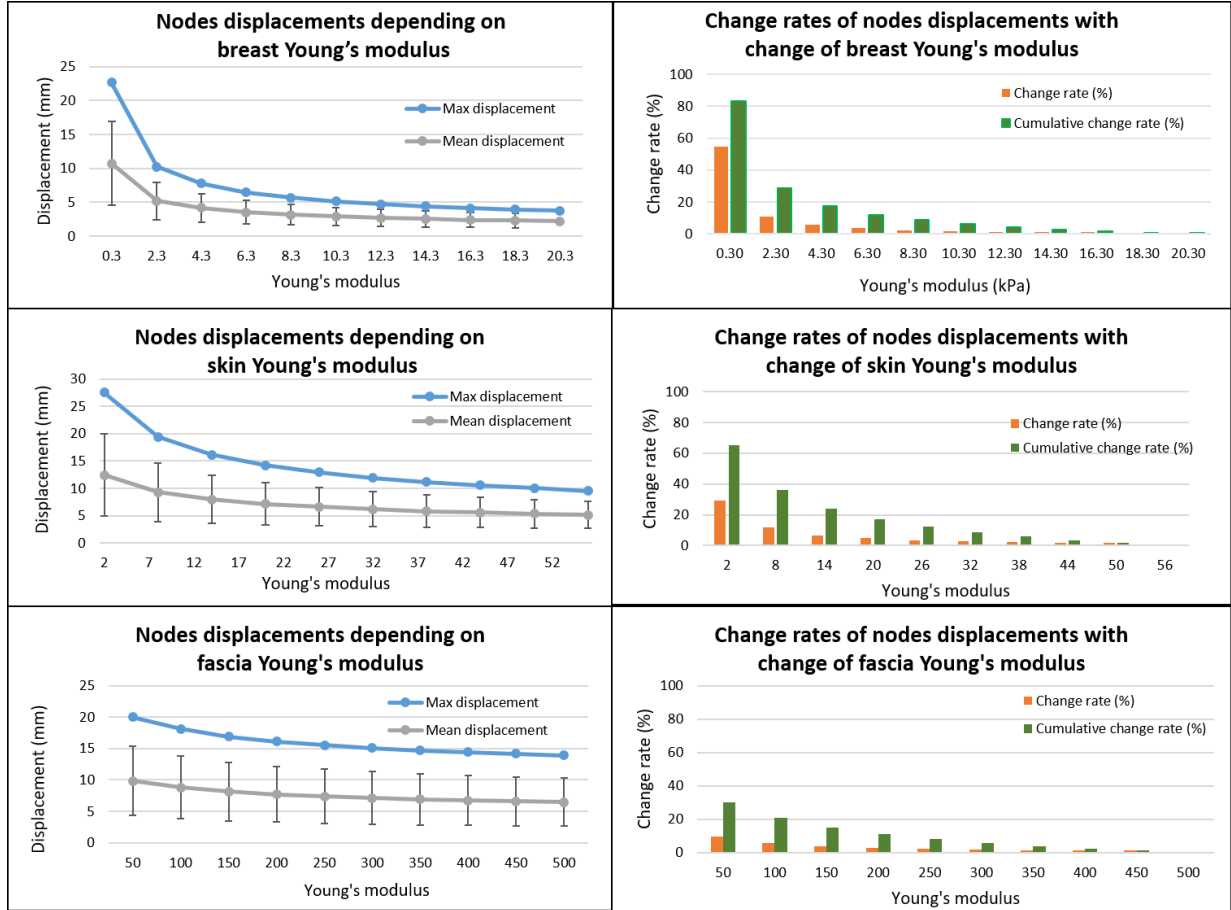


Figure 3.16: First column: relation between maximal and mean nodes displacement and the equivalent Young's moduli variation for different tissues. Second column: rate and cumulative change rate of skin node displacement as function of quivalent Young's modulus

To estimate the constitutive parameters describing the breast mechanics of the first volunteer, the new intervals defined by the above sensitivity analysis were discretized by steps of  $0.1\text{ kPa}$ ,  $1\text{ kPa}$  and  $40\text{ kPa}$  for breast, skin and fascia tissues respectively. The discretization step was chosen such that the change rate between two consecutive simulations is less than 10%. The previously described multi-loading gravity process was performed for each set of parameters and the corresponding model error distribution is shown in Figure 3.17. The contour lines are estimated by linear interpolation between two consecutive simulations.

It was found that the value of the Young's modulus of the breast tissues is lower than the ones reported in the bibliography. Therefore more simulations were done outside the defined intervals. However, for very low values, below  $0.2\text{ kPa}$ ,  $2\text{ kPa}$  and  $80\text{ kPa}$  for breast, skin and fascia's Young's modulus respectively, the tissues deformation is too large and the finite element mesh becomes degenerated at the first step of the multi-loading simulation. For values above  $1\text{ kPa}$ ,  $5\text{ kPa}$  and  $160\text{ kPa}$ , tissues deformation is too small

# CHAPTER 3. A NEW BIOMECHANICAL BREAST MODEL EVALUATED ON REAL DATA

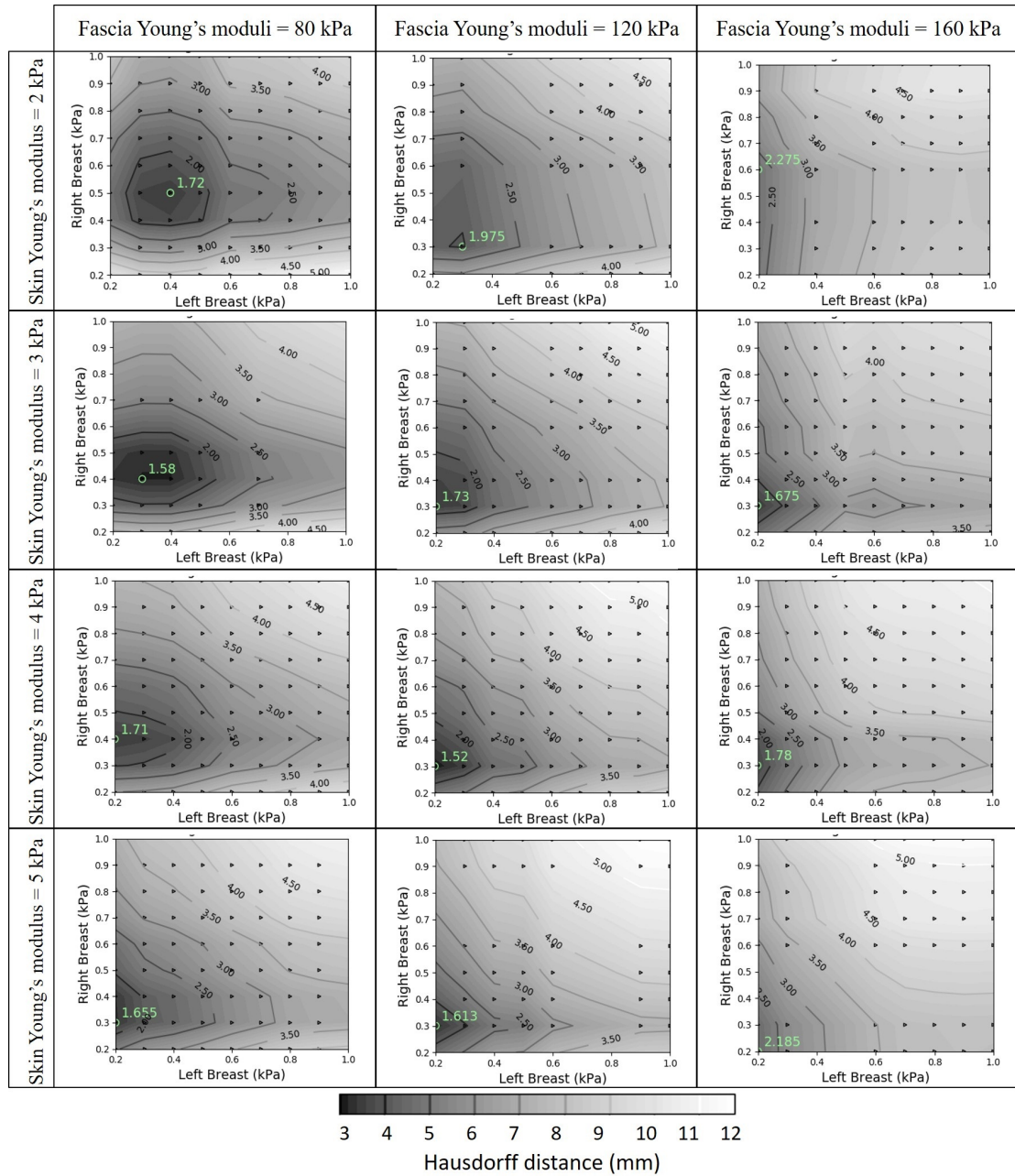


Figure 3.17: Hausdorff distance on the skin surface over the constitutive parameters space

compared to the ones observed from the MR images and the simulations using such values were excluded. All other missing values correspond to failed simulations due to a non-converging force, specifically in the region of the contact surface between the breast and the muscle.

For soft fascia ( $\lambda_{fascia} = 80\text{kPa}$ ), the lateral displacement of breast tissues is more important than the one measured on MR images. Contrariwise, for stiff fascia mater-

## CHAPTER 3. A NEW BIOMECHANICAL BREAST MODEL EVALUATED ON REAL DATA

ial ( $\lambda_{fascia} = 160\text{kPa}$ ) the amount of sliding is too small. To match the breast geometry in supine configuration, very low values of breast Young's modulus are required ( $\lambda_{breast} < 0.2\text{kPa}$ ). For such low values, the breast tissues are highly deformed, thus the finite elements undergo large distortions. Due to such errors in element formulation, the simulations giving the minimal Hausdorff distance did not succeed.

The set of parameters providing the best match between simulated and measured supine breast configurations is ( $\lambda_{breast}^r = 0.3\text{kPa}$ ,  $\lambda_{breast}^l = 0.2\text{kPa}$ ,  $\lambda_{skin} = 4\text{kPa}$ ,  $\lambda_{fascia} = 120\text{kPa}$ ).

Figure 3.17 shows the differences between the measured and estimated breast geometries in prone (left) and supine (right) configurations. Each distance was computed over the skin active nodes used also for the model optimization.

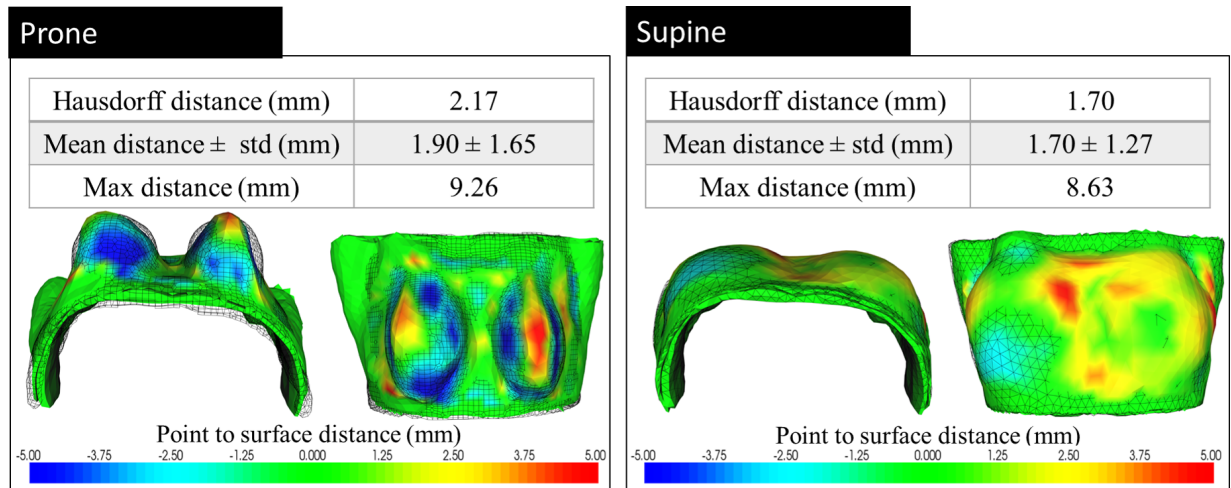


Figure 3.18: Difference between estimated and measured data, in prone and supine configurations, obtained with optimal Young's moduli and stress-free geometry.

The breast geometry is better estimated in supine configuration, with an Hausdorff distance equal to 1.72 mm. This is probably due to a better representation of the boundary conditions in supine configuration, as this configuration was used to create the initial finite element mesh. The breast geometry in prone configuration is also well estimated, with a modified Hausdorff distance equal to 2.17 mm. The maximal node to surface distance is obtained on the breast lateral parts. Considering non uniform skin thickness or elastic properties over the breast surface, as described by Sutradhar A. and Miller M.J. [134], should improve the obtained results in prone configuration.

## 3.6 Model validation

MRI-based biomechanical models already published in the literature have used the same breast configurations for the optimization and the evaluation process. In such a case, the model accuracy is assessed for a single deformation configuration, namely the one used

during the optimization process. Therefore small estimation errors are expected. However, there is a high probability that the same model will fail in computing the global breast deformations within different conditions, for example a different gravity orientation or in presence of breast compression.

Our breast model was developed to model soft tissues deformation under compression. Therefore the model error must be assessed in a more general framework. The supine tilted breast configuration was not used during the optimization process. Then, the difference between the estimated and measured data in this position was computed to evaluate the capabilities of our model.

To compute the breast deformation under gravity loading on supine tilted configuration, the reference geometry together with previously defined [materials](#) models were used. The body force direction was defined according to the vector obtained by image registration (section 3.1.3). The model accuracy, in reference with the real deformations, was assessed using 4 measures of distance based on the spatial location of the skin nodes (Appendix A). As previously described only the subset of active nodes was considered for distance computation. Figure 3.19 shows the magnitude of the node to surface distance, mean and maximal node to surface distance, and modified Hausdorff distance.

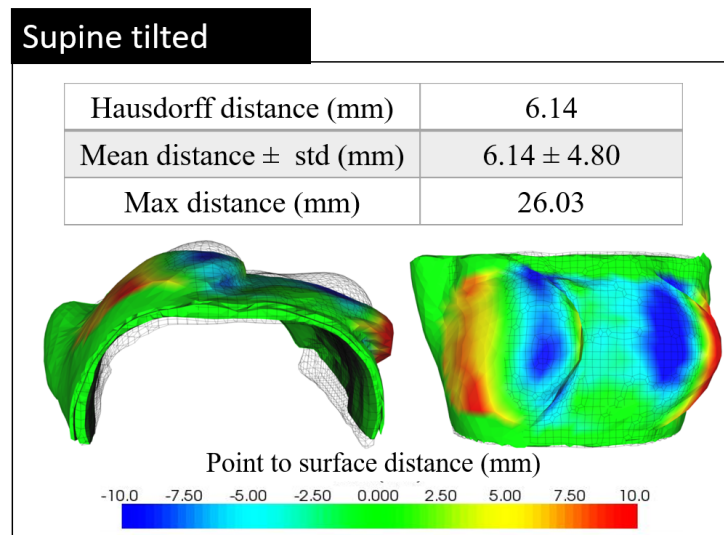


Figure 3.19: Difference between estimated and measured breast geometries in supine tilted configuration.

One may see that the supine tilted breast configuration is unwell described by the breast biomechanical model (Hausdorff distance equal to 6.14 mm). Large difference between simulated and measured breast surfaces is caused by the excessive sliding of breast tissues over the chest wall. Numerical or structural modeling choices could explain such a behavior.

Firstly, such discrepancies between the measured breast geometry in supine tilted configuration and its estimate could be caused by an accurate registration between the supine and supine tilted configurations. Moreover, one may observe on MRI images that, during

the volunteer's position change, the pectoral muscle undergo elastic deformation. Therefore ~~its~~ also involves changes of model boundary conditions that was not considered during simulations.

Secondly, the fascial and ligamentous tissues are usually characterized by a cable-like behavior. The strain-energy density function must behave asymptotically in order to limit the fascia stretch and thus reduce non-linearly the breast sliding over the chest wall. Limitations of the neo-Hookean model to capture the mechanical response of some nonlinear materials is well known [77]. For large strain rates, the Neo-Hookean material may undergo a relaxation and therefore becomes easier to deform. Our numerical results have shown that the maximal strain at the fascia level is significantly higher in supine tilted position (about 140%) than in supine or prone positions (about 50%). Therefore, an asymptotic behavior of fascia mechanical response must be considered. The Gent form of the strain-energy function characterizes better such mechanical response [58] and ~~will be considered~~ as an alternative choice .

And finally, the breast support matrix is composed of 4 suspensory ligaments. However only two of them were partially modeled: inframammary and deep medial. The 3D structures connecting the skin to some muscular areas, namely the cranial ligament, were neglected. The particularity of the cranial ligament consists in its position. Indeed, almost its entire structure is attached to the skin and the only attachments to the thorax are situated at the clavicle and at the seventh rib levels (inframammary ligament). However, including such structures at the skin surface may result in local high strain gradient rates causing solution instability and anesthetic surface deformations.

### 3.7 Discussions and conclusion

In this chapter, a new finite element breast model was proposed and evaluated with real tissues deformations measured on MR images. To this end, MR images of two volunteers were acquired in three different configurations: supine, prone and supine tilted. The supine and prone MRI volumes were used to adapt the biomechanical model to the volunteer individual breast geometry and its respective tissues mechanical properties. The optimal mechanical properties were ~~found~~ by exhaustive search over ~~a~~ predefined ~~parameters~~ intervals. For each combination of tissues elastic properties, the breast reference configuration was computed using an adapted prediction-correction iterative scheme. The ~~parameters~~ set giving the best fit between estimated and measured breast configurations was selected. Using these optimal estimates, the supine, prone and supine tilted breast configurations were computed and compared to the MRI volumes.

It was found that, extremely soft materials laws (0.2-0.3kPa for breast tissues and 4kPa for skin) must be used in order to obtain the same tissues displacement rate ~~as~~-observed on MR images. Moreover, the breast tissues sliding must be considered when computing such large deformations. However, because of tissues hyper-elasticity, the model boundary conditions have to be revisited in order to ensure the convergence capability of the solution. With such soft tissue, the finite element mesh may become highly distorted. Therefore

## CHAPTER 3. A NEW BIOMECHANICAL BREAST MODEL EVALUATED ON REAL DATA

---

to limit element distortion, a stiffer layer was added between the breast tissues and the pectoral muscle, representing the deep layer of the superficial fascia. ~~The excessive~~ sliding was prevented by using ligamentous structures fixing the soft tissue to the pectoral muscle.

Contrary to the previous ~~works~~, our model was evaluated in 3 breast configurations. Among the 3 geometries, two of them were used for the model optimization and evaluation, and the last one (supine tilted geometry) was used for the evaluation only. Good estimates were obtained in prone and supine configurations with a Hausdorff distance equal to  $2.17\text{mm}$  and  $1.72\text{mm}$  respectively. In supine tilted breast configuration, the breast tissues displace to far laterally. The main factors that could contribute to such differences between the measured and estimated breast geometries are errors in alignment between the supine and supine tilted breast configurations, ~~imprecise~~ boundary conditions or inappropriate constitutive material models.

Assuming that our model describes well enough the mechanical behavior of the breast, we may use it to compute breast tissues deformation when breast is under compression. In that case, ~~internal~~ tissues strains and pressure distribution over the skin surface can be used to quantify the patient comfort during a mammography exam.



# 4

## BREAST COMPRESSION *State of the art*

Mammography is the sole breast cancer screening method recognized by the European Commission for women aged 50-69 years. This method enables examination of the breast in its entirety and offers a high sensitivity for early-stage tumors. However, the mammographic exam is known to be unpleasant for the patient, the main source of discomfort being related to breast compression. For such a standardized and wide-used procedure, good exam conditions and patient comfort should be ensured. Therefore, a study on the relevance of breast compression in mammography is of a potential interest.

This chapter describes the standard mammographic procedure, including the breast positioning methods and the design of the most used paddles. The need of compression is explained in terms of image quality and average glandular dose. Patient comfort and the respective current gold standards are introduced. Finally, the interest of developing a simulation environment to assess the quality of breast compression is explained.

## 4.1 Mammography positioning

During the mammography exam, a qualified radiology technologist positions the breast of the patient between the stationary image receptor and a movable paddle. A routine screening mammography exam consists of two views per breast: cranio-caudal (CC) and mediolateral oblique (MLO) projections.

In a regular workflow, the breast compression is performed in the ~~up-right~~ body position. In the CC view (Figure 4.1-left) the breast is placed on the image receptor, that is initially positioned at the inframammary fold level ~~or a few centimeters higher depending on breast mobility~~. Then, the technologist lowers the compression paddle using a foot switch while gently pulling and positioning the breast onto the image receptor to maximize the amount of projected tissues in the image. In the MLO view (Figure 4.1-right), the image receptor is rotated to an angle between ~~40 to 55 deg~~. The lateral oblique side of the breast is positioned against the image receptor. In this view, the pectoral muscle is located between the detector and the compression paddle; as the muscle is stiffer than the breast tissue, the woman has to stay relaxed in order to get a better breast flattening. When lowering the compression paddle, the technologist has to pull the breast upward and forward to prevent breast drooping, and to smooth out any skin folds.

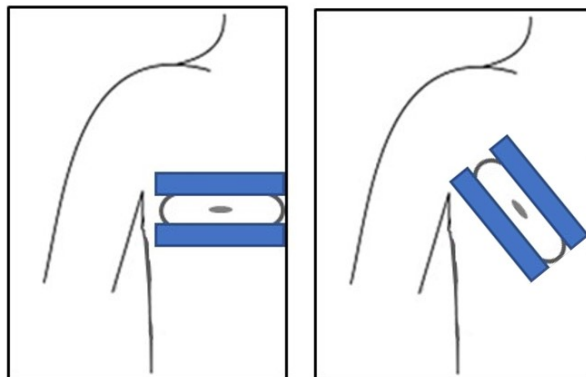


Figure 4.1: left: cranio-caudal breast compression; right: mediolateral oblique breast compression.

The two views are complementary. The MLO view covers a large amount of tissue and provides a better visualization of the upper juxtathoracic part of the breast, while the CC-view suffers less from overlapping dense tissue and provides a better visualization on the central part of the breast [23, 82]. Further incidences or magnification views may be needed for diagnostic mammography [63].

The mammography devices are equipped with paddle position and force sensors to measure and display the compressed breast thickness and the amount of force applied to the breast.

## 4.2 Paddles designs

Nowadays, a wide range of compression paddles are available for breast clinical examination. Their shape and dimensions vary in function of the purpose for which they were designed but also from manufacturer to manufacturer. According to their specific indications of use, three categories can be distinguished: **standard paddle** used for regular screening, **spot paddles** used for diagnosis purposes, and **biopsy paddles** used for breast compression during breast biopsy (Figure 4.2).

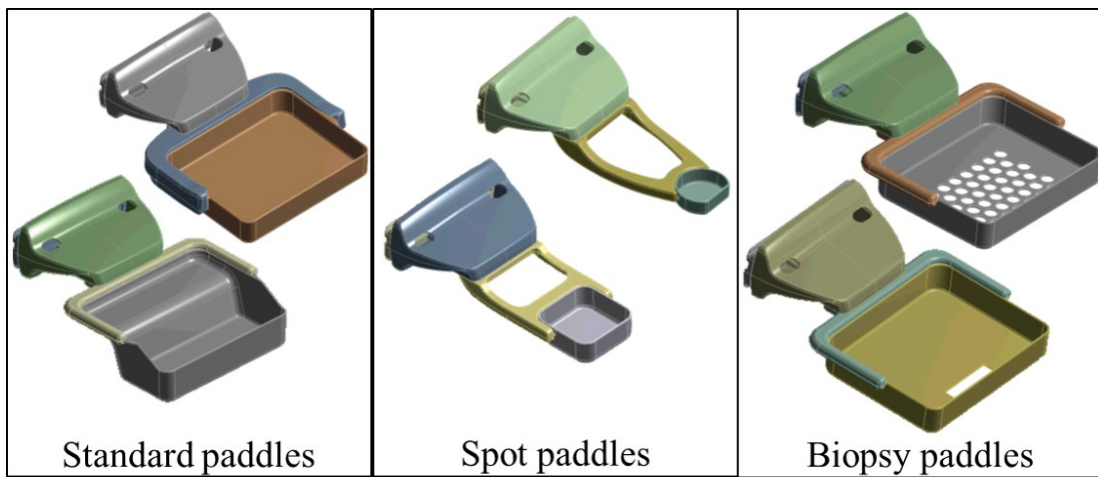


Figure 4.2: Different breast compression paddles for GE Healthcare mammography units .

The standard compression paddles have usually a rectangular shape with a flat compression plate. Depending on the industrial manufacturer, they can have different sizes for both the lateral and longitudinal edges and for the paddle front edge height. Paddles with smaller compression area are used to compress small breasts or breasts with implants (Figure 4.2, Standard paddles). Standard paddles are classified into rigid and flexible paddles. The standard rigid paddle (SRP) is fixed to its frame and is constrained to move in the up-down direction only. This paddle has some flexibility because of its material mechanical properties and can slightly bend when compressing the breast, while remaining globally parallel to the image receptor (Figure 4.3.b). On the other hand, the standard flex paddle (SFP) is attached to its frame by flexible joints and therefore, presents an additional degree of freedom enabling the paddle to tilt with respect to the image receptor plane (Figure 3.e). During compression the paddle remains parallel to the detector at first, tilts towards nipple side and then ends with the highest point at the thorax level. Depending on the breast position, the paddle may also slightly tilt in the medio-lateral direction.

Spot paddles apply the compression to a smaller area of tissue using a small compression plate or a cone. By applying compression to only a specific area of the breast, the effective pressure is increased on that spot. This results in a better tissue separation and allows for a better visualization of the small area in question. It is used to distinguish between the

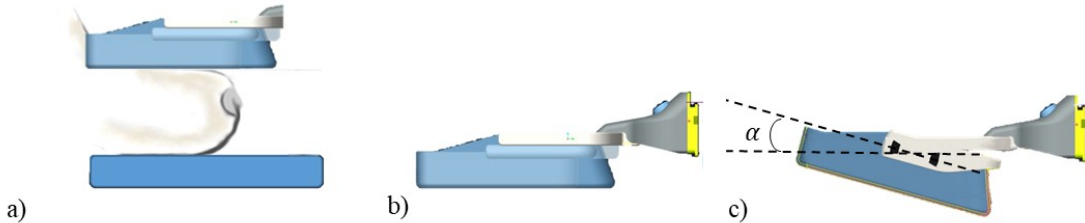


Figure 4.3: a) Breast compression between the paddle (up) and the image receptor (down); b) Rigid paddle; c) Flex paddle with a flexion angle  $\alpha$

presence of a true lesion and an overlap of tissues, as well as to better show the borders of an abnormality or questionable area or a little cluster of faint microcalcifications.

Biopsy exams require that the patient's breast remain immobile and compressed during the entire procedure. The biopsy paddles have basically the same shape as the standard rigid paddles. However, to allow the needle insertion and the accessibility to the biopsied area, the paddle plate contains multiple holes with various diameter or a single aperture.

In this chapter, only breast compression with the rigid paddle in the two main view (MLO and CC) is considered.

### 4.3 Compression mechanics

Nowadays, the European Commission recommends a force standardized breast compression, i.e. a compression that stops at a level of force just below the subject's pain threshold or at the maximum force setting of the machine. The compression guidelines state that force should be firm but tolerable with a maximum applied compression of 130-200 N [111]. As there is no exact specification for the application of breast compression, the applied force may vary between technologists and radiologists. Mercer C. and colleagues [94] have analyzed the variation of the applied force within 14 trained practitioners. Both views, CC and MLO, were included. The authors found a significant difference between the average applied forces and have highlighted three groups of radiologists depending on the mean force intensity. Between the consecutive groups, a mean difference of 16 N was found.

The global breast compression cycle is characterized by two phases: flattening and clamping [33]. During the flattening phase, the breast is gradually deformed by increasing the compression force; this step lasts about  $7.5 \pm 2.6$  s. By contrast, during the clamping phase, which lasts approximately  $12.8 \pm 3.6$  s, the compression paddle is immobilized holding the breast in a stationary position.

Figure 4.4 shows a typical compression cycle for a CC breast compression from experimental data on real patients described by Groot J.E. et al. [33]. One can see that, during compression phase, the breast thickness and contact area evolve non-linearly; meanwhile, the compression force and pressure increase quasi-linearly. During the clamping phase, the breast thickness remains constant; however, the skin pressure and the compression force

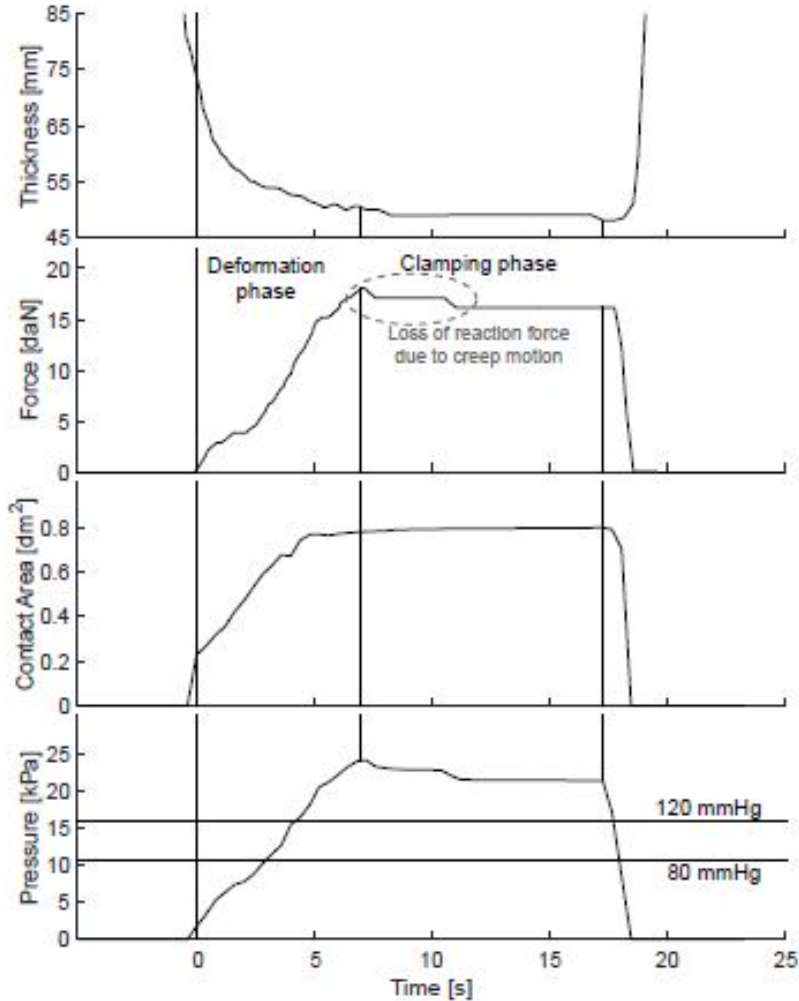


Figure 4.4: A typical breast compression cycle. Reproduced from Groot J.E. et al. [63]

slightly decreases in the first 10s. This phenomenon may be explained by breast volume changes because of the viscous effusion of blood and lymph into the central systems.

In the same work, the authors present several in-vivo measured patterns describing the relation between breast thickness and compression force depending on breast size and its firmness (Figure 4.5). One can see that, for a larger breast, higher compression force is needed but the overall behavior remains the same as for smaller breasts. For similar breast sizes, the final compression forces range within the same values, however a firmer breast will reach faster the limiting value of breast thickness resulting in an asymptotic increase of the compression force.

Dustler M. and colleagues [38] have studied the pressure distribution patterns for MLO breast compression (55 degree tilt). The authors showed that the pressure distribution varies widely within the breast. The obtained patterns from 131 subjects were classified into four main groups: a) skin pressure widespread over the breast (29%); b) skin pressure

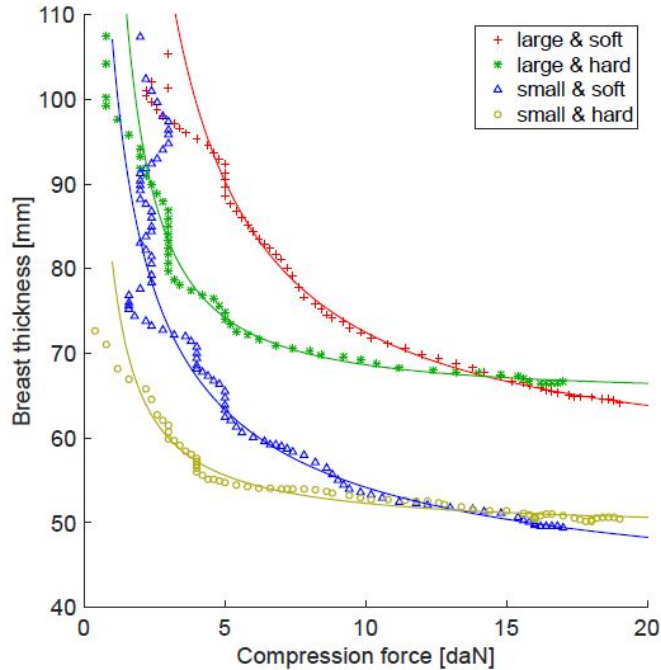


Figure 4.5: In-vivo measured breast flattening curves as function of the applied force. Reproduced from Groot J.E. et al. [63]

concentrated on the central part of the breast (8%); c) skin pressure concentrated on the juxtathoracic region (16%); d) skin pressure concentrated along a narrow zone at the juxtathoracic region (26%). According to their results, the pressure distribution depends on two factors: the variation ~~on~~ breast thickness ~~from one side and~~ surrounding tissues stiffness ~~from the other side~~. For example, for the groups c and d ~~the~~ breast anterior tissues ~~compression~~ is limited by the pectoral muscle which is much stiffer than the breast tissues. These results may explain the fact that, in MLO view, the breast thickness exceeds the one ~~on~~ the CC view, despite the larger force used in MLO ~~than in~~ CC breast compression [94, 68].

## 4.4 Compression quality metrics

A standard mammography protocol always includes breast compression prior to image acquisition. ~~The breast~~ flattening improves ~~diagnostic~~ image quality and reduces the absorbed dose of ionizing photons. However, ~~the~~ discomfort and pain produced by this procedure sometimes might deter women from attending breast screening by mammography.

An important improvement concerning the patient comfort could be achieved with the emergence of digital mammography. Indeed, several studies have shown that digital mammography is better in terms of image quality [100] and radiation dose [24] than film-

screen mammography.

Most digital mammography systems have an automatic beam quality selection mode (automatic optimization of parameters, AOP) with an automatic exposure control (AEC). The AOP mode automatically selects the X-ray tube voltage, the anode target material and filter material defining the X-ray spectrum, in order to optimize the *contrast to dose ratio*, i.e. the appropriate amount of radiation for an acceptable low dose and an increased contrast, according to breast thickness and composition [145]. Then, the required exposure time for the actual image is calculated by the AEC. The AOP control allows to determine, for each patient and compression level, the X-ray spectrum that optimizes the ratio of benefits (higher image contrast) and drawbacks (higher dose). In this section, the compression quality will be measured in terms of three metrics: image quality, average dose and patient comfort. A detailed description of each metric is given below with their impact for digital mammography.

#### 4.4.1 Image quality

Many factors may influence the quality of the mammography image such as the knowledge and skill of the person who performs the mammography examination, the equipment, the positioning technique, and the compressed breast thickness, type of breast cancer, and radiographic appearance of the breast tissue [33, 4]. In our study, only the impact of the compressed breast thickness on image quality is analyzed.

Firstly, the breast compression facilitates the image interpretation. Higher compression leads to better tissues spread and consequently to less overlapping of clinical important structures. A thinner layer of breast tissues allows a more subtle differentiation between normal and suspicious findings. Secondly, breast compression affects the image sharpness. Since the exposure time lasts several seconds, a proper breast immobilization reduces the image blurring, preserving the conspicuity of abnormal legions. Moreover, with a reduced breast thickness, the primary contrast is raised due to the reduction of radiation scatter to primary ratio at detector level. Finally, the breast compression leads to a better use of the detector dynamic range. With a non-uniform breast thickness, the different levels of brightness are used to describe the thickness variation, thus the detector dynamic is not used optimally for the contrast representation due to different internal structures. This is particular true for screen-film technology, with digital detectors; this constraint can be challenged.

It has been proved that image quality decreases with increasing breast thickness [83, 68, 128, 116]. Helvie M. and colleagues [68] analyzed the image quality for the observed breast thickness of 250 subjects using film-screen mammography. The difference in breast thickness and image quality between the MLO and CC paired images were computed. According to the authors, image sharpness decreased by 19% for 1 cm of increased breast thickness. In addition, contrast loss was observed due to scatter augmentation and beam hardening.

Later, Saunders R.S. et al. [128] have studied the effect of breast compression on mass conspicuity in digital mammography using Monte Carlo based simulation framework. The

simulation was done for two breast thicknesses (*4 cm and 6 cm*) with two compression levels (standard and reduced compression by 12%) and three photon flux conditions (constant flux, constant detector signal, and constant glandular dose). The results suggest that if a particular imaging system can handle an approximately 10% increase in total tube output and 10% decrease in detector signal, breast compression can be reduced by about 12% in terms of breast thickness with little impact on image quality or dose.

O'Leary D. et al. [102] performed a clinical study to assess the image quality in function of the applied compression force for digital mammography. The CC and MLO views of 4790 subjects were analyzed and image quality was categorized as perfect, good, moderate or inadequate. The results have shown that the image quality is highly correlated with the applied force. The mean compression force required to produce a perfect image was found to be equal to 121.34 N for a CC view and 134.23 N for a MLO view.

#### **4.4.2 Average glandular dose**

A mammography unit uses X-rays to obtain 2D-projection images from the breast tissues. As for any X-ray exposure, the irradiation of a targeted population is accepted if the benefits are significantly higher than the risks. Therefore, mammography exposures must provide a good image quality while preserving the radiation dose *as low as reasonably achievable*.

To assess the quality of breast compression, the risk from the X-ray exposure have to be considered. The absorbed energy from digital mammography depends on many factors such as the breast density, the breast thickness, the volumetric distribution of glandular tissues as well as the acquisition parameters.

It has been proved that glandular tissues of the breast are more vulnerable to radiation carcinogenesis than skin, adipose tissue, or areola [65]. Based on these findings, the average glandular dose (AGD) was defined to quantify the risk from breast irradiation and is widely accepted for regulations. The most often used method calculates the AGD as the product of the incident air kerma<sup>1</sup> at the upper surface of the breast with conversion factors called *normalized dose*. The normalized dose (DgN) is computed as a function of spectrum, breast thickness and breast density. Its computation is based on Monte Carlo simulations [31, 14].

Historically, only rigid paddles were used for breast cancer screening. Therefore, in numerical simulations, the breast is usually modeled as a flat semicircular object with a homogeneous content and surrounded by a layer of skin. The attenuation coefficient of the content corresponds to the breast density, the ratio of the amount of gland to total breast [31].

When a flex paddle is used, the breast thickness decreases towards the nipple side, resulting in a wedge-shaped breast. Since the AGD model assumes a flat shape, apart from inherent uncertainties due to general assumptions concerning breast geometry and composition, additional uncertainties due to the paddle tilt are included. In a clinical framework, no difference is made between the flex and the rigid paddles for the AGD

---

<sup>1</sup>radiation dose measurement at a point on a patient's skin

computation [15]. To our knowledge, the associated errors are not quantitatively described in the literature.

Recent reports have updated dose estimates from screen-film mammography (SFM) and full field digital mammography, indicating that two-view screening with FFDM delivers a slightly lower dose than does SFM. The mean average dose was estimated for different populations. A geographical classification shows that the AGD delivered by digital mammography for a European woman ( $1.48mGy$ ) is higher on average than the one for North American ( $1.42mGy$ ) or Asian woman ( $1.42mGy$ ) [55]. Osteras B. and colleagues [104] have classified the CC and MLO view of 3819 women in two classes by breast density. The authors reported a mean AGD of  $1.73mGy$  for the dense breasts and an AGD of  $1.74mGy$  for the fatty breasts. The AGD was estimated using the model proposed by Dance D. et al. [31].

#### 4.4.3 Pain and discomfort

Many women have reported discomfort or pain during mammography exams. A literature review over the last decades shows that the prevalence of pain varies widely, the percentage of women experiencing pain or discomfort ranging between 16% and 72% [79, 110, 37, 144]. This difference could be due to the interpretation of pain intensity (i.e. distinction between *pain* and *considerable pain*), but also could be attributed to differences in the instruments used to measure pain.

Pain intensity is influenced by the meaning of the pain to the patient and its expected duration. The environment also has an impact on the experience of pain, as do expectations, attitudes and beliefs. Pain is rarely caused by psychological factors, but is associated with psychological and emotional effects such as fear, anxiety and depression [146].

The three most-used pain metrics in clinical studies are the visual analogue scales, the numeric rating scales and the verbal rating scale [146]. The **visual analogue scale** (VAS) is presented as 10-cm continuous line together with a verbal descriptors at the line's ends (no pain and worst imaginable pain). The patient is asked to mark the pain intensity on the line. The score is measured from the zero to the patient's mark using a millimeter scale which provide 101 levels of pain intensity. The **numerical rating scale** (NRS) is a discrete point scale were the end points are the extremes of the pain range. In mammography, a 6 or 11 point scale is generally used. The patient will mark the point corresponding to the perceived pain intensity. The **verbal rating scale** (VRS) comprises a list of adjectives used to denote increasing pain intensities, such as no pain, mild pain, moderate pain and severe pain. The patient will choose the adjective corresponding to the perceived pain intensity. According to Williams M. et al. [146] the numerical rating scale provides the best trade-off between metric sensitivity and the metric repeatability.

In mammography, the pain experienced by women during the exam depends on psychological (technician behavior, patient anxiety) [8], sociological (ethnicity, education level) [37] and physiological factors (compression level, breast size)[116]. It was found that, the main factors associated with the patient discomfort are the satisfaction with care and the perception of the technologist's *roughness* [37]. Besides this findings, several studies have

also suggested the pain expectation and the anxiety level as ones of the main risk factors associated with the pain [8, 146, 79, 10].

The physiological factors such as breast thickness, breast size or periods are also positively correlated with the patient comfort [79, 64]. The relationship between applied compression force, breast thickness, reported discomfort and image quality has been studied by Poulos A. et al [116]. According to the authors, the patient comfort decrease with the compressed breast thickness. The authors reported a significant relationship between patient discomfort and breast thickness. However, no significant relationship between the reported discomfort of the procedure and the applied compression force was found. According to the authors, force does not correlate well with subject discomfort since it does not account for differences in breast thickness.

A painful mammography contributes to non-re-attendance. Twenty five percents of US women rated their experience of screening 30 months after their latest mammogram as at least moderately painful [110]. It is thus plausible that remembered pain can possibly dissuade women from attending later screening exams.

## **4.5 Recent advances in breast compression**

Breast compression is an important part of mammography exams. A good breast compression improves image quality, better separates breast tissues structures and reduces the absorbed dose. In the same time, breast positioning and compression are the main sources of discomfort experienced by patients. Because anxiety is documented to be the most important contributor to procedural pain, interventions designed to reduce both physical and psychologic discomfort are needed.

Considering the previous listed risk factors, various pain reducing techniques concerning the usual care were proposed during the last years [95]. To decrease the patient anxiousness and pain expectations, verbal and written information was proposed prior to mammogram. Informing the patients and accompanying them during the exam have shown to decrease the population mean pain score from 25 to 17 in a 100-mm VAS [129]. In the same time, the effect of some relaxation techniques has been studied. Domar A. et al. [35] compared the perceived pain from an usual mammogram to the one accompanied by music or a relaxation audiotape. The music subjects had a choice of classical music, jazz, or soft rock. The relaxation audiotape contained information that led the subject through breath focus, body scan, and meditation. According to the authors, there was no significant difference in perceived pain between the various groups.

Later, with the emergence of digital mammography, pain reducing compression techniques were proposed. Several studies [26, 128] suggest that the compression force may be reduced by at least 10% without a significant impact on image quality or average glandular dose. However, according to Poulos A. et al. [116], the patient comfort is not related to the applied force intensity but to the compressed breast thickness, which in its turn is associated with the breast size and firmness. To achieve the optimal compression considering the patient breast specific morphology, a pressure controlled compression is recommended.

instead of a force controlled compression [33]. The recommended target pressure is equal to  $10 \text{ kPa}$ . For a clinical integration, the ~~SegmaScreening~~ company has proposed a new standard rigid paddle with integrated pressure control while the Volpara Solutions company has proposed a software computing the contact area between the breast and the compression paddle in order to extrapolate the mean applied pressure. In the same time, Dustler M. et al [39] analyzed alternative breast ~~positioning~~ according to previously found pressure distribution patterns. Because of stiff juxtathoracic structures, the authors proposed to increase the distance between the compression paddle and the chest wall by 1cm. The results have shown that within the new breast positioning, the pressure is reduced on the juxtathoracic area. The breast thickness was decreased by  $4.4 \pm 2.3 \text{ mm}$  with no significant effect on force intensity. However, the six participants have identified the repositioned compression as the most painful, which, according to the authors, may be explained by the higher pressure intensities on the overall breast surface itself. The main drawback of this technique is the exclusion of juxtathoracic tissues which may obscure small posterior suspicious lesions.

According to latter studies, several constructors started to propose various solutions to reduce the physical discomfort during mammography. Hologic company proposed the MammoPad cushion which is claimed to reduce the discomfort by 50%. In the review proposed by [95], such radiolucent breast cushions are supposed to reduce the pain score (100mm VAS) from 35 to 20 in CC view and from 43 to 26 in MLO. GE Healthcare company proposed a patient-controlled breast compression with the new Senographe Pristina system. This technique lets women controlling ~~them selves~~ how much the device compresses their breasts. The breast is firstly positioned by the technologist between the compression plates; then, the patient is terminating her compression up to a level she can support. It has been shown that the patient-controlled compression is less painful than the technologist-controlled compression with no significant impact on image quality [95].

The breast positioning is a fastidious task for the technologist. For example, a larger amount of posterior tissue included in breast compression may result in a ~~thicker breast~~ at the anterior area, which in ~~its~~ turn may reduce the image quality and hide important clinical information. The technologist has the critical job of applying positioning methods using common sense. If the breast area is not well covered by the first two projections, an additional third projection may be necessary. The use of flex paddles proposed by some constructors, such as American Mammographics S.O.F.T. Paddle, GE Healthcare Flex Paddle or Hologic FAST Paddle aims at increasing the area of compressed tissues and thus avoiding an additional projection.

To our knowledge, there is only one study assessing the difference in image quality, average glandular dose and patient comfort between flex and rigid paddles [15]. According to the authors the flex paddle affects the technical image quality without improving the patient experience. Because the flex paddle pulls the soft tissues towards the pectoral wall, they are less visible in the image. It must be highlighted that the study of Broeders and colleagues included CC and MLO projections with force-controlled compressions (target force between 12-20 daN). Based on the same principle as the study presented by Dustler M. et al [39], one may guess that breast compression with a flex paddle will result in

*CHAPTER 4. BREAST COMPRESSION  
STATE OF THE ART*

---

a higher pressure over the breast surface itself (less pressure on the juxtathoracic area which may be the origin of the pain over the breast surface). It may be interesting to assess the patient discomfort and the image quality with a pressure-controlled compression. Moreover, the average glandular dose is computed by neglecting the wedge form of the flex paddle, therefore it is difficult to compare the flex and the rigid paddles.

To better quantify the difference between flex and rigid paddles, further investigations are needed. In this scope, we have developed a simulation framework allowing to assess breast compression quality ~~in~~ function of breast patient specific morphology and compression paddle design.

This framework is presented in the next chapter, where the breast compression modeling by finite element as well as the numerical methods to assess the corresponding image quality and the average glandular dose are described. In a numerical environment, it is almost impossible to model the psychological patient discomfort, thus this work is focused on analyzing the patient physical discomfort which here is assumed to be associated with tissues internal strain/stress due to breast compression. Ultimately, the breast compression quality for CC view is evaluated for flex and rigid paddles and for various paddle positions.

## BREAST COMPRESSION & COMFORT

### *A comparative study*

In this chapter, a numerical simulation able to replicate the existing breast compression techniques was developed. This tool is used to compare different breast compression paddles considering the patient experience as well as the image quality and average glandular dose. The breast biomechanical model described in Chapter 3 was used to create two different breast models corresponding to the two involved volunteers. To simulate breast compression, finite element models of standard paddles were developed and put in contact with the two breast models.

First, a comparative study is performed between various paddle designs. The compression of the right breast of both volumes was simulated with flex and rigid paddles. We propose to quantify the perceived pain for a given paddle design through three entities, namely contact pressure, internal stress and strain distributions. After compression, a set of virtual macrocalcifications were inserted into the breast volumes. A Monte-Carlo based simulation mimicking the acquisition of images with a mammography system was applied to the breast volumes. Then, the imaging performance was assessed by measuring the signal-difference-to-noise-ratio (SDNR), the signal-to-noise-ratio (SNR) and the average glandular dose (AGD).

Finally, the compression mechanics was analyzed as a function of breast positioning. To this end, the breast geometry of the second volunteer was compressed with different paddle positions with respect to the chest wall. The patient comfort was assessed for three paddle positions.

## 5.1 Breast compression modeling

In chapter 3 a new biomechanical breast model was proposed. An optimization process was developed allowing to determine subject-specific breast stress-free geometry and the corresponding mechanical properties. At this stage, the exhaustive semi-automatic research of the constitutive parameters is computationally expensive to perform. Therefore, because of lack of time, the model calibration was carried out for the first volunteer only. However, to perform a qualitative study comparing different paddle models, data of more than one subject is needed. To provide our study with a larger data set, the biomechanical breast model of the second volunteer was created without performing the model calibration to the subject specific mechanical properties. This model represents a new realistic breast geometry with a larger volume and different tissues mechanical behavior which will not characterize the breast mechanics of the second volunteer.

To simulate breast compression, finite element models of compression paddles were developed. The realism of these simulations was evaluated by comparing the resulting breast thickness and the applied force to the corresponding data measured during the most recent mammogram of both volunteers. The resulting mechanical response revealed the limitations of a Neo-Hookean strain energy function and the necessity of updating the tissues constitutive models.

In the following section, first the designed compression paddles were introduced. Then, the compression mechanics as simulated using the biomechanical breast model are described. Accordingly, the constitutive models of breast tissues were reviewed and a new form of the strain energy density function was proposed.

### 5.1.1 FE modeling of compression paddles

In this study, standard paddles (standard rigid and flex paddles) generally used for regular screening were considered. Only one paddle geometry was modeled based on the technical specifications from a Senographe Pristina mammography unit. Three different paddle models were created.

First, the paddle flexibility due to its material properties was neglected. The rigid paddle model (RPM) was therefore defined as a fully rigid body with only one translational degree of freedom in the downward direction.

Then, for the flex paddle model (FPM), a rotation around the longitudinal axis was added. The additional degree of freedom was modeled using a rotational-only joint type of element. The joint stiffness was computed by fitting the force-deflection curve of a standard flex paddle measured on a Senographe Pristina unit. For this, a rigid plate was fixed perpendicularly to the image receptor at its external edge, in order to block the SFP translation degree of freedom (Figure 5.1.a). To ensure the paddle rotation around the  $Oy$  axis only, the rigid plate was chosen to have the same length (in  $Oy$  direction) as the compression paddle. The deflection angle was measured using a digital inclinometer ( $\pm 0.1\text{deg}$  accuracy). The paddle was lowered progressively, such as the deflection angle was

incremented by steps of 0.5 *degrees*, until the maximal recommended compression force was reached ( $F = 200N$ ). At each step, the compression force was read from the calibrated mammography unit. The experiment was repeated 3 times. The relation between the mean compression force and the deflection angle is shown in Figure 5.1.b. An estimated second-degree polynomial was used to define the joint stiffness for the FE analysis.

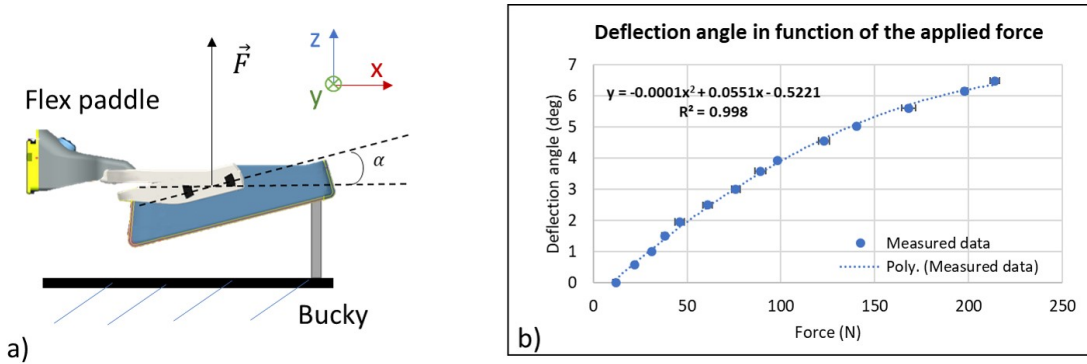


Figure 5.1: a) Experiment set-up, b) Deflection angle as function of the applied force

As concerns the third paddle model, namely the elastic paddle model (EPM), the deflection due to the material properties was included. The paddle thickness was set to 4mm and it was made of Lexan material ( $\lambda_{lexan} = 2250 \text{ MPa}$  and  $\nu_{lexan} = 0.4$ ). Only one translational degree of freedom in the downward direction was considered. The paddle was modeled using shell elements.

For the three paddle models, the interaction between the compression paddles and the breast was modeled using a frictionless contact. The penalty algorithm was used with a penetration factor equal to 0.1 and a contact stiffness equal to 1.

### 5.1.2 Breast compression mechanics

The realism of breast compression simulations was verified by confrontation with real data. The compression of a small breast, like the one we have for the first volunteer, may be complex. Sometimes the technologist has to hold the breast between the image receptor and the paddle until the compression force is high enough to preclude the breast from sliding outside of the image receptor field of view. This difficulty is also present in a simulation framework, especially since we do not simulate the breast positioning gesture by the radiologist. To facilitate the compression process during the evaluation step, it was therefore decided to use only the larger breast geometry provided by the second volunteer.

In a clinical framework, woman breasts are compressed in an up-right or prone body positions. Under compression, the gravity induced tissues pre-stresses can be neglected when compared to the compression-induced stresses [67, 124, 133]. Therefore, the prone breast configuration was used as the reference configuration, neglecting the tissues internal pre-stresses due to gravity loading. The breast compression was simulated using the rigid and flex paddle models.

**CHAPTER 5. BREAST COMPRESSION & COMFORT**  
**A COMPARATIVE STUDY**

---

Prior to breast compression simulations, the breast biomechanical model corresponding to the geometry of the second volunteer in prone configuration was developed. The optimization problem estimating the set of constitutive parameters is expensive in terms of the computation time. Therefore, for this chapter, we decided to replace the tissues constitutive parameters of the second volunteer, with the ones found in the literature [66, 118, 57]. The corresponding equivalent modulus for each involved tissue was chosen the following:  $\lambda_{breast} = 0.5kPa$ ,  $\lambda_{muscle} = 10kPa$ ,  $\lambda_{skin} = 10kPa$ ,  $\lambda_{fascia} = 160kPa$ . Of course, with this assumption, this new biomechanical model does not properly represent the breast mechanics of the second volunteer. However, it provides a realistic model with a larger breast volume and with stiffer breast tissue which may be used in a comparative study between various compression strategies.

The cranio-caudal incidence was modeled by positioning the image receptor at the inframammary ligament level while the paddle compresses the breast by a downward movement. The compression was stopped when the target breast thickness was reached. Such target thickness was given by the data recorded during the most recent mammogram of the second volunteer (Table 3.1). Figure 5.2 shows the breast thickness as function of the applied force for the flex and the rigid paddles. The breast thickness for the flex and the rigid paddles was considered constant. For a rigid paddle, the distance between the paddle and the image receptor was considered, named  $h_r$  (Figure 5.2). Concerning the flex paddle, distance between the image receptor and the paddle was measured at two distinct points, first at the nipple level (named  $h_1$  in Figure 5.2) and the second at the breast base (named  $h_2$  in Figure 5.2). Therefore, the breast thickness for the flex paddle (named  $h_f$  on Figure 5.2) is given by the mean value of  $h_1$  and  $h_2$ .

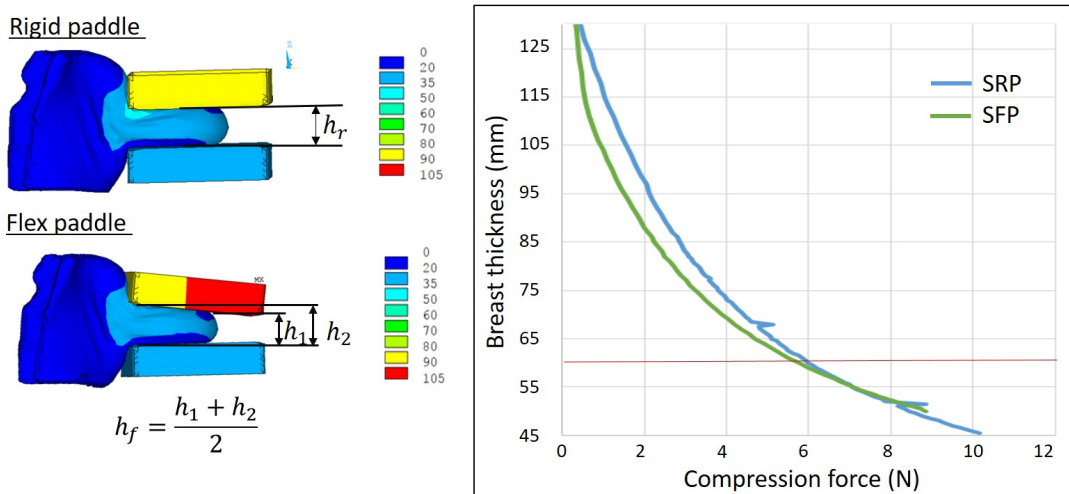


Figure 5.2: Breast flattening curve as function of the applied force for a Neo-Hookean strain energy function. SRP - standard rigid paddle, SFP -standard flex paddle

Several irregularities can be observed over the curve describing the force-thickness relation when the breast is compressed with a rigid paddle, this numerical artifacts are due

to inherent finite elements discretization errors. One can see that, the total compression force at the target breast thickness ( $50mm$ ) is about 15 times lower than the force measured during the volunteer's last mammography ( $6N$  versus  $94.8N$ ). Even if the chosen constitutive models were not accurately adapted to the patient mechanical properties, a force of  $6N$  remains too low when compared to the standard compression force of  $120N$  [26]. Usually, a larger force is applied when compressing such large breast volumes as the one of the second volunteer. Several compressions were tested (e.g. paddle closer to the juxtathoracic area, frictional contact with different friction coefficient) without observing any significant increase of the compression force.

An analysis of the literature revealed that the constitutive parameters used to model breast compression are usually higher than the ones used to model the breast deformation under gravity loading. For example, Sturgeon G.M and colleagues [133] have estimated the tissues deformation under compression considering the initial shear modulus for a Neo-Hookean strain energy function equal to  $\mu_{skin} = 88kPa$ ,  $\mu_{adipose} = 1kPa$  and  $\mu_{glandular} = 10kPa$ . Moreover, our simulations did not demonstrate the asymptotic behavior of the compression force versus breast thickness, as described by Groot J. et al. [33]. One can conclude that, for high strains, the soft tissues undergo a stiffening process more rapidly than the stiffening as described by a Neo-Hookean law.

The limitation of the Neo-Hookean model to capture the mechanical response of some nonlinear materials is well known [77]. For large strain rates, the Neo-Hookean material may undergo a relaxation and thus become easier to deform. Therefore, another strain energy model has to be considered for the modeling of breast compression.

### 5.1.3 Gent strain energy function

Giving that the Neo-Hookean strain energy function provide a poor estimation for large strains, the Gent strain energy function (see Section 2.1.4.a) can be used as an alternative model. The Gent function is characterized by three parameters ( $\mu$ ,  $K$ , and  $J_m$ ). For small strains, it is resumed to the Neo-Hookean model [22]. For large strains, the  $J_m$  parameter acts as a stiffening parameter and defines the upper limit of the first invariant of the left Cauchy-Green deformation tensor (Figure 5.3.a). When  $J_m \rightarrow \infty$ , the Gent model is reduced to the Neo-Hookean model even for large strains (Figure 5.3.a).

These properties are particularly interesting for our simulation framework. In chapter 3, the material properties have been estimated and validated for multi-loading gravity simulations. Therefore, the tissues mechanical behavior is well estimated for relatively small strains. The strain range due to breast compression is significantly larger than the one due to gravity loading. In this respect, the  $J_m$  parameter may be estimated such that, for relative small strains, the Gent model remains equivalent to the Neo-Hookean model. However for larger strains, the energy function will behave asymptotically to approach a compression force equivalent to the standard compression force (Figure 5.3.b). Then, only the third parameter of the energy function has to be estimated ( $J_m$ ), the initial shear modulus ( $\mu$ ) and the Bulk modulus ( $K$ ) being already known from the multi-loading gravity optimization process.

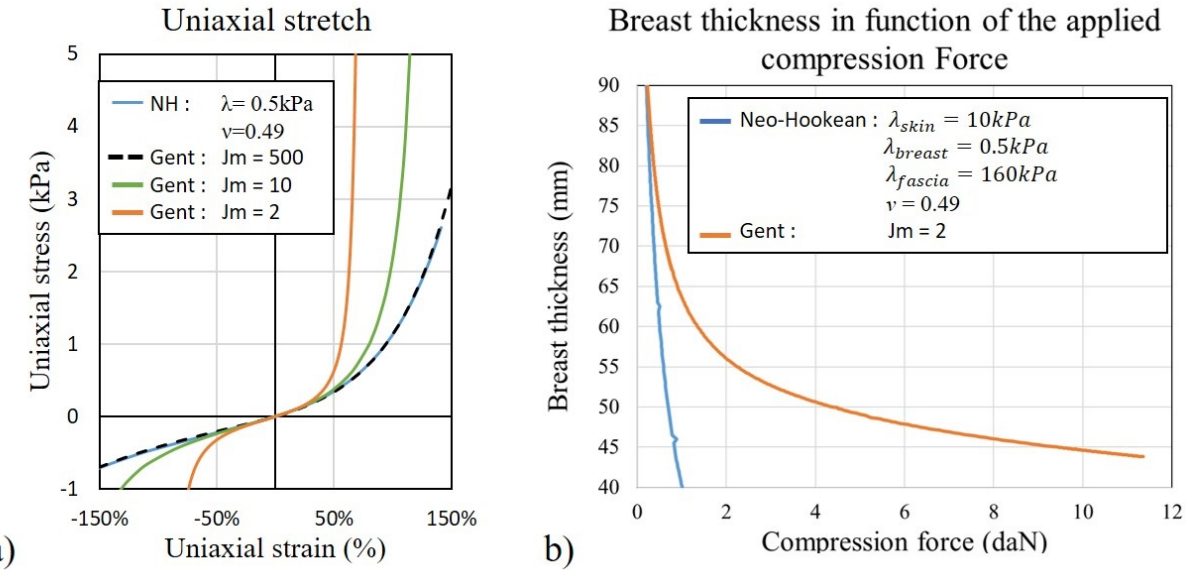


Figure 5.3: a) Stress-strain relation for Neo-Hookean and Gent energy functions; b) Breast flattening curve as function of the applied force for a Gent energy function.

Figure 5.3.b shows the breast flattening curve as function of the applied force when using Neo-Hookean and Gent material models. One can see that, when using the Gent model the curve shape is closer to the results described by Groot J.E. and colleagues [33] from experimental data on real patients. Moreover, for a breast thickness of 45 mm, the compression force obtained with the Gent material model is 10 times higher than the one obtained with the Neo-Hookean material model, i.e. 10 N versus 100 N (Figure 5.3). The Gent model definitively provides more realistic simulation results. Therefore, in the next section, the constitutive parameters of the Gent function will be estimated in order to improve breast compression mechanical behavior for both breast models.

### 5.1.4 Updated material constitutive models

We have seen that a Neo-Hookean model can not describe correctly the breast mechanics under compression. The force needed to flatten the breast during simulation was too small when compared to the mean compression force measured in mammography. The Gent model showed to perform better, giving a more realistic breast flattening curve as function of the applied force (Figure 5.3). Therefore, to compute tissue deformations under compression, the Gent energy function was used.

For the following, the compression simulations were performed on the right breast only. The constitutive parameters for the Gent energy strain function were chosen as follows. For the first volunteer the tissues mechanical properties have already been estimated. Therefore the equivalent Young's modulus of each tissue was kept as defined by the multi-loading gravity simulations ( $\lambda_{\text{breast}}^r = 0.3 \text{ kPa}$ ,  $\lambda_{\text{muscle}} = 10 \text{ kPa}$ ,  $\lambda_{\text{skin}} = 4 \text{ kPa}$ ,  $\lambda_{\text{fascia}} =$

120kPa). For the second volunteer, the constitutive parameters are unknown. However, in order to build up a new mechanical behavior, different from the first volunteer, the equivalent Young's modulus as described in the literature can be used. The appropriate values were selected among studies which have provided an in-vivo parameters estimation within similar frameworks ( $\lambda_{breast}^r = 0.5\text{kPa}$ ,  $\lambda_{muscle} = 10\text{kPa}$ ,  $\lambda_{skin} = 10\text{kPa}$ ,  $\lambda_{fascia} = 160\text{kPa}$ ) [66, 118, 57]. Therefore, the second model represents larger breast volume with stiffer tissues.

To estimate the  $J_m$  parameter, additional information was needed. To this end, the subjects were asked to provide the data from their most recent mammogram. Several compression simulations were performed to estimate the  $J_m$  value that gives the compression force and the breast thickness as measured during the mammography ( Table 3.1). The Poisson ratio for these simulations was changed to 0.499 (nearly incompressible material allowing a better convergence of the simulations). According to the sensitivity analysis performed in Chapter 3, this change does not significantly impact the mechanics of the small breast volume in the multi-loading gravity framework. For the first volunteer, a breast thickness of 46mm with a compression force of 22N is obtained with  $J_m = 1$ . For the second volunteer, a breast thickness of 48mm with a compression force of 95N is obtained with  $J_m = 2$ .

Figure 5.4 shows the breast flattening curve as function of the applied force obtained with rigid and flex paddle models. All simulations were performed with the Gent strain energy function.

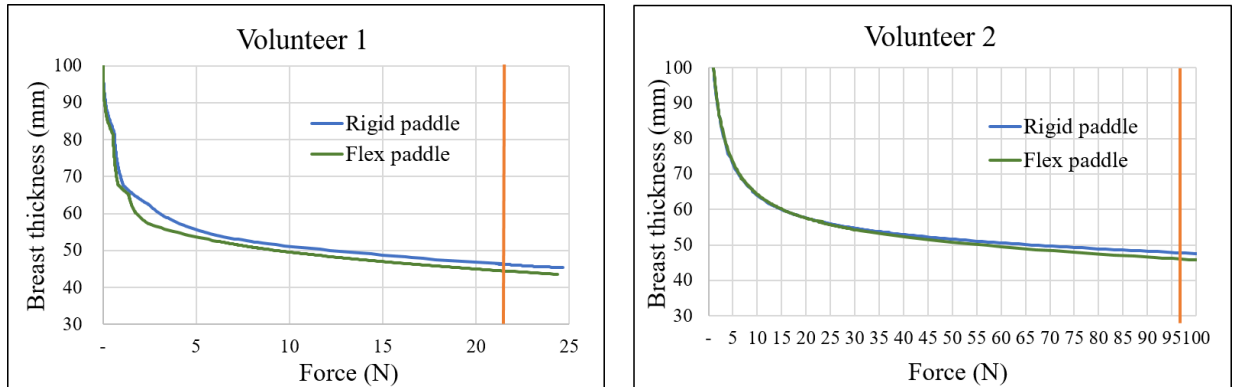


Figure 5.4: Resulting breast flattening curve as function of the compression force with Gent constitutive model.

One can see that the compression force range is comparable with the one measured during mammography. Moreover, the curve behavior is similar with the one given by Groot J.E. et al [33], with an asymptotic behavior at the end of breast compression.

In this section, it was assumed that introducing a Gent strain energy function will have a non-significant impact on breast mechanics under gravity loading since the Neo-Hookean and the Gent models have similar behaviors for small deformations. Therefore we can consider that the previous optimization process performed on the breast volume of the

first volunteer remains valid.

### 5.1.5 Gent model and breast mechanics under gravity loading

When looking back to the Gent function properties, an appropriate  $J_m$  parameter was defined as following. The  $J_m$  value has to be small enough in order to obtain an appropriate compression force. And in the same time, it has to be high enough in order to preserve the model fidelity to the gravity loading deformations.

In Chapter 3, the biomechanical breast model corresponding to the first volunteer was evaluated for Neo-Hookean material models. The worst estimate was found in supine tilted configuration due to the tissues over sliding on the lateral direction (maximal distance of 26.03 mm). Introducing Gent tissues model should not impact the breast deformation under gravity loading. However, when looking at the supine tilted configuration simulated with Neo-Hookean material, large deformations were observed at the fascia and skin surfaces. Figure 5.5 shows the strain rates in supine, prone and supine tilted configurations obtained with Neo-Hookean material models. The strain rates over the skin and fascia surfaces in supine tilted configuration were twice larger than ones observed in supine and prone breast configurations. Therefore, considering the Gent model in the multi-loading gravity simulations may improve the supine tilted estimate by reducing the fascia and skin deformations under large strain.

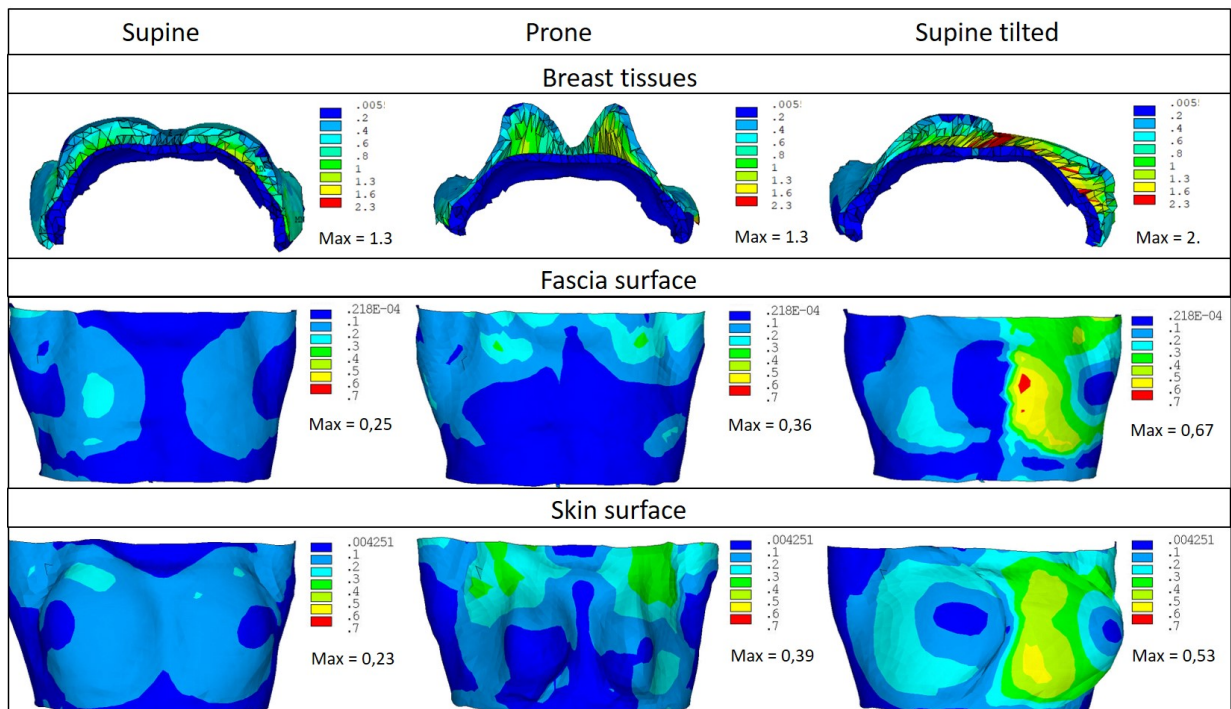


Figure 5.5: Strain range distribution when using a Neo-Hookean material model.

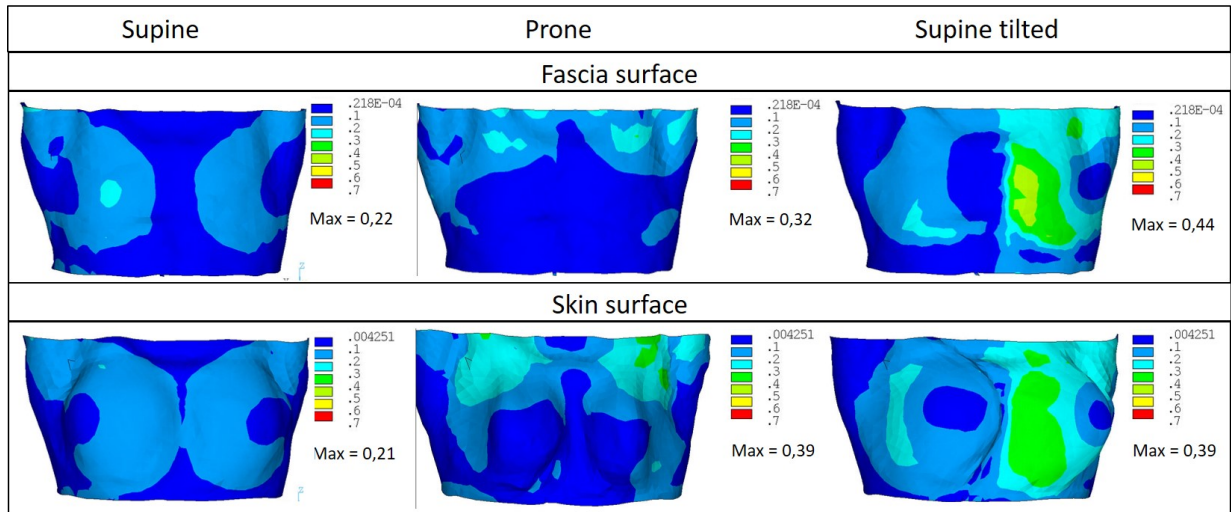


Figure 5.6: Strain range distribution when using a Gent material model.

Several simulations were performed considering  $J_m = 1$ , as identified during the compression simulations. However this value seems to constrain too much the tissues deformation in prone and supine configurations. It will be shown that the compression force is highly dependent on the paddle positioning with respect to the chest wall (Section 5.4.2). For an accurate estimation of the parameter  $J_m$ , more data is needed concerning the paddle position during compression. In our study, the paddle position with respect to the chest wall was not available. Therefore, the estimated  $J_m$  value is only an approximation and does not characterize completely the subject breast mechanics.

When the multi-loading gravity simulations were performed using a Gent model with  $J_m = 2$ , better estimates were obtained. In this respect, to show the impact of using a Gent model within multy-loading gravity simulations, the parameter  $J_m$  of all involved tissues was set to 2. Figure 5.6 shows the corresponding strain range distributions over the skin and fascia surfaces. The maximal strain does not change significantly in supine and prone configurations ( less than 10% of difference). On the other hand, important changes were observed over the left breast in supine tilted configuration. The maximal strain range decreased by about 30% over the fascia surface and by about 26 % over the skin surface. As previously described, these tissues provide the breast support, accordingly, the lateral displacement of the left breast was reduced.

The estimates of breast external geometry in the three configurations computed using the Gent material models are presented in Figure 5.7. One may see that the breast deformations in supine and prone configurations remain on the same range of precision. The Hausdorff distance being increased by only 0.46 mm and 0.6 mm respectively (maximal distance by 0.17 and 0.93 mm respectively). Contrariwise, the sliding of the left breast was significantly reduced. Even if the Hausdorff distance was reduced by only 1 mm (5.15 mm with Gent models versus 6.14 with Neo-Hookean models), an significant decrease of 10 mm in maximal distance was observed. Moreover, smaller deformations imply

*CHAPTER 5. BREAST COMPRESSION & COMFORT  
A COMPARATIVE STUDY*

---

also better solution convergence.

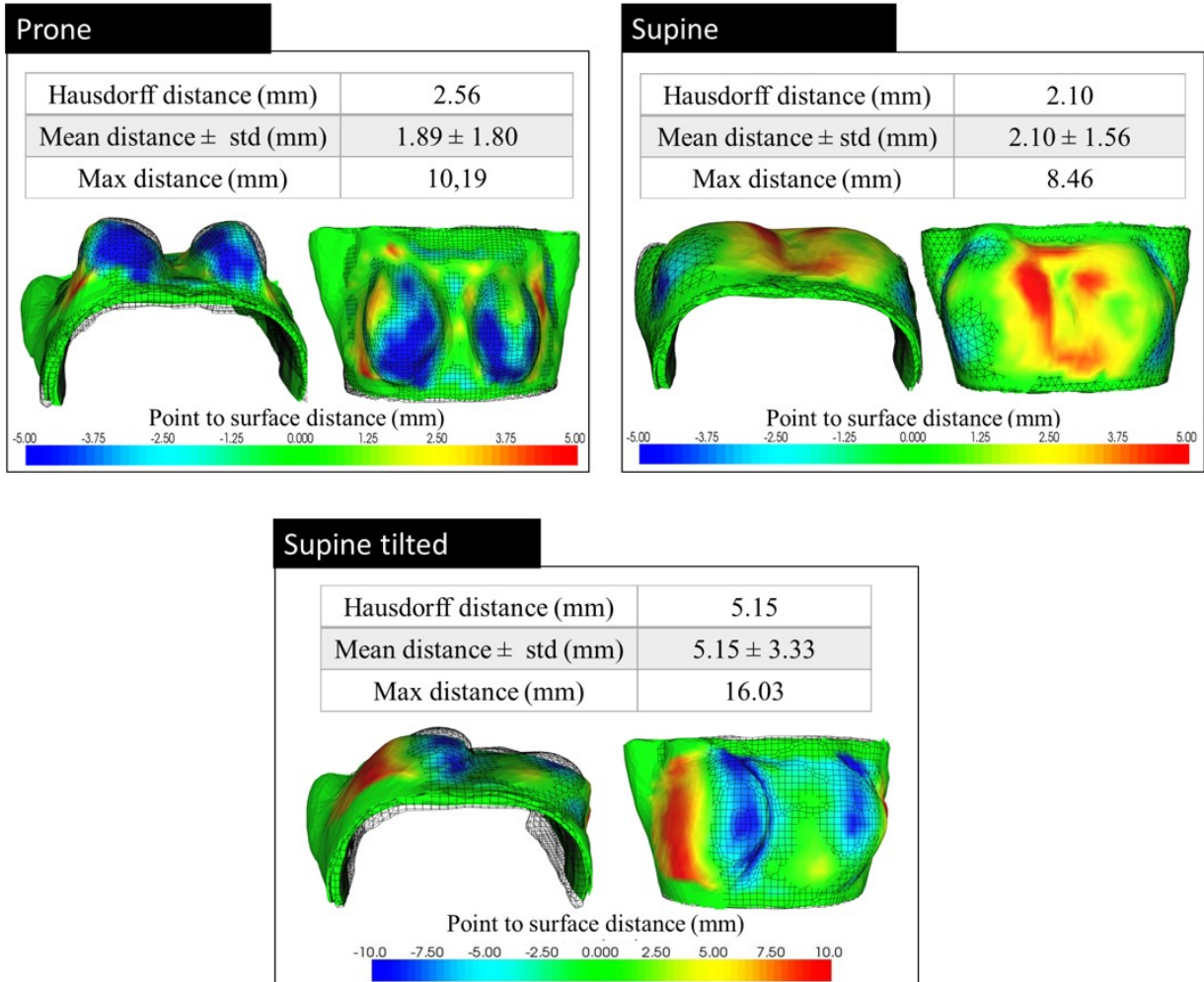


Figure 5.7: Difference between estimated and measured breast surfaces, in supine, prone and supine tilted configurations obtained with a Gent material model.

Using the Gent model improved the overall performance of the breast biomechanical model. However, different values of parameter  $J_m$  were used to simulate breast deformations under compression and under gravity loading. A more detailed study is needed to find appropriate constitutive parameters characterizing a wider panel of breast deformations.

In this chapter we assumed a constant value of  $J_m$  for all involved hyperelastic material models, yet their mechanical response under large stresses are different. A variable  $J_m$  parameter within tissues types may improve model accuracy. On the other hand, it also implies an optimization process with more constitutive parameters. An optimization process with a higher number of variables is also more expensive in terms of data and time resources.

For the breast compression simulations presented below the parameter  $J_m$  for the first

volunteer was set to 1. This assumption satisfies the thickness-force relation obtained during the mammography exam.

## 5.2 Simulation of digital images

Once the compression simulations were performed, the compressed breast geometry was extracted and used to create numerical object defined by the means of a surface meshes, also named numerical phantoms. These objects were used as input for the CatSim environment able to simulate a digital mammography acquisition [32, 34]. The simulated images were used to assess the image quality as function of the compression paddle design.

### 5.2.1 Physical characteristics

The X-ray projections of phantom objects were simulated using a GE Senographe Pristina system topology (Figure 5.8). The focal spot was modeled as a point source. A 24 keV mono-energetic X-ray beam was considered. This beam quality is similar to the effective X-ray energy of a 34 kVp Rh/Ag target/filter spectrum filtered by a 46 mm compressed breast. Spreading of the light photons in the CsI scintillator of the detector was modeled by filtering the detected X-ray beam by an empirically assessed modulation transfer function of the cesium iodide (CsI) scintillator. X-ray scatter from the test object and other system components were not included in the simulation. Only quantum noise, modelled by a Poisson random distribution, was considered as noise source. The simulated x-ray flux was tuned to match the average signal intensity ( $\langle SI \rangle$ ) and signal-to-noise ratio (SNR) measured in real images of a 46 mm thick, 20% fibroglandular equivalent phantom acquired with the automatic exposure control. To do so, a calibration was performed on a real Senographe Pristina mammography unit.

### 5.2.2 Breast phantom objects

The phantoms were created by first extracting the compressed breast external shape. Then, a set of virtual microcalcifications ( $\mu calc$ ) were inserted into each compressed breast volume. The smallest breast volume contains 21 microcalcifications arranged in a matrix of 7 rows and 3 columns (Figure 5.9.a). The largest breast volume contains 56 microcalcifications arranged in a matrix of 7 rows and 8 columns. The matrix of  $\mu calc$  was parallel with the entrance surface of the image receptor and was positioned at the breast mid thickness (Figure 5.9.b). The distance between two consecutive columns or rows was equal to 10 mm. The anatomical background was assumed to be a uniform breast-equivalent material composed of glandular/adipose tissue with a 20/80 ratio. Two simulations were performed for each compression considering microcalcifications of 0.2 mm and 0.3 mm in diameter.

Microcalcifications were simulated as round-shaped surface mesh. To add irregularities, initially spherical objects were randomly deformed. Their X-ray attenuation properties

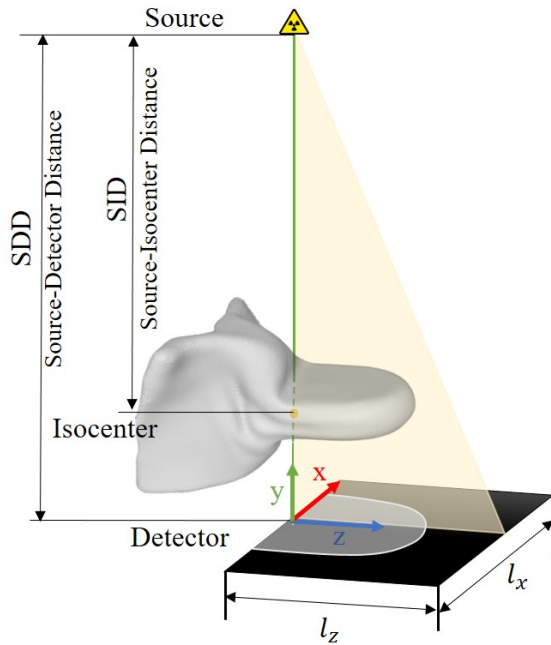


Figure 5.8: A schematic illustration og the simulated GE Senographie Pristina TM mammography unit.

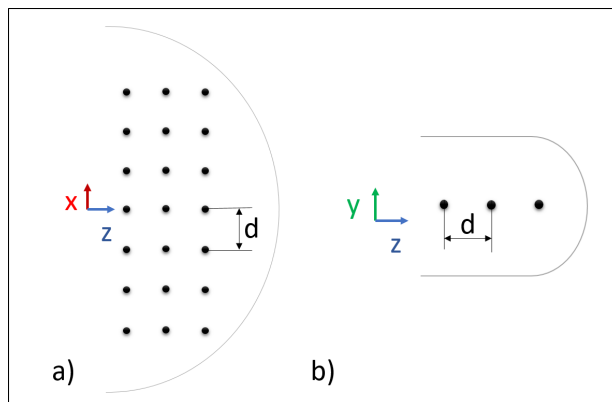


Figure 5.9: Microcalcification distribution over the smallest breast volume ( $d = 10\text{mm}$ ):  
a) axial view, b) sagittal view.

were chosen to correspond with the attenuation of aluminium (Al) at 24 keV, their volumetric mass density correspond to 60% of the Al density (i.e.  $1.63 \frac{\text{kg}}{\text{m}^3}$ ). The choice of 24 keV corresponds to the photon energy of the x-ray source used in our study.

## 5.3 Compression quality metrics

The measures used to quantify the three criteria characterizing the quality of breast compression (patient comfort, image quality and average glandular dose) are described in the following section.

### 5.3.1 Patient comfort

Today, pain estimation and quantification still remain an open question. The perceived pain during mammography, or its interpretation, may depend on the social status, pain history or psychological condition of the patient. But it also depends on physical parameters such as compression force, amount of strain or pressure at skin surface. In clinical studies, the patient comfort is assessed using pain scales. The repeatability of such methods is questionable, because they are based on the patient own interpretation and expertise. More quantitative measures such as pupil dilatation or heart beat rate are interesting in assessing the patient comfort; however they may indicate not only the pain but also the fear of pain.

In this work, only physical pain associated with tissues deformations was considered. In this scope, the maximal strain and stress intensities as well as the maximal pressure intensity at the contact surface were chosen as pain quantifiers. Their distribution over the breast volume were obtained from FE simulations of breast compression and were analysed in order to compare the patient experience between two distinct compression systems.

### 5.3.2 Image quality

To assess image quality, the signal-difference-to noise ratio (SDNR) and the signal-to-noise ratio (SNR) were measured in the raw simulated images. To this end, squared ROIs of  $1\text{cm} \times 1\text{cm}$  were defined centered on the  $\mu_{calc}$ s position. The pixels inside of each ROI were divided into two sets. Pixels located at the ROI's center within a radius equal to the radius of the  $\mu_{calc}$ s represented the  $\mu_{calc}$ s attenuated signal intensity ( $SI_{\mu_{calc}}$ ). Pixels located within the ROI but outside the  $\mu_{calc}$  radius represent the background signal intensity ( $SI_{back}$ ). The two sets were used to compute the average detected signal per  $\mu_{calc}$ s pixel ( $\langle SI_{\mu_{calc}} \rangle$ ), the average detected signal per background pixel ( $\langle SI_{back} \rangle$ ) and the standard deviation in the background signal intensity  $\sigma_{back}$ :

$$\langle SI_{\mu_{calc}} \rangle = \frac{1}{|SI_{\mu_{calc}}|} \sum_{p_i \in SI_{\mu_{calc}}} p_i \quad (5.1)$$

$$\langle SI_{back} \rangle = \frac{1}{|SI_{back}|} \sum_{p_i \in SI_{back}} p_i \quad (5.2)$$

$$\sigma_{back} = \sqrt{\frac{1}{|SI_{back}|} \sum_{p_i \in SI_{back}} (p_i - \langle SI_{back} \rangle)^2} \quad (5.3)$$

*CHAPTER 5. BREAST COMPRESSION & COMFORT*  
*A COMPARATIVE STUDY*

---

Where  $|\cdot|$  is the number of pixels in the respective set.

The SDNR per pixel of the inserted microcalcifications is defined as follows

$$SDNR = \frac{\langle SI_{back} \rangle - \langle SI_{\mu calc} \rangle}{\sigma_{back}}, \quad (5.4)$$

The SNR per background pixel was defined as follows

$$SNR = \frac{\langle SI_{back} \rangle}{\sigma_{back}}. \quad (5.5)$$

### 5.3.3 Average glandular dose

The estimation of the dose delivered to the glandular tissue remains an essential component of quality control in X-ray mammography. We derived the average glandular dose using the approach proposed by Dance D. [31] regardless the paddle type. The method uses conversion factors to relate measurements of the incident air kerma  $K$  at the upper surface of the breast to the mean dose absorbed by the breast glandular tissue.

$$AGD = K gcs \quad (5.6)$$

Where  $g$  and  $s$  are conversion factors giving the AGD in function of the target/filter combination and the breast thickness (range between 20 and 110 mm) for a breast glandularity of 50%. The factor  $c$  extends the AGD estimation for different breast glandularity. Monte-Carlo simulation was used to estimate these factors by modeling the compressed breast as a semi-circular cross section cylinder.

The numerical phantom was characterized by a uniform thickness, while mammography compression implies variable breast thickness due to paddle elasticity (SRP) and paddle flexibility (SFP). In a clinical framework, the breast thickness is adjusted by applying an offset characterizing the paddle deflection during compression.

For the rigid paddle model, as paddle elasticity was neglected, the AGD was computed assuming the breast thickness is equal to the distance between the image receptor and the paddle itself. Regarding the flex paddle, the breast thickness decreases quasi-linearly from the chest wall to the nipple. Thus, breast thickness was computed as the mean of the maximal and minimal distance over the breast contact area.

## 5.4 Results

Two studies were performed using the previously defined components for modeling the breast compression and simulating digital mammography. First, the results of a comparative study between flex and rigid paddles is presented with the effects on image quality, AGD and patient comfort. Then, the impact of paddle positioning on breast mechanics is analysed.

### 5.4.1 Compression quality for rigid and flex paddles

To compare the breast compression quality when using a standard rigid paddle against a standard flex paddle, the rigid and flex paddle models were used. The right breasts of the two volunteers were first compressed until the target breast thickness measured during mammography was obtained (Table 3.1). Then, the breast phantoms with  $\mu_{calc}$  were imported into CatSim environment and mammography images were simulated. The compression quality were measured in terms of image quality, average glandular dose and patient comfort.

The resulting breast thickness after compression varies by less than 2mm between rigid and flex paddles for both volunteers (Table 5.10). Accordingly, no significant difference was found between the estimated AGD, while dose reductions of 2.6% for the smaller breast and 4.2% for the larger breast were observed in favor of the flex paddle.

Rigid Paddle		Flex Paddle		p-Values	Rigid Paddle		Flex Paddle		
Mean SNR	StdDev SNR	Mean SNR	StdDev SNR		BNT (mm)	AGD (mGy)	BNT (mm)	AGD (mGy)	
Volunteer 1	82.90	43.09	83.70	37.72	0.706	46	1.15	44	1.12
Volunteer 2	126.89	8.75	137.21	10.73	0.000	48	1.20	46	1.15

	200 um					300 um				
	Rigid Paddle		Flex Paddle		p-Values	Rigid Paddle		Flex Paddle		p-Values
	Mean SDNR	StdDev SDNR	Mean SDNR	StdDev SDNR		Mean SDNR	StdDev SDNR	Mean SDNR	StdDev SDNR	
Volunteer 1	0.74	0.68	0.79	0.54	0.689	2.01	1.28	1.85	1.02	0.224
Volunteer 2	1.14	0.57	1.13	0.53	0.885	2.96	0.76	3.15	0.92	0.093

Figure 5.10: Breast nominal thickness (BNT), average glandular dose (AGD), signal-to-noise-ratio (SNR) and signal-difference-to-noise (SDNR) for both volunteers and both compression paddle types

The SNR and SDNR have been estimated and compared between flex and rigid paddles. When using a flex paddle instead of a rigid paddle on the largest breast (volunteer 2), we observe a statistically significant higher SNR. We do not observe statistically significant differences on SDNR for both  $200\mu m$  and  $300\mu m$  microcalcifications, when using rigid or flex paddle. Therefore, despite a breast thickness varying linearly from chest wall to nipple when the flex compression paddle is used, the image quality is preserved or improved compared to the image quality obtained with the rigid compression paddle.

In a clinical study, Broeders M.J. et al. [15] have also compared the image quality and patient comfort between the standard rigid and flex paddles. According to the authors, the standard flex paddle performed slightly better image quality in the projected breast area, however it moved breast tissue from the image area at chest wall side. According to our compression simulation, for the small breast volume, no difference in tissues lateral displacement was observed. On the other hand, for the larger breast, using the flex paddle has indeed increased the tissues displacement toward the chest wall side , but not by more than 4 mm (Figure 5.11).

*CHAPTER 5. BREAST COMPRESSION & COMFORT  
A COMPARATIVE STUDY*

---

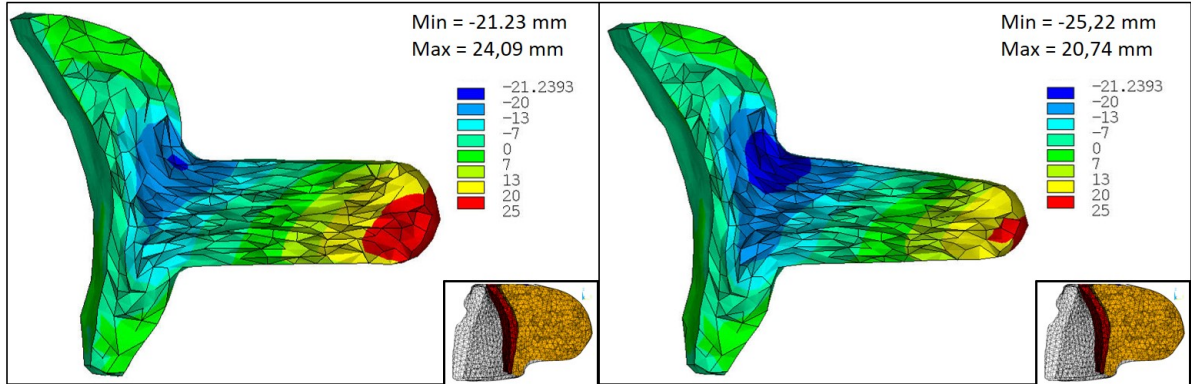


Figure 5.11: Node displacements on the direction parallel to the paddle (Oy axis).

To assess the patient comfort during compression, the resulting internal stress and strain distributions, as well as the contact pressure maps were derived. These data were collected at compressive forces of 22 N for the first volunteer (Figure 5.12) and 95 N for the second one (Figure 5.13).

Regarding the smallest breast volume (Figure 5.12), there is no significant difference between FPM and RPM in pressure distribution over the skin surface or in internal stress/strain intensity distributions. For both compression paddles, high pressure at the skin surface is concentrated in the juxtathoracic region with a maximum pressure of 77.7 kPa. In addition, the FE simulations confirm that in small breasts the paddle tilt is too small to impact the tissues compression in the middle part of the breast. FPM applied on larger breast volumes (Figure 5.13) results in significantly lower intensities of pressure at the skin surface in contact with the compression paddle, with a maximal pressure of 37 kPa, compared to 56 kPa when using RPM. No significant difference in the measured maximal intensities of strain and stress was observed, however strain and stress distribution patterns are different. When the breast is compressed with a rigid paddle, maximal strain and stress are concentrated in the retromammary space and decrease considerably toward the nipple. When a flex paddle is used, stress and strain are more uniformly distributed over the breast volume with the highest values in the middle third of the breast.

The area pressure distribution patterns have already been demonstrated in the work by Dustler M. et al. [38]. The authors have studied the pressure distribution patterns of 103 women undergoing breast compression with a rigid paddle at different compression levels. Four groups were differentiated: a) skin pressure widespread over the breast (29%); b) skin pressure concentrated on the central part of the breast (8%); c) skin pressure concentrated on the juxtathoracic region (16%); d) skin pressure concentrated along a narrow zone at the juxtathoracic region (26%). The pressure distribution patterns observed for our first and second volunteers correspond to the group d) and a) respectively.

**CHAPTER 5. BREAST COMPRESSION & COMFORT**  
**A COMPARATIVE STUDY**

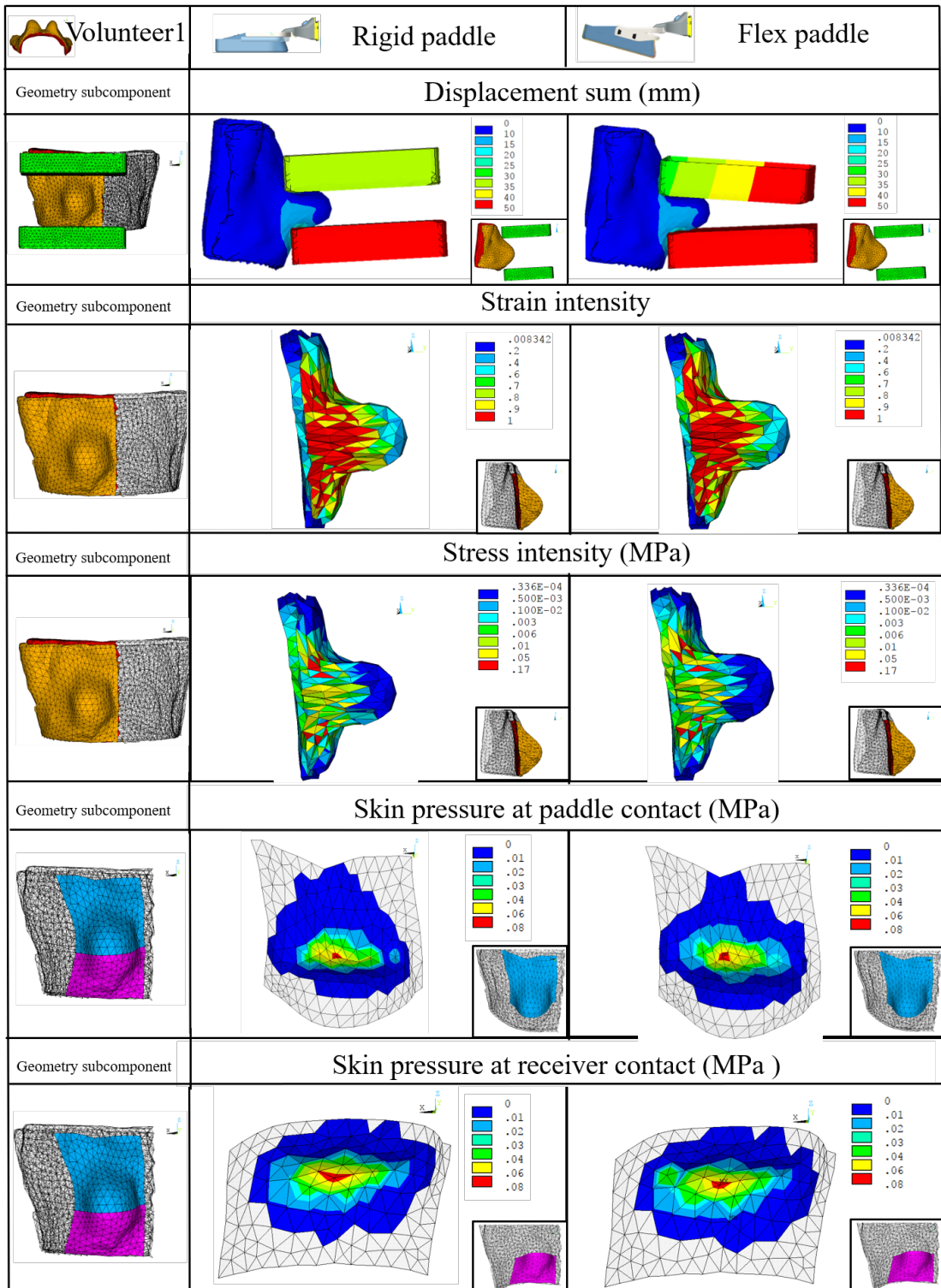


Figure 5.12: Stress, strain and contact pressure distribution for the first volunteer

*CHAPTER 5. BREAST COMPRESSION & COMFORT  
A COMPARATIVE STUDY*

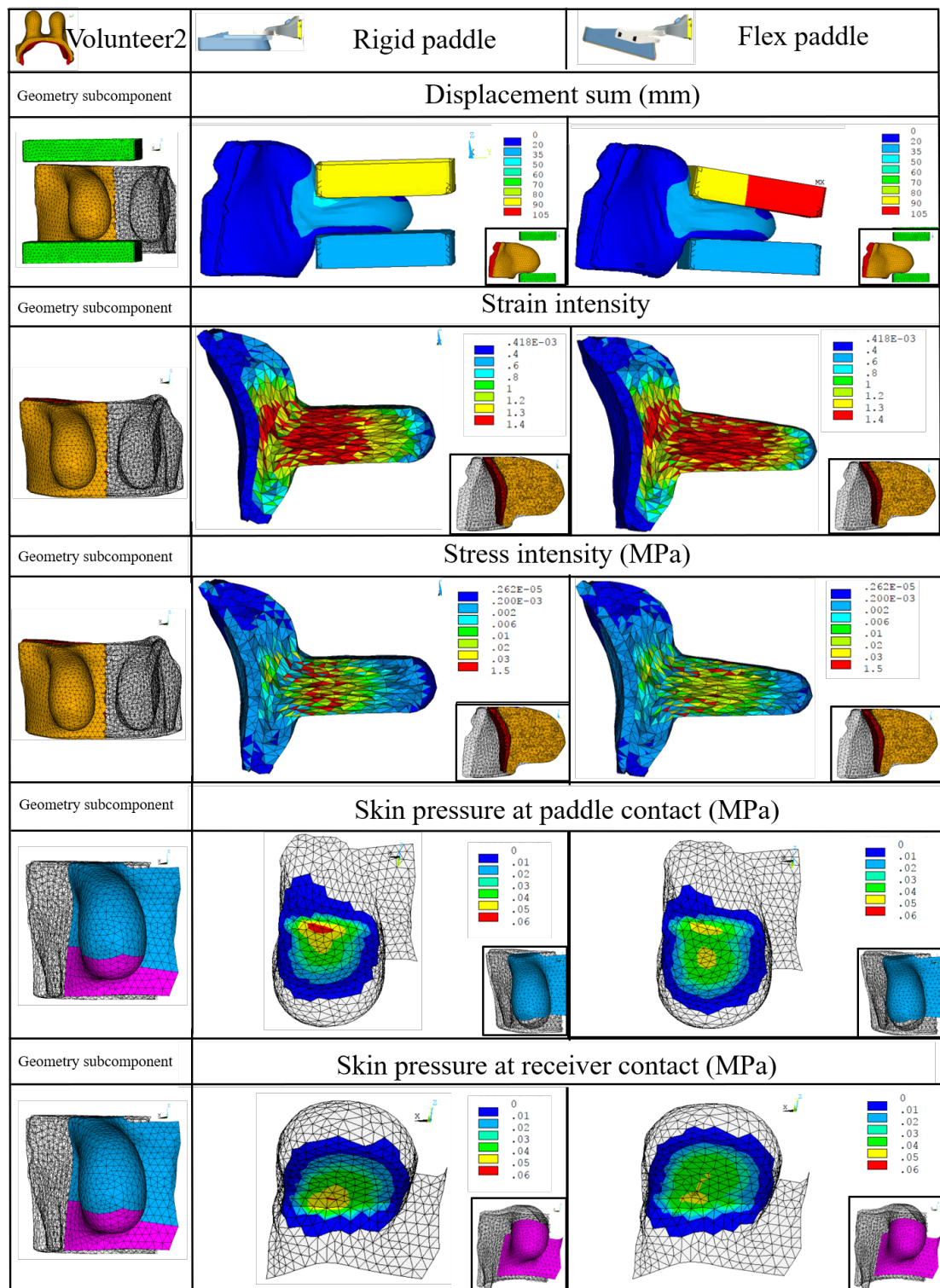


Figure 5.13: Stress, strain and contact pressure distribution for the second volunteer

### 5.4.2 Paddle positioning impact on compression mechanics

A second study was performed in order to assess the paddle positioning impact on the compression force. The simulations were performed only on the right breast of the second volunteer. Indeed, the geometry of the first volunteer is too small and does not meet the necessary morphological criteria required by this study.

Using the rigid paddle model to perform compressions with different paddle position in respect to the thoracic cage (thoracic cage to paddle distance TPD, Figure 5.15) has generated large convergence problems. For example, when the paddle was positioned closer to the chest wall, the finite elements were distorted because of high contact pressure at the juxtathoracic are. Therefore, for further investigations, the elastic paddle model was used. This model is closer to the mechanical properties of the standard rigid paddle from a mammography unit. In addition, material elasticity allows a slight paddle bending which seems to reduce elements' distortions.

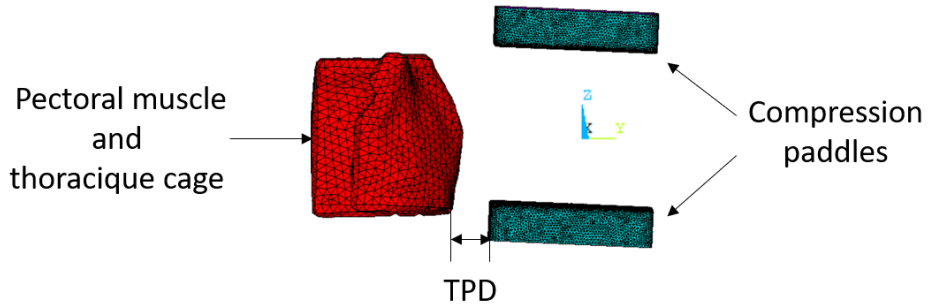


Figure 5.14: Thoracic cage to paddle distance (TPD).

The breast was compressed until a minimal thickness of 50mm was reached. Then, the compression force as well as surface pressure at the contact with the compression paddle were compared. The compression force was computed as the product between the mean surface pressure and the contact area  $\langle P_{contact} \rangle * A_{contact}$ .

Figure 5.15 shows the strain/stress as well as the pressure distributions over the contact area for three distinct distances TPD between the paddle and the thoracic cage. The compression force varies considerably within paddle positions. A compression force of 59 N, 94 N and 158 N was obtained when the paddle was positioned at a distance from the chest wall of 48 mm, 40 mm and 33 mm respectively. Positioning the paddle with 15 mm closer to the chest wall tripled the force intensity.

Due to the paddle elasticity, the breast thickness slightly varies, with a maximal deflection equal to 3.5 mm (Figure 5.15 first line). A very small difference between the maximal paddle deflection ( $\sim 1$  mm) was observed within the previous three compressions. Thus, image quality or AGD were not significantly impacted by the breast thickness variation. However, the wider the space between the chest wall and the compression paddle, the fewer breast tissues in the projected mammography image. In a standard framework, the

*CHAPTER 5. BREAST COMPRESSION & COMFORT  
A COMPARATIVE STUDY*

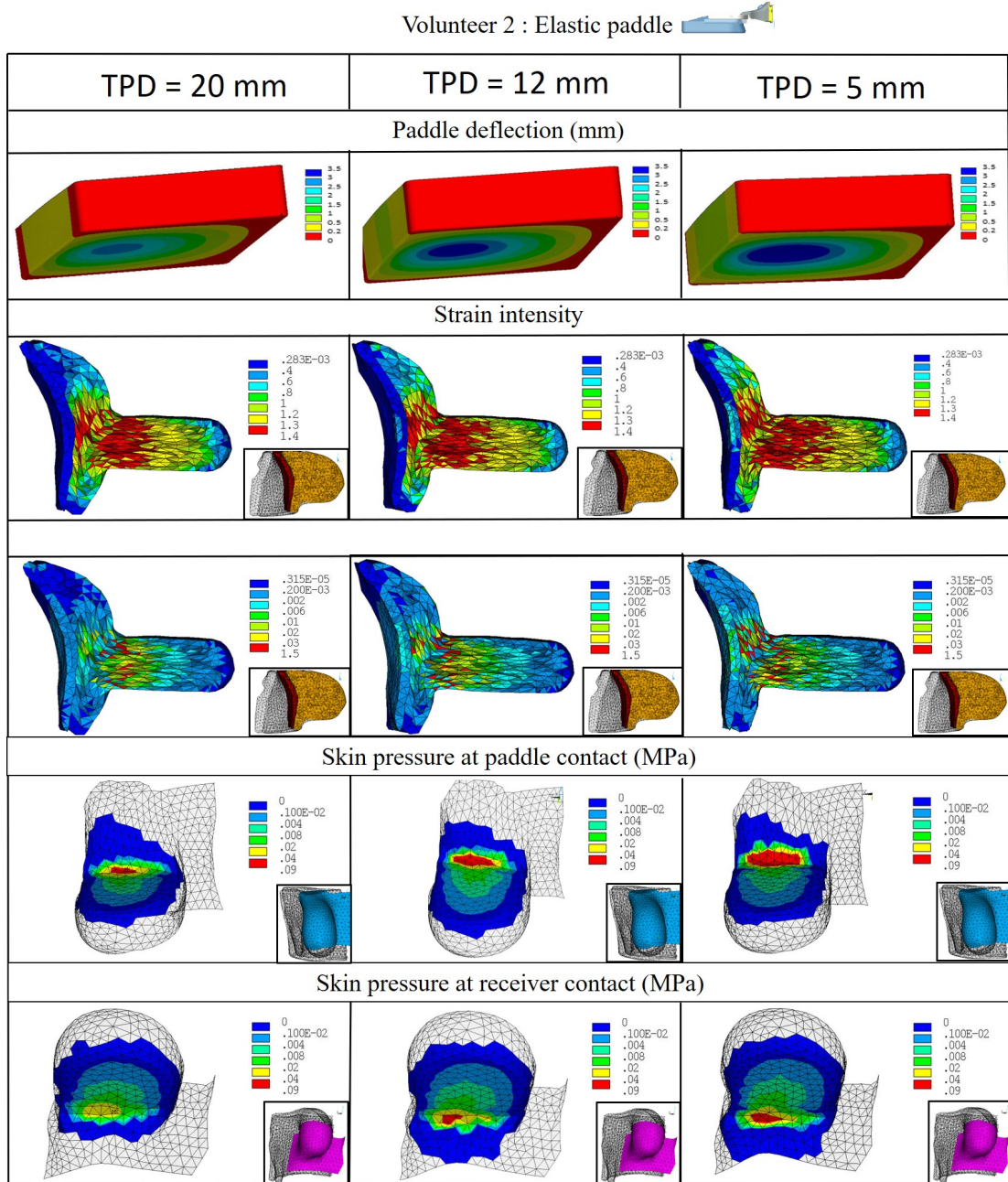


Figure 5.15: Stress, strain and contact pressure distribution for a variable thoracic cage to paddle distance (TPD).

technologist will include as much breast tissues as possible in order to reduce the risk of missing a suspicious lesion.

When looking at the strain distribution, one can see that, when the compression paddle is positioned closer to the chest wall, the juxtathoracic soft tissue undergoes higher deformation resulting also in a higher stress intensity. Concerning the skin surface pressure dis-

tribution, the highest intensities ( $\sim 90 \text{ kPa}$ ) are always concentrated in the juxtathoracic area. However, for a thorax to paddle distance equal to  $33 \text{ mm}$ , the area corresponding to the high pressure is considerably larger. This means that a significant part of the total force was used to compress the tissues in the juxtathoracic area only, which may increase the patient discomfort.

## 5.5 Discussion and conclusion

In this chapter, the breast compression was simulated using three paddles models, the rigid, flex and elastic models. In order to comply with the compression mechanics as described in literature, an update of the tissues constitutive models was needed. Applying the Gent form of strain-energy potential, instead of the Neo-Hookean form, allowed to obtain compression force magnitudes comparable with the real subject data. However, when the same law is used to perform the multi-loading gravity simulations, the breast deformations in supine and prone configurations are over-constrained. We found that, with a larger value of  $J_m$  parameter, the Gent model may improve the breast geometry estimates obtained with a Neo-Hookean model. In conclusion, the estimated value of  $J_m$  does not characterize the subject-specific mechanical properties and gives only an estimation of a standard behaviour. Our second study shows that, to obtain a proper estimation of parameter  $J_m$ , more information like the paddle position with respect to the breast volume is needed.

The patient comfort (measured as strain and stress) as well as the image quality (measured as SNR, SDNR) and AGD were compared for breast compression with rigid and flex paddles. The results from the two volunteers were analysed. The compression simulations indicate that, for the smallest breast, there is no significant difference for the patient perceived pain when using the rigid or the flex paddles. We did not observe any statistically significant difference in SNR or SDNR for microcalcification of any size. Therefore, our results suggest that using a flex paddle should not significantly impact image quality and delivered dose in small breasts and should not reduce significantly the perceived pain. For the largest breast, our simulations indicate that using a flex paddle may reduce the maximal pressure intensity on the skin surface by about 30% compared to the rigid paddle. The tissues deformation is more uniformly distributed inside the breast volume, and the highest deformation occurs in the middle breast region corresponding to the supposed location of dense tissues. Moreover, our simulations have shown that the flex paddle has no significant impact on the average glandular dose and improves image quality compared to the rigid paddle. However, breast compression with a flex paddle is suspected to facilitate the displacement of the fibroglandular tissues into the retromammary area. As the breast thickness increases linearly from the nipple to the chest wall, the retromammary area is characterized by a low image quality.

The impact of paddle positioning on patient comfort and image quality was also addressed. Three paddle positions with respect to the chest wall were studied using the elastic compression paddle. Even if a variable breast thickness is obtained due to the paddles de-

*CHAPTER 5. BREAST COMPRESSION & COMFORT*  
*A COMPARATIVE STUDY*

---

flection, the variations are too small ( $\sim 1mm$ ) to impact the AGD or the resulting image quality in terms of the SNR or SDNR. However, by excluding the retromammary tissues from the imaged area, information on small posterior cancerous legions may be lost. In terms of patient comfort, the simulations have shown that the high pressure are always localized in the juxtathoracic areas. When the paddle is too close to the chest wall, the compression force is mostly dissipated on this narrow area resulting in very high pressures compared to the skin pressure over the breast ( $90kPa$  vs  $10kPa$ ).

# 6

## CONCLUSION AND PERSPECTIVES

The main aim of this PhD work was to develop a simulation framework capable of assessing breast compression as function of paddle design, compression force or breast positioning. Image quality, average glandular dose as well as patient comfort were considered when comparing different compression strategies.

A Monte-Carlo based simulation software was used to compute the X-ray propagation through matter and to generate simulated mammography images. The image quality was depending on the compressed breast thickness. The average glandular dose was computed using the method proposed by Dance D. et al. [31] requiring only the knowledge of compressed breast thickness and breast glandularity.

To assess the breast deformations depending on the paddle design or the applied compression force a new biomechanical breast model was developed. After being evaluated by confrontation with real data collected through MR images, this model was used to predict the outer shape of the breast under compression as well as the patient comfort assumed to be associated to internal strain/stress intensity and distribution.

In this chapter, the main results and conclusions on the implemented application are recalled. The possible improvements for a large prospect of applications are discussed.

## 6.1 Biomechanical breast model

Before modeling the mammography breast compression, the model fidelity to real tissues deformations had to be assessed. In this scope, data sets describing in-vivo breast mechanics were collected. The MRI is an interesting imaging modality allowing the extraction of the whole 3D breast geometry with the distribution of each internal structure. Therefore, MR images of two volunteers in three body positions (prone, supine and supine tilted) were acquired and used in this study. The two volunteers were chosen such that two different breast sizes were represented, small volume (breast cup A) and large volume (breast cup F). The boundary conditions describing breast deformation under gravity loading are easy to reproduce in a simulation framework. Thus, the acquired data made possible the calibration and the evaluation of the biomechanical model.

The development of the biomechanical breast model was performed using the small breast volume (first volunteer). As a small breast volume undergoes smaller deformations under gravity loading, the corresponding breast model was suspected to lead to less convergence difficulties. To this end, the MRI volume of the breast in supine position was used to build the finite element mesh. Then, combined with the MRI breast volume in prone body position, it was used to estimate the subject-specific constitutive parameters and the corresponding stress-free geometry.

From this first simulation, the importance of considering the sliding boundary conditions at the juncture surface between the pectoral muscle and the breast was pointed out. Indeed, the displacements driven by only tissues' elasticity were not enough to reflect the geometrical changes between the supine and prone breast configurations. Therefore, breast tissues were allowed to slide over the pectoral muscle surface. Additional boundary conditions were considered by modeling the breast suspensory ligaments and fascial system. Including stiffer structures into the finite element model improved solution convergence capabilities. These new structures allowed breast deformations for a larger range of soft tissue constitutive parameters.

According to the literature, a well defined breast model has to consider in-vivo measured constitutive parameters. To this end, the tissues Young's moduli giving the best fit between the simulated and measured breast configurations of the first volunteer were computed. The optimal estimates, assuming Neo-Hookean material models, were found to be  $\lambda_{breast}^r = 0.3 \text{ kPa}$ ,  $\lambda_{breast}^l = 0.2 \text{ kPa}$ ,  $\lambda_{skin} = 4 \text{ kPa}$  and  $\lambda_{fascia} = 120 \text{ kPa}$ . The obtained mechanical properties are comparable to the ones proposed in the literature when considering only the breast models with similar simulation frameworks [118, 52, 62]. This result allowed to compute the breast geometry in supine and prone configurations with an accuracy of  $1.70 \text{ mm}$  and  $2.17 \text{ mm}$  respectively. The model fidelity to the global breast deformation was evaluated using the breast geometry in supine tilted position. The Hausdorff distance between the breast skin surface extracted from the MRI volume and the simulated skin surface was equal to  $6.14 \text{ mm}$ . The larger error ( $\sim 26.03 \text{ mm}$ ) was obtained on the left breast where the lateral displacements of the tissues were overestimated due to large strains observed over the fascia and skin surfaces.

These results may be improved by developing a more complex breast support matrix or considering region dependent stiffness for the skin or the fascia system. Adding stiffer materials in the strategically localized areas on the contact surface may limit the fascia deformations under a large strain range. Therefore, the sliding of breast tissues in supine tilted configuration may be reduced.

The similarity between the estimated and measured breast configurations is assessed by computing the minimal distance from the estimated position of each skin node to the measured breast other shape. Using only surface measurements dose not entirely describe how both the skin surface and the internal tissues deform. During the MRI acquisitions, both volunteers were asked to fix six fiducial landmarks over the breast surface. Moreover, even if very difficult, one can envisage to identify internal anatomical landmarks defined by singular structures within breast volume. These landmarks' location brings new information on the internal tissue deformations. In a future work, considering such information as additional constraints in the calibration process may improve the breast geometry estimates. Moreover, including the distance between landmarks location in the measured and estimated configurations will also allow a better evaluation of the model accuracy .

The breast biomechanical model was then built up for the larger breast volume (second volunteer). However, because of a lack of time, the model optimization process was not performed for this volunteer. In future work, it would be interesting to perform such model optimization and evaluation on at least two more subjects with different breast morphologies and mechanical properties. The model calibration on a larger population should improve its flexibility for further studies on breast compression techniques.

Despite providing good results in the multi-loading gravity framework, the developed breast model turned out to be less efficient in simulating breast compression. With this model, the maximal force needed to simulate breast flattening was estimated to be relatively low when compared to the mean recommended force of a typical mammography exam (10N vs 120N). These low values of the compression force were due to tissue's abnormal softening under large stress rates. Tissue relaxation from a given stress threshold is a well known phenomenon when using Neo-Hookean materials. We therefore suggested to overcome this issue by replacing the Neo-Hookean model by a Gent model for all involved hyperelastic tissues.

The stress-strain relation almost remains almost the same for both models below a strain threshold defined by the parameter  $J_m$ . Beyond this threshold the Gent material model is stiffening exponentially resulting in an asymptotic behavior. These properties allow to change the tissues mechanical response only for large strain rates, as during breast compression. On the other hand, they also allow to preserve the same mechanical response for relatively small strains as induced by gravity loading simulations.

The breast compression simulations were performed using both breast volumes. As the tissues constitutive parameters of the second volunteer were not optimized, the values proposed by others similar works were used. Therefore, the second breast model does not describe the subject-specific mechanical behavior. However, it provides a new realistic model that may be used to assess the compression quality of different compression types.

The Gent material model improved the tissues mechanical response when the breast is compressed between the paddle and the image receiver. A compression force of 22 N for the first volunteer and 95 N for the second volunteer was obtained which fits well the measured clinical data (21.9 N and 94.8 N respectively).

Based on the same constitutive parameters, as estimated during breast compression, the Gent tissues model was used to estimate breast deformation under gravity loading for the first volunteer. We found that, with such a model, tissues displacements were over-constrained in both supine and prone configurations. However, we proved that the Gent model may also improve the biomechanical model fidelity to the real deformations under gravity loading. Therefore we suggested to use two different values of the parameter  $J_m$  in order to obtain the best estimates for multi-loading gravity and breast compression simulations. A more detailed study has then to be considered in order to estimate a unique tissues constitutive model. To this end, more data describing the compression breast process, such as breast position with respect to paddle, is needed. The impact of using different constitutive parameters within tissues types should also be studied. However, increasing the number of model parameters might increase the complexity of the optimization problem, as well as the computation time and the size of the data set describing the subject breast mechanics.

In this work, we have assumed that the breast mechanics does not depend on the glandular tissues distribution. This assumption is only valid if a global breast deformation is assessed, such as the breast surface deformation. However, when one wants to estimate the breast internal tissues displacements under compression or gravity loading, a more subtle definition of tissues materials is needed. In such a case, the differentiation of the glandular and adipose tissues should be more relevant.

During the modeling process, it has been observed that the breast tissues undergo extremely large deformations (up to 150%). This involves large convergence difficulties due to bad element formulations during simulations. To improve the solution convergence capabilities an hexahedral adaptive mesh might be considered.

In conclusion, the proposed biomechanical model was able to provide a good estimation of breast deformation under different boundary conditions. The models based on breast geometries of two subjects were used to perform comparative studies between various compression methods.

## **6.2 Breast compression and patient comfort**

The developed biomechanical breast model together with the image simulation framework were used to assess the clinical compression quality whithin different compression strategies.

A first study was performed to compare the breast compression quality when using standard rigid or flex paddles. To compute breast compressions, the proposed biomechanical model was calibrated for two breast volumes (small and large) with various mechanical properties (soft and firm). The results showed that, using the flex paddle may improve the patient comfort without affecting the image quality and the delivered average glandular

---

## CHAPTER 6. CONCLUSION AND PERSPECTIVES

---

dose. Moreover, despite a breast thickness varying linearly from chest wall to nipple, the image quality seems to be preserved or even improved compared to the image quality obtained with a rigid compression paddle. Such a better image quality obtained when using the flex paddle could be explained by a better overall breast compression. The paddle tilt allows a better compression of the tissues close to the nipple, relaxing the tissues located in the chest wall region. Our simulations tend to confirm that the paddle tilt may displace breast tissues towards the chest wall. The tissues accumulation on the retromammary space may hide clinical relevant information and thus increase the false negatives rates.

A second study was performed to assess the impact of breast positioning on breast compression mechanics. This time, the paddle deflection due to its material elastic properties was considered to enable solution convergence when the compression paddle is close to the chest wall. Three breast compression simulations were performed with various distances between the paddle and the chest wall. In this context, only the larger breast volume was used, the smaller volume being not adapted to such a simulation. The results showed that patient comfort can be improved by positioning the paddles further from the pectoral muscle. For an equivalent breast thickness under compression, the compression force decreased from  $158\text{ N}$  to  $59\text{ N}$  for a difference of  $15\text{ mm}$  in the distance from chest wall to paddle. On the other hand, clinical guidelines request to place the paddle as close as possible to the chest wall. Therefore, our simulations show that one may have to find a compromise between the exam quality and the patient comfort.

These two preliminary studies have shown that the clinical compression quality can be assessed using such simulation frameworks. The tools designed during this PhD thesis may be used to perform wider studies on existing breast compression systems, but also to provide a first estimation of the performance of a new, not yet implemented, paddle design. Simulation based studies are less expensive in time and materials than the usual clinical studies, therefore they may be used to discharge the less relevant paddle models.

*CHAPTER 6. CONCLUSION AND PERSPECTIVES*

---

## KEY CONTRIBUTIONS

The key contributions concerning the finite element breast modeling are the following:

- We introduced new boundary conditions which reflect the motion of the breast over the thoracic cage. They included sliding contact surface based on Coulombs friction law combined with stiff support structures. To our knowledge, the breast support matrix was considered for the first time into the finite element model. The generic model includes suspensory ligaments together with the fascial system, and was built based on their anatomical description.
- The iterative algorithms allowing to estimate the breast stress-free geometry are generally using only one breast configuration (supine or prone breast configuration). In this work we proposed an optimization algorithm which estimate the breast stress-free geometry starting from supine configuration and then iteratively correct it based on the prone configuration.
- We disposed of a data set of breast MR images in three different body positions of the same volunteer. Therefore, our biomechanical breast model was first calibrated using prone and supine configurations. Then, its mechanical response was evaluated on a third breast configuration (supine tilted). Because of a lack of reliable data, none of previously published biomechanical breast models was evaluated in such wide panel of deformations.
- We evaluated the capability of the proposed biomechanical breast model to reproduce the breast compression mechanics as described by several clinical studies. This analysis allowed us to point out the limitations of the Neo-Hookean strain energy function when modeling such large deformations. Accordingly, a new material constitutive model defined by the Gent strain energy function was proposed.
- We developed a simulation framework allowing to quantify breast compression in terms of image quality, average glandular dose and patient comfort. Due to its mod-

## KEY CONTRIBUTIONS

---

ularity, framework supports different paddle designs and different breast geometries and compositions.

Using previously described tools, two studies assessing the breast compression quality were performed, demonstrating:

- The difference of the compression quality in terms of patient comfort, image quality and average glandular dose between a standard rigid and flex paddles was quantified. We have showed that, for the small breast, there was no difference in patient experience or image quality between the two paddles. However, using the flex paddle to compress the larger breast, may improve the patient experience without affecting the image quality or the average glandular dose.
- The impact of breast positioning on the compression mechanics and patient comfort was analyzed. The obtained results have proved that the breast positioning have a significant impact on patient comfort. The surface pressure in the juxtathoracic area increased when the paddle was positioned closer to the chest wall.

A list of publications resuming the results of this work is provided below.

## PUBLICATIONS

Mîra, A., Payan, Y., Carton, A. K., de Carvalho, P. M., Li, Z., Devauges, V., & Muller, S. (2018, March). Simulation of breast compression using a new biomechanical model. *In Medical Imaging 2018:Physics of Medical Imaging* (Vol. 10573, p. 105735A). International Society for Optics and Photonics.

Mîra A., Carton A.K., Muller S. & Payan Y. (2018). Breast biomechanical modeling for compression optimization in digital breast tomosynthesis. *Computer Methods in Biomechanics and Biomedical Engineering*, Lecture Notes in Bioengineering, A. Gefen and D. Weihs editors, pp. 29-35, DOI 10.1007/978 – 3 – 319 – 59764 – 5\_4

Mîra A., Carton A.K., Muller S. & Payan Y. (2016). Breast biomechanical modeling for compression optimization in digital breast tomosynthesis. *Proceedings of the 22nd Congress of the European Society of Biomechanics (ESB2016)*

## PUBLICATIONS

---

# Appendices





## DISTANCE MEASURES

For the sake of simplicity, only the distance between discrete 3D-surfaces represented by triangular meshes will be defined. A discrete 3D-surface is usually represented by a set of points  $S = \{p_1, p_2, \dots, p_n\}$  in  $\mathbb{R}^3$  (vertices), and by a set  $\mathcal{T}$  of triangles describing how the vertices from  $S$  are linked together. Thus, the similarity between two surfaces is measured by computing distances between the respective point sets. Let define a point  $p$  belonging to the surface  $S$ , and a point  $q$  belonging to the surface  $S'$ .

### Euclidean distance between two points

The Euclidian distance is defined as the shortest possible path through space between two points (also named the  $L^2 - norm$ ) and is defined as:

$$D(p, q) = \|p - q\|_2 = (\|p_x - q_x\|^2 + \|p_y - q_y\|^2 + \|p_z - q_z\|^2)^{\frac{1}{2}} \quad (\text{A.1})$$

### Node to surface distance

The distance  $D'(p, S')$  from the point  $p$  to the surface  $S'$  is defined as

$$D'(p, S') = \min_{q \in S'} \|p - q\|_2 \quad (\text{A.2})$$

### Minimal distance between two surfaces

The minimal distance between two surfaces  $S$  and  $S'$  is defined as

$$D'_{min}(S, S') = \min_{p \in S} \{D'(p, S')\} \quad (\text{A.3})$$

### Maximal distance between two surfaces

The maximal distance between two surfaces  $S$  and  $S'$  is defined as

$$D'_{max}(S, S') = \max_{p \in S} \{D'(p, S')\} \quad (\text{A.4})$$

---

## APPENDIX A. DISTANCE MEASURES

---

### Mean distance between two surfaces

The mean distance between two surfaces  $S$  and  $S'$  is defined as

$$D'_{mean}(S, S') = \frac{1}{|S|} \sum_{p \in S} D'(p, S') \quad (\text{A.5})$$

where  $|S|$  is the number of nodes belonging to the surface  $S$ .

### Hausdorff distance between two surfaces

The Hausdorff distance [75] between two surfaces is defined as

$$H(S, S') = \max\{D'_{max}(S, S'), D'_{max}(S', S)\} \quad (\text{A.6})$$

### Modified Hausdorff distance between two surfaces

The modified Hausdorff distance between two surfaces is defined as

$$H'(S, S') = \max\{D'_{mean}(S, S'), D'_{mean}(S', S)\} \quad (\text{A.7})$$

Dubuisson and Jain [36] have studied 24 measures to assess the similarities between two discrete surface meshes. According to the authors, the Hausdorff distance has the best performance for object matching.

# B

## MESH CONVERGENCE

In finite element modeling, a finer mesh usually results in a more accurate solution. However, as a mesh is made finer, the computation time increases. To get a mesh that satisfactorily balances accuracy and computing resources, a mesh convergence study has to be performed.

In this scope, the breast and muscle geometries were meshed with different mesh sizes; the minimal elements sizes was set to  $7\text{mm}$  and the maximal element size was varied to  $\{7\text{mm}, 10\text{mm}, 13\text{mm}, 15\text{mm}, 17\text{mm}, 20\text{mm}\}$ . Simulation with a mesh size of  $5\text{mm}$  was not supported as it become too expensive in computation time and memory therefore a computer with higher computational power was needed. The compression paddle geometries were meshed with a constant element size of  $1\text{mm}$ . The number of elements obtained for each mesh size is given in Table B.1. We can see that, in general, larger the mesh size, lower the number of elements. However, we observed that for a mesh size equal to  $17\text{ mm}$ , a higher number of elements was obtained when compared to a mesh size of  $15\text{mm}$ . This is due to the fact that the mesh size being defined by the maximal and minimal elements size, a higher number of *small* elements is needed to cover the areas smaller than the *large* elements. With such meshes, the element density is usually concentrated on the corners or narrow spaces which, in our case, do not coincide with the region of interest.

Mesh size	20mm	17mm	15mm	13mm	10mm	7mm
Nb. of elements	8367	10897	8099	10751	18453	65785

Table B.1: Number of elements obtained for each mesh size.

Our model was developed to compute breast deformation under compression, an equivalent simulation was performed to estimate the optimal mesh size. Starting from the breast supine geometry, the gravity was applied in the posterio-anterior direction. Then, the right breast was compressed between the breast support and the paddle (Figure B.1). In this work we are interested in tissue deformations, therefore the strain range for each mesh density was analysed. The strain distribution over the breast volume for each mesh

## APPENDIX B. MESH CONVERGENCE

---

size are given in Figure B.1.

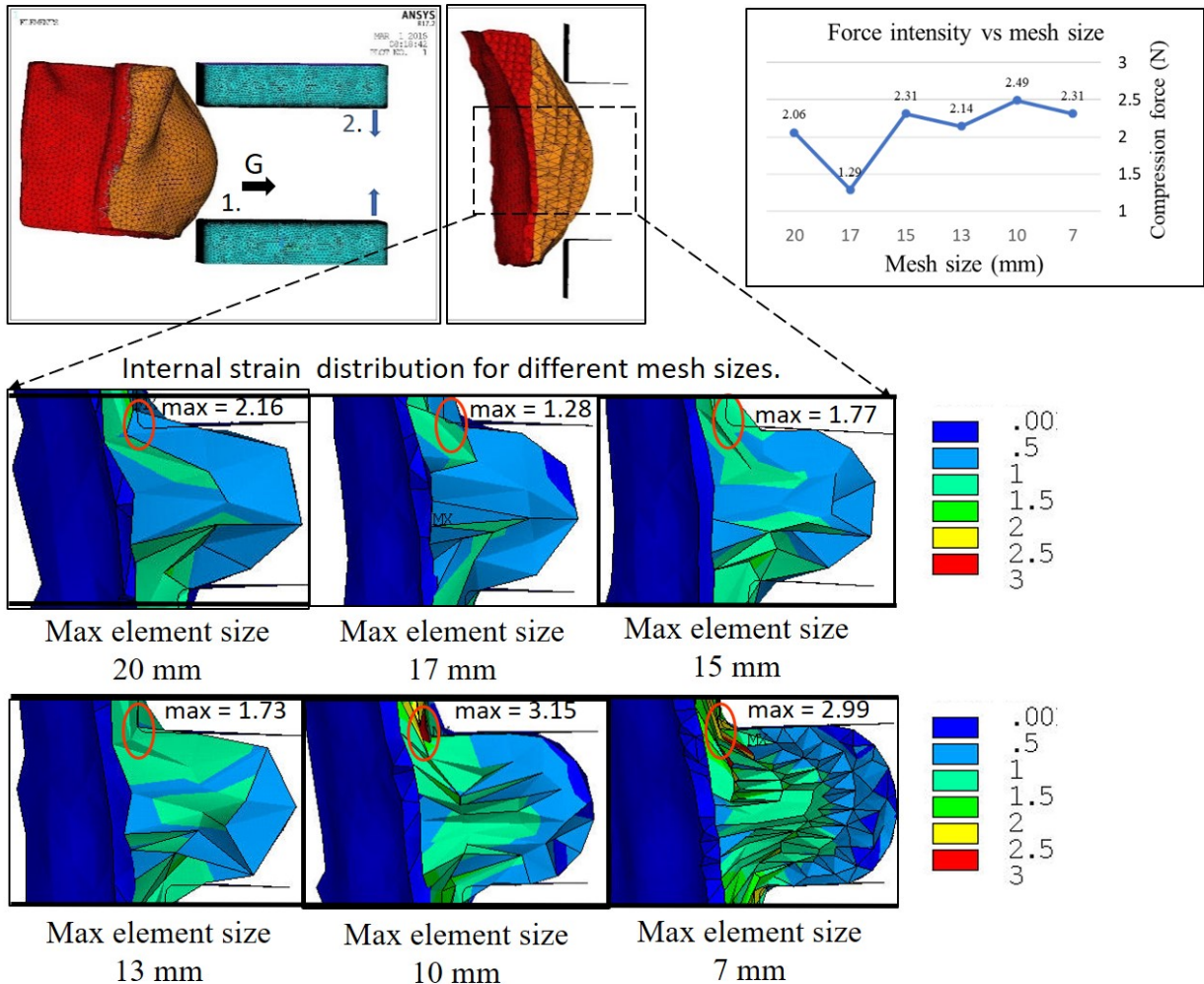


Figure B.1: Internal strain distribution in function of the elements size.

Under compression, the maximal strain is expected to occur in the juxtathoracic area at the contact with the paddle corner (marked area with an orange ellipsoid in Figure B.1), therefore the maximal strain was measured in this region for each mesh density. However, the observed values did not show a converging behavior within different mesh sizes. To analyze the mesh convergence, the applied force for a target compressed breast thickness was plotted (Figure B.1). One can see that the force intensity converges starting with a mesh size equal to 15mm. However, a visual analysis of the strain distributions over the breast volume shows that using a mesh size equal to or lower than 10 mm results in a better estimation of the internal strain distribution. Therefore, to optimize the computation time, a mesh size equal to 10mm is used.

# C

## BONDARY CONDITIONS *contact models*

The proposed biomechanical model consists of two bodies, one representing the pectoral cage with the pectoral muscle, and the second representing the breast soft tissue. Between the two bodies, a contact surface is defined in order to model tissues mechanics at the juncture interface.

The next section describes the implementation of different interaction models tested during the model development process. Since the breast tissues are always attached to the pectoral muscle (Figure C.1), the contact surface was modeled using *bonded* and *no-separation frictional* interaction model only.

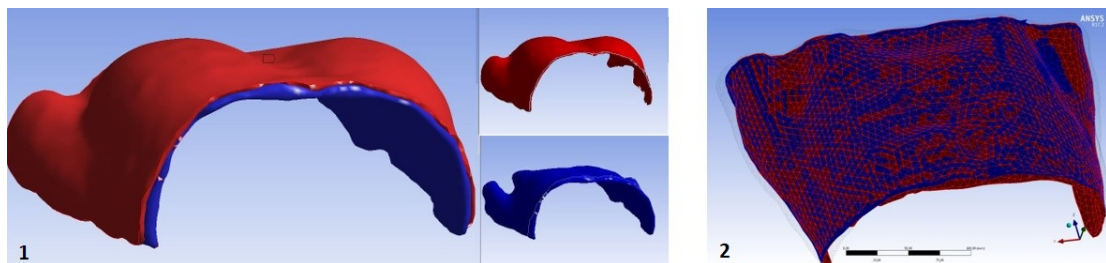


Figure C.1: The two bodies representing the thoracic cage and breast (1) with their the associated contact surface (2). Blue surface - muscle representing the target surface, red surface - breast representing contact surface

The results for pure bonded and pure no-separation sliding models, as well as one combined contact surface, are listed bellow. For some contact models, because of large instabilities or a poor fidelity to the real breast mechanics, only partial results are presented.

## APPENDIX C. BONDARY CONDITIONS CONTACT MODELS

---

### Bonded contact surface

First, a pure bounded contact was used to model the interaction between the breast and the pectoral muscle. To achieve realistic breast deformation, extremely low values of equivalent Young's modulus and Poisson ratio were needed ( $\lambda_{breast} = 0.3 \text{ kPa}$  and  $\nu_{breast} = 0.45$ ). An example of breast deformation in prone and supine configuration is illustrated in Figure C.2.

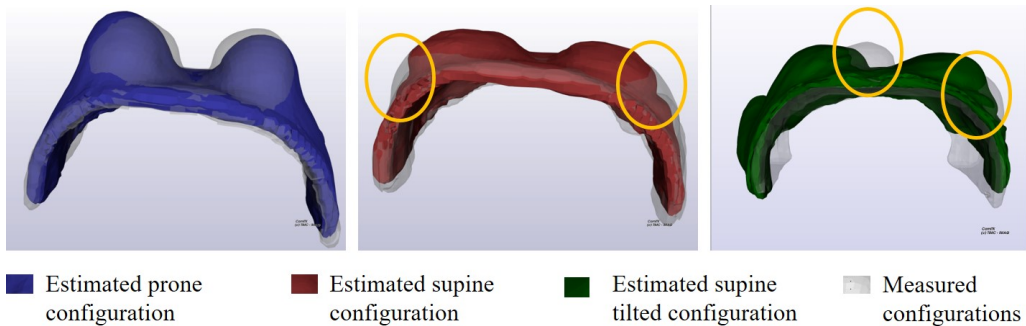


Figure C.2: Resulting breast deformation with a bonded contact model.

One can see that, even if the breast geometry in prone position is well estimated, the one in supine and supine tilted configurations are constrained laterally. Moreover, an important volume variation was observed which is not a characteristic of breast changes under gravity loading. The volume variation is due to a too low value of the Poisson ratio.

### Sliding contact surface

Pure sliding contact surface was considered in order to allow larger tissues displacements on lateral direction. The breast sliding over the muscle surface was modeled using the Coulomb friction law (Section 2.3.2). Additional boundary conditions were set by imposing zero-displacement on the right, left, superior and inferior mesh boundaries representing the breast volume (see Figure 3.11 for a recall on different mesh boundaries). This model caused large convergence problems because of breast tissues over-sliding. It was obvious that the model needs more boundary conditions in order to achieve convergence. Moreover, a non-linear and a non-uniform sliding model was needed in order imitate the behavior of rich fibrous areas where the breast is attached to the chest wall (see Section 1.1.3 for a recall on breast anatomy).

### Mixt contact surface

In order to limit breast tissues sliding, a mixt contact surface was defined. Herein, the contact surface consists of two complementary areas (Figure C.3), the first one modeled as bonded contact and the second one modeled as no-separation sliding contact. The regions corresponding to the bounded contact are defined following the anatomical structures where the concentration of fibrous tissues is significantly higher. Such regions are encountered

along the muscle surface where the superficial muscle fascia meets the breast suspensory ligaments, as it is the case for the inframammary ligament, the deep medial ligament or the deep lateral ligament.

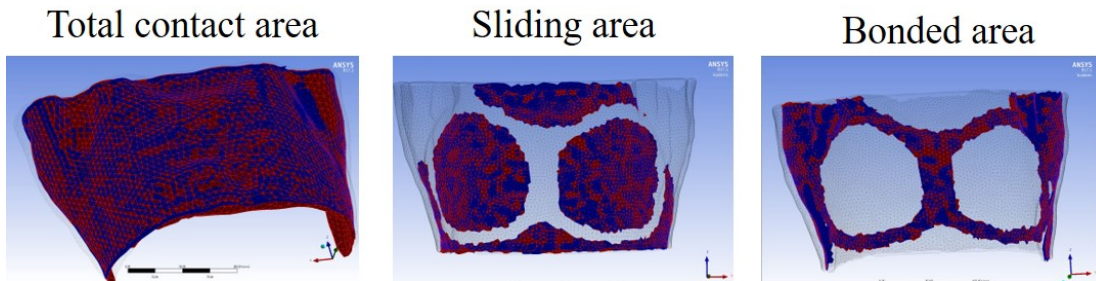


Figure C.3: The contact surface divided in two regions: sliding region and bonded region.

Using such a contact model improves substantially the estimate of the supine breast configuration. However, because of a high deformation gradient imposed at the juncture border between the two contact areas, convergence problems were observed. Moreover, when the supine configuration is estimated, several folds are created at the skin surface (Figure C.4). The same types of folds were obtained in supine tilted configuration creating large convergence problems because of tissues superposition.

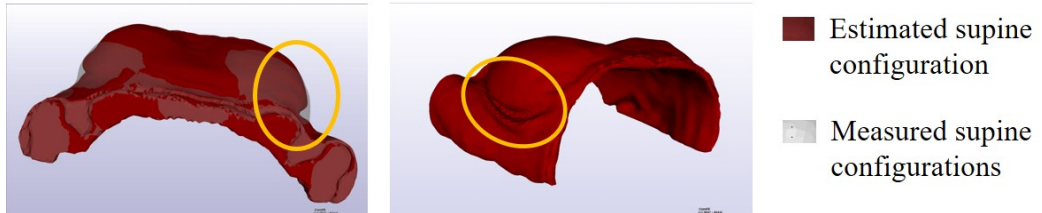


Figure C.4: The contact surface divided in two regions: sliding region and bonded region.

This last described model has provided satisfactory results, however it led to important solution convergence problems. Therefore, the model was improved by replacing the bonded contact regions with stiff ligaments connecting the breast tissues to the muscle. Contrary to the bonded contact, the ligaments preclude progressively the breast tissues from sliding and allow a slight displacements avoiding the creation of folds. Moreover, an additional layer modeling the deep layer of breast superficial fascia was added at the juncture surface between the breast and muscle. Knowing that the fascia is stiffer than the breast soft tissues, it controls the amount of sliding and facilitates the solution convergence. For more information on ligaments and fascia mechanical properties, see Section 3.4.



## BIBLIOGRAPHY

- [1] R. Abeyaratne. *Continuum Mechanics: Volume II of Lecture Notes on The Mechanics of Elastic Solids*. Cambridge MA and Singapore, 2012.
- [2] M. Abu-Hijleh, A. Roshier, Q. Al-Shboul, A. Dharap, and P. Harris. The membranous layer of superficial fascia: evidence for its widespread distribution in the body. *Surgical and Radiologic Anatomy*, 28(6):606–619, 2006.
- [3] ACS. American cancer society: Types of breast cancer. <https://www.cancer.org/cancer/breast-cancer/understanding-a-breast-cancer-diagnosis/types-of-breast-cancer.html>, 2017.
- [4] V. Andolina and S. Lillé. *Mammographic imaging: a practical guide*. Lippincott Williams & Wilkins, 2011.
- [5] F. J. Andrews. Pain during mammography: implications for breast screening programmes. *Journal of Medical Imaging and Radiation Oncology*, 45(2):113–117, 2001.
- [6] ANSYS. *ANSYS Contact Technology Guide*, 17 edition, 2017.
- [7] ANSYS. *Theory reference for the mechanical APDL and mechanical applications*, 17 edition, 2017.
- [8] A. R. Aro, P. Absetz-Ylöstalo, T. Eerola, M. Pamilo, and J. Lönnqvist. Pain and discomfort during mammography. *European Journal of Cancer*, 32(10):1674–1679, 1996.
- [9] A. R. Aro, H. J. De Koning, P. Absetz, and M. Schreck. Psychosocial predictors of first attendance for organised mammography screening. *Journal of Medical Screening*, 6(2):82–88, 1999.

## BIBLIOGRAPHY

---

- [10] L. K. Askhar and Y. H. Zaki. Female patients' perception of pain caused by mammography in the western region of saudi arabia. *Saudi medical journal*, 38(7):768, 2017.
- [11] F. S. Azar, D. N. Metaxas, and M. D. Schnall. Methods for modeling and predicting mechanical deformations of the breast under external perturbations. *Medical Image Analysis*, 6(1):1–27, 2002.
- [12] S. Bayati and B. R. Seckel. Inframammary crease ligament. *Plastic and reconstructive surgery*, 95(3):501–508, 1995.
- [13] T. Belytschko, W. K. Liu, B. Moran, and K. Elkhodary. *Nonlinear finite elements for continua and structures*. John wiley & sons, 2013.
- [14] J. M. Boone. Glandular breast dose for monoenergetic and high-energy x-ray beams: Monte carlo assessment. *Radiology*, 213(1):23–37, 1999.
- [15] M. J. Broeders, M. ten Voorde, W. J. Veldkamp, R. E. van Engen, C. van Lansveld-Verhoeven, M. NL't Jong-Gunneman, J. de Win, K. Droogh-de Greve, E. Paap, and G. J. den Heeten. Comparison of a flexible versus a rigid breast compression paddle: pain experience, projected breast area, radiation dose and technical image quality. *European radiology*, 25(3):821–829, 2015.
- [16] M. Bucki, C. Lobos, and Y. Payan. A fast and robust patient specific finite element mesh registration technique: application to 60 clinical cases. *Medical image analysis*, 14(3):303–317, 2010.
- [17] J. L. Calvo-Gallego, J. Martínez-Reina, and J. Domínguez. A polynomial hyperelastic model for the mixture of fat and glandular tissue in female breast. *International Journal for numerical methods in biomedical engineering*, 31(9), 2015.
- [18] *Determining material properties of the breast for image-guided surgery*. International Society for Optics and Photonics, 2009.
- [19] T. Carter, L. Han, Z. Taylor, C. Tanner, N. Beechy-Newman, S. Ourselin, and D. Hawkes. Application of biomechanical modelling to image-guided breast surgery. *Soft Tissue Biomechanical Modeling for Computer Assisted Surgery*, pages 71–94, 2012.
- [20] T. J. Carter. *Biomechanical modelling of the breast for image-guided surgery*. PhD thesis, University of London, 2009.
- [21] G. Catanuto, A. Spano, A. Pennati, E. Riggio, G. M. Farinella, G. Impoco, S. Spoto, G. Gallo, and M. B. Nava. Experimental methodology for digital breast shape analysis and objective surgical outcome evaluation. *Journal of Plastic, Reconstructive & Aesthetic Surgery*, 61(3):314–318, 2008.

- [22] G. Chagnon, G. Marckmann, and E. Verron. A comparison of the hart-smith model with arruda-boyce and gent formulations for rubber elasticity. *Rubber chemistry and technology*, 77(4):724–735, 2004.
- [23] H.-P. Chan, S. Galhotra, C. J. Vyborny, H. MacMahon, P. M. Jokich, et al. Image feature analysis and computer-aided diagnosis in digital radiography. i. automated detection of microcalcifications in mammography. *Medical physics*, 14(4):538–548, 1987.
- [24] B. Chen, Y. Wang, X. Sun, W. Guo, M. Zhao, G. Cui, L. Hu, P. Li, Y. Ren, J. Feng, et al. Analysis of patient dose in full field digital mammography. *European journal of radiology*, 81(5):868–872, 2012.
- [25] J. T.-M. Cheung, M. Zhang, and K.-N. An. Effects of plantar fascia stiffness on the biomechanical responses of the ankle–foot complex. *Clinical Biomechanics*, 19(8):839–846, 2004.
- [26] K. Chida, Y. Komatsu, M. Sai, A. Nakagami, T. Yamada, T. Yamashita, I. Mori, T. Ishibashi, S. Maruoka, and M. Zuguchi. Reduced compression mammography to reduce breast pain. *Clinical imaging*, 33(1):7–10, 2009.
- [27] J.-H. Chung, V. Rajagopal, P. M. Nielsen, and M. P. Nash. Modelling mammographic compression of the breast. In *Medical Image Computing and Computer-Assisted Intervention—MICCAI 2008*, pages 758–765. Springer, 2008.
- [28] D. R. Ciocca and M. A. Fanelli. Estrogen receptors and cell proliferation in breast cancer. *Trends in Endocrinology & Metabolism*, 8(8):313–321, 1997.
- [29] C. D. Clemente. *Anatomy: a regional atlas of the human body*. Wolters Kluwer/Lippincott Williams & Wilkins Health, 2011.
- [30] R. H. Conley, I. M. Meszoely, J. A. Weis, T. S. Pheiffer, L. R. Arlinghaus, T. E. Yankeelov, and M. I. Miga. Realization of a biomechanical model-assisted image guidance system for breast cancer surgery using supine mri. *International journal of computer assisted radiology and surgery*, 10(12):1985–1996, 2015.
- [31] D. Dance, C. Skinner, K. Young, J. Beckett, and C. Kotre. Additional factors for the estimation of mean glandular breast dose using the uk mammography dosimetry protocol. *Physics in medicine & biology*, 45(11):3225, 2000.
- [32] P. M. de Carvalho. *Low-Dose 3D Quantitative Vascular X-ray Imaging of the Breast*. PhD thesis, Université Paris Sud-Paris XI, 2014.
- [33] J. E. de Groot, M. J. Broeders, C. A. Grimborgen, and G. J. den Heeten. Pain-preventing strategies in mammography: an observational study of simultaneously recorded pain and breast mechanics throughout the entire breast compression cycle. *BMC women's health*, 15(1):26, 2015.

## BIBLIOGRAPHY

---

- [34] B. De Man, S. Basu, N. Chandra, B. Dunham, P. Edic, M. Iatrou, S. McOlash, P. Sainath, C. Shaughnessy, B. Tower, et al. Catsim: a new computer assisted tomography simulation environment. In *Medical Imaging 2007: Physics of Medical Imaging*, volume 6510, page 65102G. International Society for Optics and Photonics, 2007.
- [35] A. D. Domar, A. Eyvazzadeh, S. Allen, K. Roman, R. Wolf, J. Orav, N. Albright, and J. Baum. Relaxation techniques for reducing pain and anxiety during screening mammography. *American Journal of Roentgenology*, 184(2):445–447, 2005.
- [36] M.-P. Dubuisson and A. K. Jain. A modified hausdorff distance for object matching. In *Pattern Recognition, 1994. Vol. 1-Conference A: Computer Vision & Image Processing., Proceedings of the 12th IAPR International Conference on*, volume 1, pages 566–568. IEEE, 1994.
- [37] J. R. Dullum, E. C. Lewis, and J. A. Mayer. Rates and correlates of discomfort associated with mammography. *Radiology*, 214(2):547–552, 2000.
- [38] M. Dustler, I. Andersson, H. Brorson, P. Fröjd, S. Mattsson, A. Tingberg, S. Zackrisson, and D. Förnvik. Breast compression in mammography: pressure distribution patterns. *Acta Radiologica*, 53(9):973–980, 2012.
- [39] M. Dustler, I. Andersson, D. Förnvik, and A. Tingberg. The effect of breast positioning on breast compression in mammography: a pressure distribution perspective. In *Medical Imaging 2012: Physics of Medical Imaging*, volume 8313, page 83134M. International Society for Optics and Photonics, 2012.
- [40] M. Eder, S. Raith, J. Jalali, A. Volf, M. Settles, H.-G. Machens, and L. Kovacs. Comparison of Different Material Models to Simulate 3-D Breast Deformations Using Finite Element Analysis. *Annals of Biomedical Engineering*, 42(4):843–857, Apr. 2014.
- [41] B. Eiben, R. Lacher, V. Vavourakis, J. H. Hipwell, D. Stoyanov, N. R. Williams, J. Sabczynski, T. Bülow, D. Kutra, K. Meetz, et al. Breast conserving surgery outcome prediction: A patient-specific, integrated multi-modal imaging and mechano-biological modelling framework. In *International Workshop on Digital Mammography*, pages 274–281. Springer, 2016.
- [42] B. Eiben, V. Vavourakis, J. H. Hipwell, S. Kabus, T. Buelow, C. Lorenz, T. Mertzanidou, S. Reis, N. R. Williams, M. Keshtgar, and D. J. Hawkes. Symmetric Biomechanically Guided Prone-to-Supine Breast Image Registration. *Annals of Biomedical Engineering*, 44(1):154–173, Jan. 2016.
- [43] B. Eiben, V. Vavourakis, J. H. Hipwell, S. Kabus, C. Lorenz, T. Buelow, and D. J. Hawkes. Breast deformation modelling: comparison of methods to obtain a patient specific unloaded configuration. *Proc. SPIE*, 9036:903615–8, 2014.

- [44] B. Eiben, V. Vavourakis, J. H. Hipwell, S. Kabus, C. Lorenz, T. Buelow, N. R. Williams, M. Keshtgar, and D. J. Hawkes. Surface driven biomechanical breast image registration. In *SPIE Medical Imaging*, pages 97860W–97860W. International Society for Optics and Photonics, 2016.
- [45] M. A. Fanelli, L. M. Vargas-Roig, F. E. Gago, O. Tello, R. L. De Angelis, and D. R. Ciocca. Estrogen receptors, progesterone receptors, and cell proliferation in human breast cancer. *Breast cancer research and treatment*, 37(3):217–228, 1996.
- [46] A. G. Feldman. Once more on the equilibrium-point hypothesis ( $\lambda$  model) for motor control. *Journal of motor behavior*, 18(1):17–54, 1986.
- [47] P. Fleming, S. O’Neill, M. Owens, T. Mooney, and P. Fitzpatrick. Intermittent attendance at breast cancer screening. *Journal of public health research*, 2(2), 2013.
- [48] FNAH. Cancer du sein : modalités spécifiques de dépistage pour les femmes à haut risque. [https://www.has-sante.fr/portail/jcms/c\\_1740821/fr/cancer-du-sein-modalites-specifiques-de-depistage-pour-les-femmes-a-haut-risque](https://www.has-sante.fr/portail/jcms/c_1740821/fr/cancer-du-sein-modalites-specifiques-de-depistage-pour-les-femmes-a-haut-risque). 2016.
- [49] FRM. Les chiffres du cancer du sein. <https://www.frm.org/cancer-du-sein/>, 2017.
- [50] Y.-c. Fung. *Biomechanics: mechanical properties of living tissues*. Springer Science & Business Media, 2013.
- [51] Y.-c. Fung, P. Tong, and X. Chen. *Classical and computational solid mechanics*, volume 2. World Scientific Publishing Company, 2017.
- [52] T. P. B. Gamage, R. Boyes, V. Rajagopal, P. M. F. Nielsen, and M. P. Nash. Modelling prone to supine breast deformation under gravity loading using heterogeneous finite element models. In Poul M.F. Nielsen, Adam Wittek, and Karol Miller, editors, *Computational Biomechanics for Medicine*, pages 29–38. Springer New York, 2012.
- [53] E. Garcia, A. Oliver, O. Diaz, Y. Diez, A. Gubern-Merida, R. Marti, and J. Marti. Mapping 3d breast lesions from full-field digital mammograms using subject-specific finite element models. In *SPIE Medical Imaging*, pages 1013504–1013504. International Society for Optics and Photonics, 2017.
- [54] S. Gaur, V. Dialani, P. J. Slanetz, and R. L. Eisenberg. Architectural distortion of the breast. *American Journal of Roentgenology*, 201(5):W662–W670, 2013.
- [55] N. Geeraert, R. Klausza, S. Mullera, et al. Breast characteristics and dosimetric data in x-ray mammography a large sample worldwide survey. In *Bonn: IAEA conference*. Citeseer, 2012.

## BIBLIOGRAPHY

---

- [56] A. Gefen. The in vivo elastic properties of the plantar fascia during the contact phase of walking. *Foot & ankle international*, 24(3):238–244, 2003.
- [57] A. Gefen and B. Dilmoney. Mechanics of the normal woman’s breast. *Technology and Health Care*, 15(4):259–271, 2007.
- [58] A. Gent. A new constitutive relation for rubber. *Rubber chemistry and technology*, 69(1):59–61, 1996.
- [59] A. Gent and A. Thomas. Forms for the stored (strain) energy function for vulcanized rubber. *Journal of Polymer Science Part A: Polymer Chemistry*, 28(118):625–628, 1958.
- [60] J. Georgii, T. Paetz, M. Harz, C. Stoecker, M. Rothgang, J. Colletta, K. Schilling, M. Schlooß-Vries, R. M. Mann, and H. K. Hahn. Simulation and visualization to support breast surgery planning. In *International Workshop on Digital Mammography*, pages 257–264. Springer, 2016.
- [61] S. Govindjee and P. A. Mihalic. Computational methods for inverse deformations in quasi-incompressible finite elasticity. *International Journal for Numerical Methods in Engineering*, 43(5):821–838, 1998.
- [62] R. H. Griesenauer, J. A. Weis, L. R. Arlinghaus, I. M. Meszoely, and M. I. Miga. Breast tissue stiffness estimation for surgical guidance using gravity-induced excitation. *Physics in Medicine and Biology*, 62(12):4756, 2017.
- [63] J. E. d. Groot, W. Branderhorst, C. A. Grimbergen, G. J. d. Heeten, and M. J. Broeders. Towards personalized compression in mammography: A comparison study between pressure- and force-standardization. *European Journal of Radiology*, 84(3):384–391, 2015.
- [64] B. Hafslund. Mammography and the experience of pain and anxiety. *Radiography*, 6(4):269–272, 2000.
- [65] R. G. Hammerstein, D. W. Miller, D. R. White, M. Ellen Masterson, H. Q. Woodard, and J. S. Laughlin. Absorbed radiation dose in mammography. *radiology*, 130(2):485–491, 1979.
- [66] L. Han, J. H. Hipwell, B. Eiben, D. Barratt, M. Modat, S. Ourselin, and D. J. Hawkes. A nonlinear biomechanical model based registration method for aligning prone and supine mr breast images. *IEEE transactions on medical imaging*, 33(3):682–694, 2014.
- [67] L. Han, J. H. year, C. Tanner, Z. Taylor, T. Mertzanidou, Jorge Cardoso, Sébastien Ourselin, and David J Hawkes. Development of patient-specific biomechanical models for predicting large breast deformation. *Physics in Medicine and Biology*, 57(2):455–472, 2012.

- [68] M. Helvie, H.-P. Chan, D. Adler, and P. Boyd. Breast thickness in routine mammograms: effect on image quality and radiation dose. *AJR. American journal of roentgenology*, 163(6):1371–1374, 1994.
- [69] F. Hendriks, D. Brokken, C. Oomens, D. Bader, and F. Baaijens. The relative contributions of different skin layers to the mechanical behavior of human skin in vivo using suction experiments. *Medical engineering & physics*, 28(3):259–266, 2006.
- [70] P. Henrot, A. Leroux, C. Barlier, and P. Génin. Breast microcalcifications: the lesions in anatomical pathology. *Diagnostic and interventional imaging*, 95(2):141–152, 2014.
- [71] T. K. Ho. Random decision forests. In *Document analysis and recognition, 1995., proceedings of the third international conference on*, volume 1, pages 278–282. IEEE, 1995.
- [72] S. Hofvind, B. Geller, J. Skelly, and P. Vacek. Sensitivity and specificity of mammographic screening as practised in vermont and norway. *The British journal of radiology*, 85(1020):e1226–e1232, 2012.
- [73] T. Hopp, M. Dietzel, P. A. Baltzer, P. Kreisel, W. A. Kaiser, H. Gemmeke, and N. V. Ruiter. Automatic multimodal 2d/3d breast image registration using biomechanical fem models and intensity-based optimization. *Medical image analysis*, 17(2):209–218, 2013.
- [74] S.-Y. Huang, J. M. Boone, K. Yang, N. J. Packard, S. E. McKenney, N. D. Prionas, K. K. Lindfors, and M. J. Yaffe. The characterization of breast anatomical metrics using dedicated breast ct. *Medical physics*, 38(4):2180–2191, 2011.
- [75] D. P. Huttenlocher, G. A. Klanderman, and W. J. Rucklidge. Comparing images using the hausdorff distance. *IEEE Transactions on pattern analysis and machine intelligence*, 15(9):850–863, 1993.
- [76] A. Itoh, E. Ueno, E. Tohno, H. Kamma, H. Takahashi, T. Shiina, M. Yamakawa, and T. Matsumura. Breast disease: clinical application of us elastography for diagnosis. *Radiology*, 239(2):341–350, 2006.
- [77] M. Kaliske and H. Rothert. On the finite element implementation of rubber-like materials at finite strains. *Engineering Computations*, 14(2):216–232, 1997.
- [78] J. Kanitakis. Anatomy, histology and immunohistochemistry of normal human skin. *European journal of dermatology: EJD*, 12(4):390–9, 2002.
- [79] M. Keemers-Gels, R. Groenendijk, J. Van Den Heuvel, C. Boetes, P. Peer, and T. Wobbes. Pain experienced by women attending breast cancer screening. *Breast cancer research and treatment*, 60(3):235–240, 2000.

## BIBLIOGRAPHY

---

- [80] A. L. Kellner, T. R. Nelson, L. I. Cervino, and J. M. Boone. Simulation of mechanical compression of breast tissue. *IEEE Transactions on Biomedical Engineering*, 54(10):1885–1891, 2007.
- [81] K. Kemp Jacobsen, E. S. O’meara, D. Key, D. SM Buist, K. Kerlikowske, I. Vejborg, B. L. Sprague, and E. Lynge. Comparing sensitivity and specificity of screening mammography in the united states and denmark. *International journal of cancer*, 137(9):2198–2207, 2015.
- [82] S. J. Kim, W. K. Moon, N. Cho, J. H. Cha, S. M. Kim, and J.-G. Im. Computer-aided detection in digital mammography: comparison of craniocaudal, mediolateral oblique, and mediolateral views. *Radiology*, 241(3):695–701, 2006.
- [83] M.-S. Ko, H. H. Kim, J. H. Cha, H. J. Shin, J. H. Kim, and M. J. Kim. Dose reduction in automatic optimization parameter of full field digital mammography: Breast phantom study. *Journal of breast cancer*, 16(1):90–96, 2013.
- [84] D. B. Kopans. *Breast imaging*. Lippincott Williams & Wilkins, 2007.
- [85] T. A. Krouskop, T. M. Wheeler, F. Kallel, B. S. Garra, and T. Hall. Elastic moduli of breast and prostate tissues under compression. *Ultrasonic Imaging*, 20(4):260–274, 1998.
- [86] M. Kuhlmann, E. Fear, A. Ramirez-Serrano, and S. Federico. Mechanical model of the breast for the prediction of deformation during imaging. *Medical engineering \& physics*, 35(4):470–478, 2013.
- [87] H.-T. Leong, G. Y.-f. Ng, V. Y.-f. Leung, and S. N. Fu. Quantitative estimation of muscle shear elastic modulus of the upper trapezius with supersonic shear imaging during arm positioning. *PloS one*, 8(6):e67199, 2013.
- [88] K. M. M. Lima, E., J. F. S. C. Júnior, W. C. de Albuquerque Pereira, and L. F. de Oliveira. Assessment of the mechanical properties of the muscle-tendon unit by supersonic shear wave imaging elastography: a review. *Ultrasonography*, 37(1):3, 2018.
- [89] J. Lorenzen, R. Sinkus, M. Biesterfeldt, and G. Adam. Menstrual-cycle dependence of breast parenchyma elasticity: estimation with magnetic resonance elastography of breast tissue during the menstrual cycle. *Investigative radiology*, 38(4):236–240, 2003.
- [90] L. J. Martin. What causes breast cancer? <https://www.webmd.com/breast-cancer/guide/what-causes-breast-cancer>, 2017.

- [91] F. Martínez-Martínez, M. Rupérez-Moreno, M. Martínez-Sober, J. Solves-Llorens, D. Lorente, A. Serrano-López, S. Martínez-Sanchis, C. Monserrat, and J. Martín-Guerrero. A finite element-based machine learning approach for modeling the mechanical behavior of the breast tissues under compression in real-time. *Computers in Biology and Medicine*, 90:116–124, 2017.
- [92] R. J. McKenna. The abnormal mammogram radiographic findings, diagnostic options, pathology, and stage of cancer diagnosis. *Cancer*, 74(S1):244–255, 1994.
- [93] R. M. McMeeking and J. Rice. Finite-element formulations for problems of large elastic-plastic deformation. *International Journal of Solids and Structures*, 11(5):601–616, 1975.
- [94] C. Mercer, P. Hogg, R. Lawson, J. Diffey, and E. Denton. Practitioner compression force variability in mammography: a preliminary study. *The British journal of radiology*, 86(1022):20110596, 2013.
- [95] D. Miller, V. Livingstone, and P. Herbison. Interventions for relieving the pain and discomfort of screening mammography. *Cochrane Database Syst Rev*, 1, 2008.
- [96] T. T. Mugea and M. A. Shiffman. *Aesthetic Surgery of the Breast*. Springer, 2014.
- [97] NCI. Breast and adjacent lymph nodes, national cancer institute. <https://www.cancer.gov/publications/patient-education/wyntk-breast-cancer>, 2012.
- [98] NHSBSP. 2012 review of the uk breast screening programme. <http://www.cancerresearchuk.org/about-cancer/breast-cancer/screening/screening-2012-review>, 2012.
- [99] A. Nordez and F. Hug. Muscle shear elastic modulus measured using supersonic shear imaging is highly related to muscle activity level. *Journal of applied physiology*, 108(5):1389–1394, 2010.
- [100] S. Obenauer, S. Luftner-Nagel, D. Von Heyden, U. Munzel, F. Baum, and E. Grabbe. Screen film vs full-field digital mammography: image quality, detectability and characterization of lesions. *European radiology*, 12(7):1697–1702, 2002.
- [101] R. W. Ogden. Large deformation isotropic elasticity—on the correlation of theory and experiment for incompressible rubberlike solids. In *Proc. R. Soc. Lond. A*, volume 326, pages 565–584. The Royal Society, 1972.
- [102] D. O’Leary, A. Teape, J. Hammond, L. Rainford, and T. Grant. Compression force recommendations in mammography must be linked to image quality. In *Proceedings of the European Congress of Radiology*, pages 1–19, 2011.

## BIBLIOGRAPHY

---

- [103] D. Ç. Olgun, B. Korkmazer, F. Kılıç, A. S. Dikici, M. Velidedeoğlu, F. Aydoğan, F. Kantarcı, and M. H. Yılmaz. Use of shear wave elastography to differentiate benign and malignant breast lesions. *Diagnostic and Interventional Radiology*, 20(3):239, 2014.
  - [104] B. H. Østerås, P. Skaane, R. Gullien, and A. C. T. Martinsen. Average glandular dose in paired digital mammography and digital breast tomosynthesis acquisitions in a population based screening program: effects of measuring breast density, air kerma and beam quality. *Physics in medicine and biology*, 2018.
  - [105] A. P. d. Palomar, B. Calvo, J. Herrero, J. López, and M. Doblaré. A finite element model to accurately predict real deformations of the breast. *Medical Engineering & Physics*, 30(9):1089–1097, 2008.
  - [106] S. Pandya and R. G. Moore. Breast development and anatomy. *Clinical obstetrics and gynecology*, 54(1):91–95, 2011.
  - [107] P. Patete, M. I. Iacono, M. F. Spadea, G. Trecate, D. Vergnaghi, L. T. Mainardi, and G. Baroni. A multi-tissue mass-spring model for computer assisted breast surgery. *Medical Engineering and Physics*, 35(1):47–53, 2013.
  - [108] P. Pathmanathan, D. J. Gavaghan, J. P. Whiteley, S. J. Chapman, and J. M. Brady. Predicting tumor location by modeling the deformation of the breast. *IEEE Transactions on Biomedical Engineering*, 55(10):2471–2480, 2008.
  - [109] E. A. Pechter. A new method for determining bra size and predicting postaugmentation breast size. *Plastic and reconstructive surgery*, 102(4):1259–1265, 1998.
  - [110] L. A. Peipins, J. A. Shapiro, J. K. Bobo, and Z. Berkowitz. Impact of women’s experiences during mammography on adherence to rescreening (united states). *Cancer causes & control*, 17(4):439–447, 2006.
  - [111] N. Perry, M. Broeders, C. de Wolf, S. Törnberg, R. Holland, and L. von Karsa. European guidelines for quality assurance in breast cancer screening and diagnosis.—summary document. *Annals of Oncology*, 19(4):614–622, 2008.
  - [112] N. H. Peters, I. H. Borel Rinkes, N. P. Zuithoff, W. P. Mali, K. G. Moons, and P. H. Peeters. Meta-analysis of mr imaging in the diagnosis of breast lesions. *Radiology*, 246(1):116–124, 2008.
  - [113] R. Peto, J. Boreham, M. Clarke, C. Davies, and V. Beral. Uk and usa breast cancer deaths down 25% in year 2000 at ages 20–69 years. *The Lancet*, 355(9217):1822, 2000.
  - [114] M. C. Pike, D. V. Spicer, L. Dahmoush, and M. F. Press. Estrogens progestogens normal breast cell proliferation and breast cancer risk. *Epidemiologic reviews*, 15(1):17–35, 1993.
-

- [115] L. S. Pilcher. The breast, its anomalies, its diseases and their treatment. *Annals of Surgery*, 65(4):527, 1917.
- [116] A. Poulos, D. McLean, M. Rickard, and R. Heard. Breast compression in mammography: how much is enough? *Journal of Medical Imaging and Radiation Oncology*, 47(2):121–126, 2003.
- [117] V. Rajagopal, J.-H. Chung, R. P. Highnam, R. Warren, P. M. Nielsen, and Martyn P. Nash. Mapping microcalcifications between 2d mammograms and 3d MRI using a biomechanical model of the breast. In Karol Miller and Poul M.F. Nielsen, editors, *Computational Biomechanics for Medicine*, pages 17–28. Springer, 2010.
- [118] V. Rajagopal et al. *Modelling breast tissue mechanics under gravity loading*. PhD thesis, ResearchSpace@ Auckland, 2007.
- [119] V. Rajagopal, A. Lee, J.-H. Chung, R. Warren, R. P. Highnam, M. P. Nash, and P. M. Nielsen. Creating individual-specific biomechanical models of the breast for medical image analysis. *Academic Radiology*, 15(11):1425–1436, 2008.
- [120] V. Rajagopal, P. M. F. Nielsen, and M. P. Nash. Modeling breast biomechanics for multi-modal image analysis—successes and challenges. *Wiley Interdisciplinary Reviews: Systems Biology and Medicine*, 2(3):293–304, 2010.
- [121] E. Riggio, P. Quattrone, and M. Nava. Anatomical study of the breast superficial fascial system: the inframammary fold unit. *European Journal of Plastic Surgery*, 23(6):310–315, 2000.
- [122] R. S. Rivlin and D. Saunders. Large elastic deformations of isotropic materials vii. experiments on the deformation of rubber. *Phil. Trans. R. Soc. Lond. A*, 243(865):251–288, 1951.
- [123] P.-Y. Rohan, C. Lobos, M. A. Nazari, P. Perrier, and Y. Payan. Finite element modelling of nearly incompressible materials and volumetric locking: a case study. *Computer methods in biomechanics and biomedical engineering*, 17(sup1):192–193, 2014.
- [124] N. V. Ruiter, R. Stotzka, T.-O. MULLER, H. Gemmeke, J. R. Reichenbach, and W. Kaiser. Model-based registration of x-ray mammograms and MR images of the female breast. *IEEE Transactions on Nuclear Science*, 53(1):204–211, 2006.
- [125] A. Samani, J. Bishop, M. J. Yaffe, and D. B. Plewes. Biomechanical 3-d finite element modeling of the human breast using MRI data. *Medical Imaging, IEEE Transactions on*, 20(4):271–279, 2001.
- [126] A. Samani and D. Plewes. A method to measure the hyperelastic parameters of ex vivo breast tissue samples. *Physics in Medicine and Biology*, 49(18):4395–4405, 2004.

## BIBLIOGRAPHY

---

- [127] A. Samani, J. Zubovits, and D. Plewes. Elastic moduli of normal and pathological human breast tissues: an inversion-technique-based investigation of 169 samples. *Physics in medicine and biology*, 52(6):1565, 2007.
- [128] R. S. Saunders and E. Samei. The effect of breast compression on mass conspicuity in digital mammography. *Medical physics*, 35(10):4464–4473, 2008.
- [129] S. Shrestha and A. Poulos. The effect of verbal information on the experience of discomfort in mammography. *Radiography*, 7(4):271–277, 2001.
- [130] R. Sinkus, M. Tanter, T. Xydeas, S. Catheline, J. Bercoff, and M. Fink. Viscoelastic shear properties of in vivo breast lesions measured by mr elastography. *Magnetic resonance imaging*, 23(2):159–165, 2005.
- [131] J. E. Skandalakis. Embryology and anatomy of the breast. *Breast augmentation: principles and practice*. Springer, Berlin, 12, 2009.
- [132] SPF. Sante publique france: Cancer du sein. <http://invs.santepubliquefrance.fr/Dossiers-thematiques/Maladies-chroniques-et-traumatismes/Cancers/Donnees-par-localisation/Cancer-du-sein>, 2016.
- [133] G. M. Sturgeon, N. Kiarashi, J. Y. Lo, E. Samei, and W. P. Segars. Finite-element modeling of compression and gravity on a population of breast phantoms for multimodality imaging simulation. *Medical Physics*, 43(5):2207–2217, 2016.
- [134] A. Sutradhar and M. J. Miller. In vivo measurement of breast skin elasticity and breast skin thickness. *Skin Research and Technology*, 19(1), 2013.
- [135] L. Tabár, B. Vitak, H.-H. T. Chen, M.-F. Yen, S. W. Duffy, and R. A. Smith. Beyond randomized controlled trials. *Cancer*, 91(9):1724–1731, 2001.
- [136] C. Tanner, J. A. Schnabel, D. L. G. Hill, D. J. Hawkes, M. O. Leach, and D. R. Hose. Factors influencing the accuracy of biomechanical breast models. *Medical Physics*, 33(6):1758, 2006.
- [137] L. Treloar. The elasticity of a network of long-chain molecules—ii. *Transactions of the Faraday Society*, 39:241–246, 1943.
- [138] H. Ulger, N. Erdogan, S. Kumanlioglu, and E. Unur. Effect of age, breast size, menopausal and hormonal status on mammographic skin thickness. *Skin Research and Technology*, 9(3):284–289, 2003.
- [139] E. E. Van Houten, M. M. Doyley, F. E. Kennedy, J. B. Weaver, and K. D. Paulsen. Initial in vivo experience with steady-state subzone-based mr elastography of the human breast. *Journal of magnetic resonance imaging*, 17(1):72–85, 2003.

- [140] J. Vandeput and M. Nelissen. Considerations on anthropometric measurements of the female breast. *Aesthetic plastic surgery*, 26(5):348–355, 2002.
- [141] V. Vavourakis, J. H. Hipwell, and D. J. Hawkes. An inverse finite element u/p-formulation to predict the unloaded state of in vivo biological soft tissues. *Annals of biomedical engineering*, 44(1):187–201, 2016.
- [142] P. Wellman, R. D. Howe, E. Dalton, and K. A. Kern. Breast tissue stiffness in compression is correlated to histological diagnosis. *Harvard BioRobotics Laboratory Technical Report*, pages 1–15, 1999.
- [143] M. P. Wenger, L. Bozec, M. A. Horton, and P. Mesquida. Mechanical properties of collagen fibrils. *Biophysical journal*, 93(4):1255–1263, 2007.
- [144] P. Whelehan, A. Evans, M. Wells, and S. MacGillivray. The effect of mammography pain on repeat participation in breast cancer screening: a systematic review. *The Breast*, 22(4):389–394, 2013.
- [145] M. B. Williams, P. Raghunathan, M. J. More, J. A. Seibert, A. Kwan, J. Y. Lo, E. Samei, N. T. Ranger, L. L. Fajardo, A. McGruder, et al. Optimization of exposure parameters in full field digital mammography. *Medical physics*, 35(6Part1):2414–2423, 2008.
- [146] A. Williamson and B. Hoggart. Pain: a review of three commonly used pain rating scales. *Journal of clinical nursing*, 14(7):798–804, 2005.
- [147] M. Yaffe, J. Boone, N. Packard, O. Alonzo-Proulx, S.-Y. Huang, C. Peressotti, A. Al-Mayah, and K. Brock. The myth of the 50-50 breast. *Medical physics*, 36(12):5437–5443, 2009.
- [148] O. Yeoh. Characterization of elastic properties of carbon-black-filled rubber vulcanizates. *Rubber chemistry and technology*, 63(5):792–805, 1990.
- [149] J. H. Youk, H. M. Gweon, and E. J. Son. Shear-wave elastography in breast ultrasound: the state of the art. *Ultrasonography*, 36(4):300, 2017.
- [150] P. A. Yushkevich, J. Piven, H. Cody Hazlett, R. Gimpel Smith, S. Ho, J. C. Gee, and G. Gerig. User-guided 3D active contour segmentation of anatomical structures: Significantly improved efficiency and reliability. *Neuroimage*, 31(3):1116–1128, 2006.
- [151] F. E. Zajac. Muscle and tendon properties models scaling and application to biomechanics and motor. *Critical reviews in biomedical engineering*, 17(4):359–411, 1989.